Defects in crystals studied by Raman scattering

Masahiro Kitajima

Defects in Crystals Studied by Raman Scattering

Masahiro Kitajima

National Research Institute for Metals, 1–2–1 Sengen, Tsukuba, Ibaraki, 305 Japan;
e-mail kitajima@nrim.go.jp

ABSTRACT: Raman studies of crystal defects are reviewed. Raman spectroscopy is a powerful technique and has been used widely for investigating disordered structures. The degree of disorder in a crystal is quantitatively evaluated in terms of the phonon correlation length. The asymmetric Raman line shapes in defective crystals such as microcrystals, ion-implanted semiconductors are well reproduced by the spatial correlation (SC) model. The effect of alloying induced-potential fluctuations on Raman scattering is also explained within the framework of the SC model. In disordered graphite, the in-plane phonon correlation length is obtained from the relative intensity ratio of the disorder induced peak. The initial lattice disordering rates and the relaxation rates of disorder are determined, using real-time Raman measurements during ion irradiation in a scale of seconds. In this way, the phonon confinement due to the local defects is observed in the kinetic manner. Localized vibrational modes of defects in crystals are also described. In particular, Raman observation of the hydrogen molecule in crystalline semiconductors is discussed in detail.

KEY WORDS: Raman scattering, defects in crystals, disordering kinetics, optical phonon modes, localized vibrational modes.

TABLE OF CONTENTS

I. INTRODUCTION

Raman scattering has been used widely for investigating disordered structures such as micro- or nano-crystals, alloys or compounds, mixed oxides, impurities-doped semiconductors, and ion-implanted crystals. For studying defects in crystals by Raman scattering, there are generally two angles to analyze the Raman spectra: one from optical phonon modes and the other from local modes. (1) We can learn about the degree of disorder in crystals from spectral shape changes of optical phonons. One of the most important selection rules for light scattering processes in crystals is the conversion of the wave-vector. In Raman scattering from perfect crystals, only phonon modes near the center of the Brillouin-zone (Γ-point) are observed, owing to the wave-vector selection rule. For disordered crystals, the periodicity diminishes and Raman scatter-

ing can be observed for phonon modes having in principle any wave vector. In other words, nonperiodicity causes the relaxation of the wave vector selection rules, and hence phonon modes having wave-vectors other than $q = 0$ are also observed.[1,2] The relaxation of the selection rule leads to changes in the line shape for the phonon mode and this is observed frequently in disordered semiconductors. In some crystals, the relaxation induces a development of a new Raman line that cannot be allowed to appear in perfect crystals. (2) The Raman scattering enables us to directly identify local vibrational modes that are related to configurations of impurities or vacancies. This method provides more detailed information on the identity and the location of the isolated defects.

Thus, Raman spectra provides important information on disordered materials such as size of microcrystal or cluster, density of defects, strains or stresses, damage profiles, identity of impurities, and their chemical states. Nondestructive kinetic studies on disordering and relaxation of the disordered structures are also possible combined with real-time techniques. There are many papers on the Raman scattering of disordered crystals of semiconductors and carbon materials, as referred in this review. In particular, Raman scattering has been applied successfully to the studies of disordering in crystals induced by ion implantation.

In this article, the most recent results on Raman spectroscopic studies of defects in crystals are reviewed. We focus mostly on semiconductors and graphite.

II. RAMAN SCATTERING AND CRYSTALS

In this article we briefly explain the basic physics of Raman scattering from crystals. Particularly, the physical meaning of the wave-vector selection rule, which is important for considering the effects of disorder in crystals on Raman scattering, is stressed. When monochromatic radiation of wave number v_i is incident on a substance like molecule or crystal, most of it is transmitted without change, but, in addition, some scattering of the radiation occurs. If the frequency content of the scattered radiation is analyzed, you can observe not only the wave number v_i associated with the incident radiation but also, in general, pairs of new wave numbers of the type $v_s = v_i \pm v_R$. In molecular systems, the wave numbers v_R are found to lie principally in the ranges associated with transitions between rotational, vibrational, and electronic levels. Such scattering of radiation with change of wave numbers (or frequency) is called Raman scattering.

The simplest picture of the mechanism of the Raman scattering is furnished by considering the interaction between a light quantum and a molecule, as a collision satisfying the law of conservation of energy. If the incident light quantum suffers a loss of energy as a result of the encounter, it appears in the spectrum as a radiation of diminished frequency (i.e., as a Stokes line), while the molecule that takes up the energy is transported to a higher level of rotation or vibration. It is also possible to conceive of collisions in which the molecule, already in an excited state, gives up its energy to the light quantum and comes down to a lower level. The scattered radiation then appears in the spectrum as a line of increased frequency (i.e., as an anti-Stokes line). In either case the spectral shifts of the modified radiations from the parent line give us a measure of the rotational or vibrational frequencies of the molecule. In a crystal the spectral shifts give vibrational frequencies of the optical phonon modes. The important parameters obtained from Raman scattering are the frequency shifts, the state of polarization, and the intensities of the Raman lines. The frequency shifts are expressed in

wave numbers (cm^{-1}) and obtained as the differences of the wave numbers of the exciting (incident) line and the corresponding Raman lines (Raman shift).

While infrared absorption involves only one transition, namely, the direct transition between the two states, the Raman scattering is the result of a double transition involving three stationary levels. The Raman line corresponding to the transition from the initial level (i) to the final level (f) of the system can appear only when there is an intermediate level (also called the virtual level) that can combine with i and f in absorption or emission. If there is no such intermediate state at all, the corresponding transition $i \rightarrow f$ is forbidden in the Raman scattering. The vibrations of a molecule that produce changes in the polarizability of the molecule make the molecule (or lattice) active in the Raman scattering, and the selection rules govern the appearance of a Raman line. The symmetric vibrations of the molecule (or lattice) that are usually missed in the infrared, comes out most prominently in Raman scattering. Generally, the Raman spectra and the infrared absorption spectra are not identical but complementary in character.

Raman scattering arises from the radiating dipole moment induced in a system by the electric field of incident electromagnetic radiation. In a crystal the electric field of a plane, monochromatic wave of frequency v_i propagating in a direction k_i is represented by the expression

$$\mathbf{E}_i = \mathbf{E}^0 e^{-i(\mathbf{k}_i \cdot \mathbf{r} - 2\pi v_i t)} \qquad (1)$$

The frequency of this exciting radiation is usually chosen to be in the visible region of the spectrum. Thus, v_i is very large compared with the frequencies of any of the crystal vibrations.

· The dipole moment induced in the system of the exciting radiation is given by

$$\mathbf{m} = \alpha \mathbf{E}_i \qquad (2)$$

where α is the polarizability tensor. Eq. 2 describes polarization of the crystals, which is, in general, a function of the instantaneous positions of the atoms in the lattice. Hence, the polarizability can be expanded in a set of normal coordinates of the crystals,[9-11] viz.,

$$\alpha = \alpha_0 + \sum_k \left(\frac{\partial \alpha}{\partial Q_k} \right)_0 Q_k$$
$$+ \frac{1}{2} \sum_{k,l} \left(\frac{\partial^2 \alpha}{\partial Q_k \partial Q_l} \right)_0 Q_k Q_l + \cdots \qquad (3)$$

The linear term in Q_k is responsible for first-order scattering, while the quadratic and higher terms account for the second- and higher-order effects.

In crystals, propagation of the lattice wave must be considered. Since the lattice wave of vibrational frequency v_k propagating in a direction given by the wave vector q_k is represented by

$$Q_k = A_k e^{\pm i(\mathbf{q}_k \cdot \mathbf{r} - 2\pi v_k t)} \qquad (4)$$

for each normal coordinate, Q_k, the induced dipole becomes, to first order,[9]

$$\mathbf{m} = \alpha_0 \mathbf{E}^0 e^{-i(\mathbf{k}_i \cdot \mathbf{r} - 2\pi v_i t)}$$
$$+ \sum_k \left(\frac{\partial \alpha}{\partial Q_k} \right)_0 A_k \mathbf{E}^0 e^{\pm i[(\mathbf{k}_i \pm \mathbf{q}_k) \cdot \mathbf{r} - 2\pi(v_i \mp v_k)t]}$$

$$(5)$$

The first term corresponds to the Rayleigh scattering. The scattered light with a frequency $v_i \mp v_k$ propagating in a direction $k_i \pm q_k$ is then referred to as the Raman scatter-

ing. (When acoustic frequencies are involved, the term Brillouin scattering is employed.) The frequencies given by $v_i \mp v_k$ are the *Stokes* or the *anti-Stokes* Raman frequencies, depending on the choice of sign. For vibrations of molecules (or local vibrational modes in crystals), the phase term of $k_i \pm q_k$ is not included in the Raman scattering processes because the positions of molecules can be taken as $r = 0$.

In crystals, as in isolated molecules, the vibrational energy levels take the form

$$E_{nk} = hv_k\left(n_k + \frac{1}{2}\right), \quad n_k = 0,1,2,...\quad (6)$$

in the harmonic approximation. However, in crystals the frequency v_k is a function of the wave vector q, as determined by the dispersion relation (see, for example, Figures 1 and 2). The quantum of energy of lattice vibration wave hv_k is often referred to as a *phonon*, by analogy with the term *photon* for a quantum electromagnetic (light) energy. Phonons have directional properties, as they depend directly on the wave vector, q. The effective momentum of a phonon can be represented by hq. Thus, the interaction of a phonon with a photon of electromagnetic radiation, for example, is governed by the law of conservation of momentum, as well as the usual principle of energy conservation.

The conservation laws lead to the selection rules for Raman scattering from crystals:

$$v = \pm(v_i - v_s) \quad \text{and} \quad q = \mp(k_i - k_s) \quad (7)$$

where v is the phonon frequency, and v_s and k_s are the frequency and the wave vector of the scattered light, respectively. As the wavelength of the scattered light differs little from that of the incident radiation (λ), then effectively $k_s \approx k_i$ ($=2\pi/\lambda$) and the mag-

nitude of the wave vector of the scattering lattice wave is given by

$$q = 2k_i \sin\frac{\theta}{2} \quad (8)$$

where θ is the scattering angle with respect to the incident light beam. The value of q is no more than $4\pi/\lambda$. Usually, we use a visible laser light of about 500 nm wavelength, and, then, q is much smaller than the value of the Brillouin-zone boundary wave vector, π/a, because the lattice constant a could be an order of 1 nm. Hence, first-order Raman scattering only allows one to study the excitations near the center of the Brillouin zone in the phonon dispersion relation: the $q = 0$ selection rule.[3] This wave vector selection rule in Raman scattering would be collapsed when introducing defects to crystals, leading to the optical Raman spectral changes, as discussed in detail in this review.

For more detailed discussions of Raman scattering processes in solids, there are many good reviews.[1,4-11]

III. PHONON CONFINEMENT AND RAMAN SCATTERING IN DISORDERED CRYSTALS

The Raman line shapes would change when introducing disorders to the crystals and are theoretically explained by several authors.[1,12,13,28] Here we explain the spatial correlation (SC) model, which many researchers are applying to the analyses for disordered crystals. The degree of disorder is quantitatively estimated in terms of the phonon correlation length, L, which corresponds to a length of phonon confinement by defects or a microcrystallite size. L can be obtained by applying the SC model to the analysis of the Raman phonon line shape, that is, frequency shift and line width. In
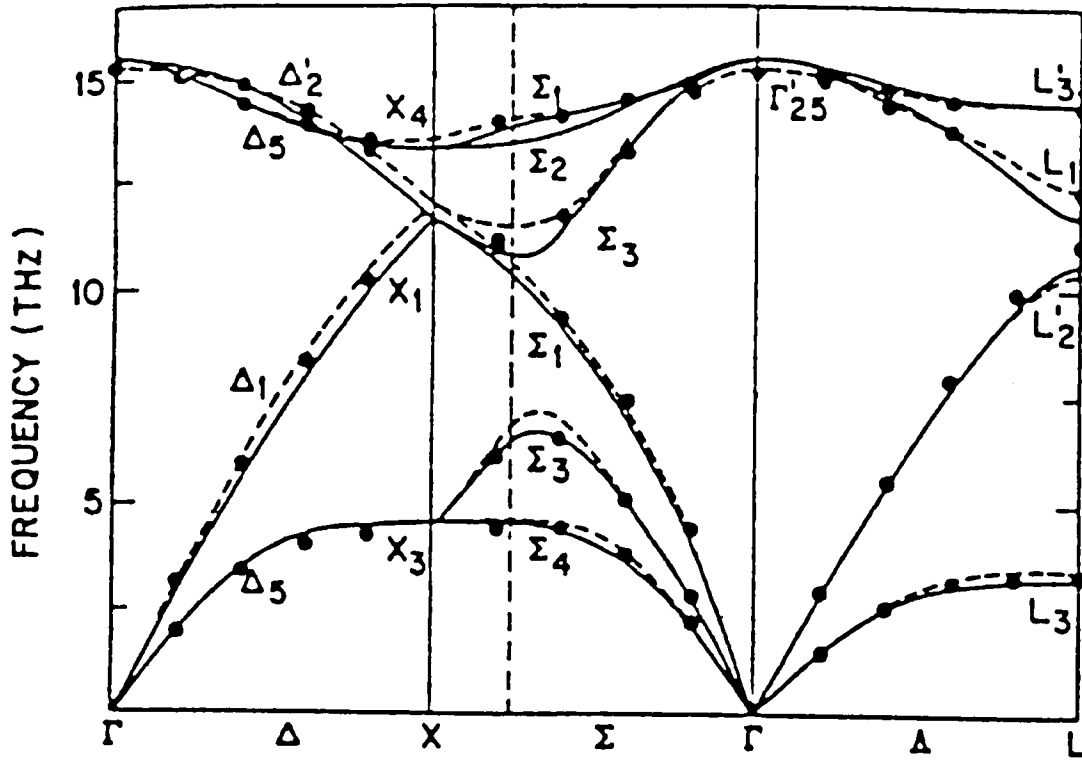
FIGURE 1. Phonon dispersion curves for Si. Solid lines show the adiabatic bond charge model results. Solid lines are experimemtal values. Dashed lines represent the VFF calculations. (see Ref. 49.)

materials where disorder-induced Raman scattering (DIRS) peaks develop due to the relaxation of the $q = 0$ selection rule, we can obtain L in a much easier way from the relative intensity ratio of the DIRS peak with respect to the crystal peak.

A. Spatial Correlation Model

The spatial correlation (SC) model was originated by Richter et al.[12] to explain the line shape of the first-order Raman scattering of microcrystalline silicon. As mentioned in the introduction, the region over which the spatial correlation function of the phonon extends is infinite in a perfect crystal. This leads to the usual plane wave phonon eigenstates and the $q = 0$ selection momen-

tum rule of the first-order Raman scattering. However, when the crystal is damaged by ion-irradiation or the material consists of microcrystallites, the mode correlation functions become finite due to the defects. Thus, there is a relaxation of the $q = 0$ selection rule and associated with this relaxation, a finite phonon correlation length (L). This allows a greater range of phonon modes to contribute to Raman scattering: a range $\Delta q \sim 1/L$ of allowed phonon q values. Experimentally, this is often observed as an asymmetrical broadening of the Raman line shape.[13-15,17]

In an infinite crystal, the wave function of a phonon with wave vector q_0 has been described by[12]

$$\Phi(q_0, r) = u(q_0, r)e^{iq \cdot r} \qquad (9)$$

280
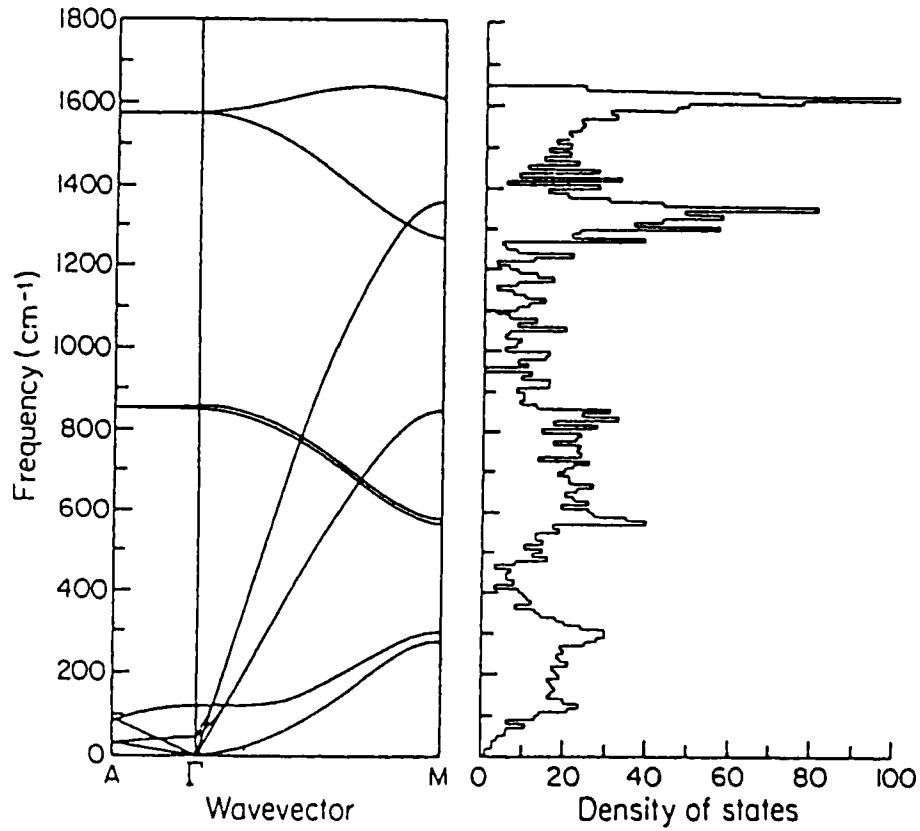
Graphite

FIGURE 2. Phonon dispersion relations of graphite[20] and the corresponding phonon density of states.[21]

where $u(q_0,r)$ has the periodicity of the lattice. When the crystal is defective, the phonon is supposed to be restricted to a spherical region of diameter L.[12] The phonon confinement changes the phonon wave function to

$$\Psi(q_0,r) = W(r,L)\Phi(q_0,r) = \Psi'(q_0,r)u(q_0,r)$$

(10)

where $W(r,L)$ is the phonon weighing function. The Gaussian function $\exp(-\alpha r^2/L^2)$ has been used as $W(r,L)$[12-16] to map the distribution of microcrystals. There is no physical reason to assume this form of confinement or its particular value at the boundary.[13]

Richter et al.[12] first made a choice of $\alpha = 2$ for a microcrystal silicon as described later. Tiong et al.[15] used a value of $\alpha = 8\pi^2$ for ion-implanted GaAs crystals. Campbell and Fauchet discussed the value of α and the effect of shape of microcrystal on Raman spectra based on the SC model.[13]

To calculate the effect on the Raman spectrum Ψ' in Eq. 10 is expanded in a Fourier series

$$\Psi'(q_0,r) = \int d^3q\, C(q_0,q)e^{iq\cdot r} \quad (11)$$

with Fourier coefficient $C(q_0,q)$ determined by

$$C(\mathbf{q}_0,\mathbf{q}) = \frac{1}{(2\pi)^3} \int d^3r \Psi'(\mathbf{q}_0,\mathbf{r})e^{-i\mathbf{q}\cdot\mathbf{r}} \quad (12)$$

The phonon wavefunction of a defective crystal is a superposition of eigenfunctions with q vectors centered at $\mathbf{q}_0$. For the Gaussian weighing function, the Fourier coefficients are

$$|C(0,\mathbf{q})|^2 \cong e^{q^2 L^2 / 2\alpha} \quad (13)$$

where we have neglected scale factors and assumed $\mathbf{q}_0 = 0$ which is appropriate for one phonon scattering.[13] The first-order Raman spectrum, $I(\omega)$, is

$$I(\omega) \propto \int \frac{d^3q |C(0,\mathbf{q})|^2}{[(\omega - \omega(\mathbf{q}))]^2 + [\Gamma_0/2]^2} \quad (14)$$

where $\omega(\mathbf{q})$ is the phonon dispersion curve ($\omega = 2\pi\nu$) and Γ_0 is the natural line width. In Figure 1 the phonon dispersion curves of silicon are shown.[49] If L is finite and the phonon dispersion curves vary significantly in the region near q = 0, spectral features could shift or broaden (or new features could occur, as mentioned later in Section III.B). In the absence of phonon confinement (infinite L) Eq. 14 becomes a Lorentzian type,[13]

$$\propto \frac{1}{[\omega - \omega(0)]^2 + [\Gamma_0/2]^2}$$

In other words, phonon Raman lines change from a symmetric Lorentzian shape to asymmetric shapes when going from single (perfect) crystal to microcrystalline structures.

B. Disorder-Induced Raman Scattering

The relaxation of the wave-vector selection rule, in addition to the asymmetric shape change of the first order Raman line, makes all non zero-center phonons (q ≠ 0) observable. Thus, in some cases, we can observe very sensitively disorder induced Raman scattering (DIRS) peaks (they are also called DARS [disorder-activated Raman scattering]). Graphite is a good example of this case. Figure 2 shows phonon dispersion relations of graphite and the corresponding phonon density of states (DOS).[20-22] While single-crystal graphite corresponding to the DOS exhibits a sharp line at $\approx$1580 cm^{-1} (G), disordered graphite exhibits an additional line at $\approx$1360 cm^{-1} (D), as described in more detail later. These two lines are the main peaks in the Raman spectrum of graphite. The G-peak is assigned to the Raman-active E_{2g}-mode lattice vibration in the graphite-plane. On the other hand, the D-peak is a typical DIRS peak of graphite corresponding to a strong maximum of DOS,[19] which is not allowed to appear because of the q = 0 selection rule in single crystal graphite.

It is well known that the relative intensity ratio (R) of the D-peak with respect to the G-peak is inversely proportional to an in-plane microcrystallite size in graphite La.[23] The relation is given by an empirical relation

$$R = C/La \quad (15)$$

where the constant C is 4.4 nm.[23,24] A Raman study of graphite with various crystallite sizes showed that La is considered to correspond to the in-plane phonon correlation length.[25,50] In graphite, La can be a measure of the microcrystallite size or the length of phonon propagation in the graphite plane. The appearance of the D-peak is well explained if we consider the attenuation of the phonon wave functions by point defects.[29,30] When phonon confinement occurs in the graphite plane (finite La), the D-peak appears (R increases) and the phonon correlation length or microcrytallite size decreases.

IV. PHONON RAMAN SPECTRA IN DISORDERED CRYSTALS

In Section III, a theoretical background of asymmetric line broadening in disordered crystals and the phonon correlation length was discussed. In this section we explain examples of the measured Raman spectra of disordered semiconductors, insulators, and carbon materials.

A. Microcrystals and Compounds

1. Asymmetric Line Broadening and Frequency Shift

Richter et al. first applied their SC model to microcrystalline (μc)-silicon.[12] The

Raman line of the μc-silicon is asymmetric with some tailing toward lower Raman shifts. This asymmetric lineshape and the shift are well reproduced by the SC model, as shown in Figure 3. Figure 4 shows the relationship between the Raman peak shift and the full linewidth. The solid line is calculated by Eq. 14 as a function of L. It is known that the width and the shift increase as L decreases. The agreement between theory and experiment is good.

Nemanich et al.[28] performed Raman scattering and X-ray diffraction measurements to correlate the finite size effects on Raman spectra of nonpolar vibrational modes in hexagonal BN. The Raman measurements showed that the E_{2g} mode shifted to higher frequency and broadened as the microcrystal size decreased. They calculated the varia-
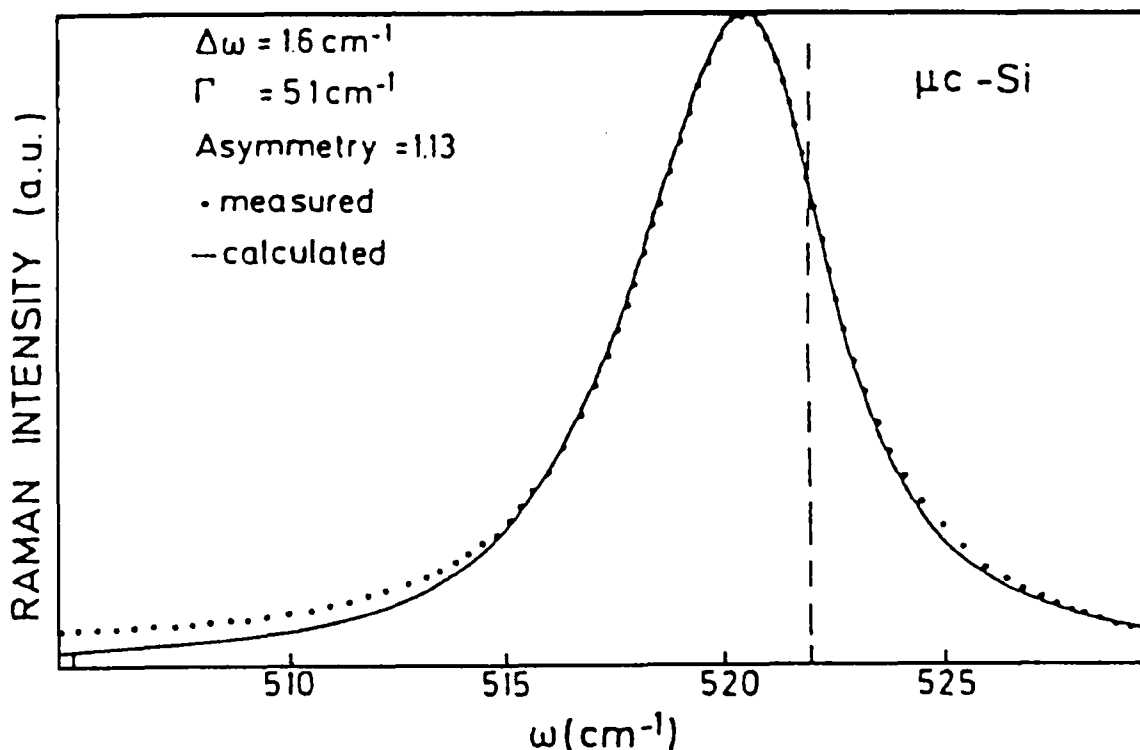

FIGURE 3. Measured and calculated Raman line of a μc-Si sample. The dashed line indicates the Raman shift for c-Si. The calculation was made by Eq. 14.[12]
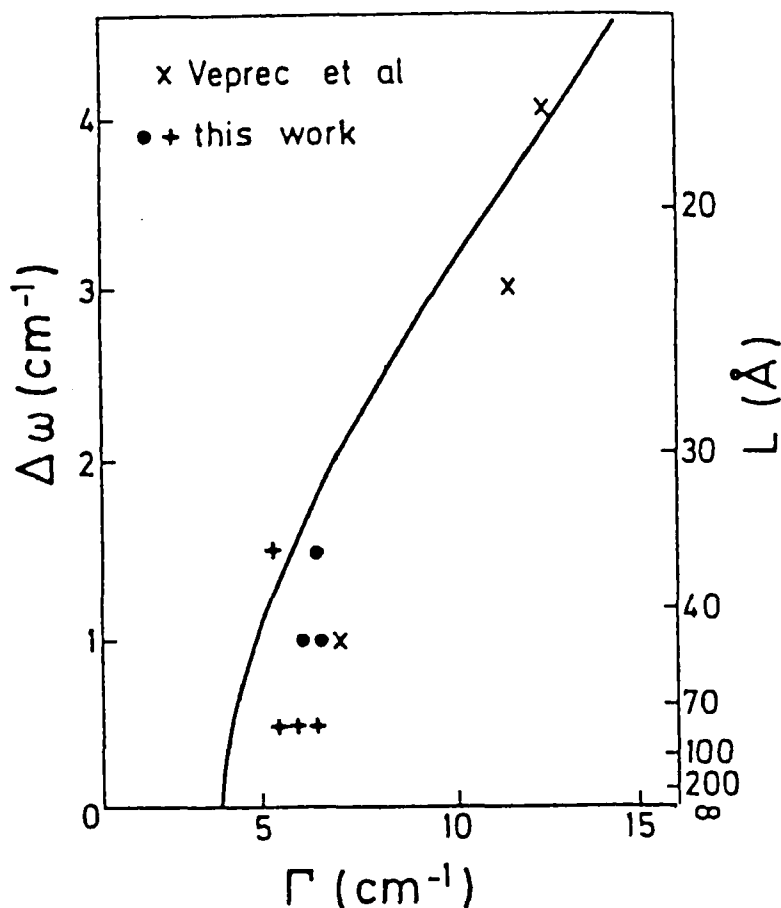
FIGURE 4. Relationship between shift $\Delta\omega$ and width Γ of the Raman line in microcrystalline silicon.[12] The points are from measurements on microcrystalline Si films prepared by the plasma transport method.[12] Crosses are values taken from Ref. 17. The solid line shows the calculated result using Eq. 14.

tion of peak shift on $1/L_a$ based on a similar idea with the relaxation of the $q = 0$ selection rule to the SC model, and their calculation was in good agreement with their observation (Figure 5).

Asymmetric Raman line broadenings were also observed in SiC crystals containing sticking faults,[2,31] SiC powders,[32] and porous SiC.[32] Another interesting example of line broadening is crystalline rutile (TiO_2).[33] Raman measurements of rutile from 4 K to 500 K showed that the A_{1g} and E_g modes in defect rutile are broader than the corresponding bands of stoichiometric rutile. For example, at 80 K the E_g band of stoichiometric rutile had a width of about

12 cm^{-1}, whereas in the non-stoichiometric rutile the width was 18 to 25 cm^{-1}. As shown in Figure 6, the bandwidth of the more highly reduced rutile $(10^{-11}$ atm) is broader than the bands of the less-reduced crystals. This was interpreted as being due to the randomizing effect of oxygen vacancies in the defect crystal.[33]

So far, we have discussed Raman spectral changes due to structural disorder in crystals. The idea of the SC model is more general. Parayanthal and Pollak[34] studied semiconductor alloys $(Ga_{1-x}Al_xAs/GaAs$ and $Ga_{0.47}In_{0.53}As/InP)$ with Raman scattering. They explained the broadening and asymmetry of the first-order longitudinal-optic
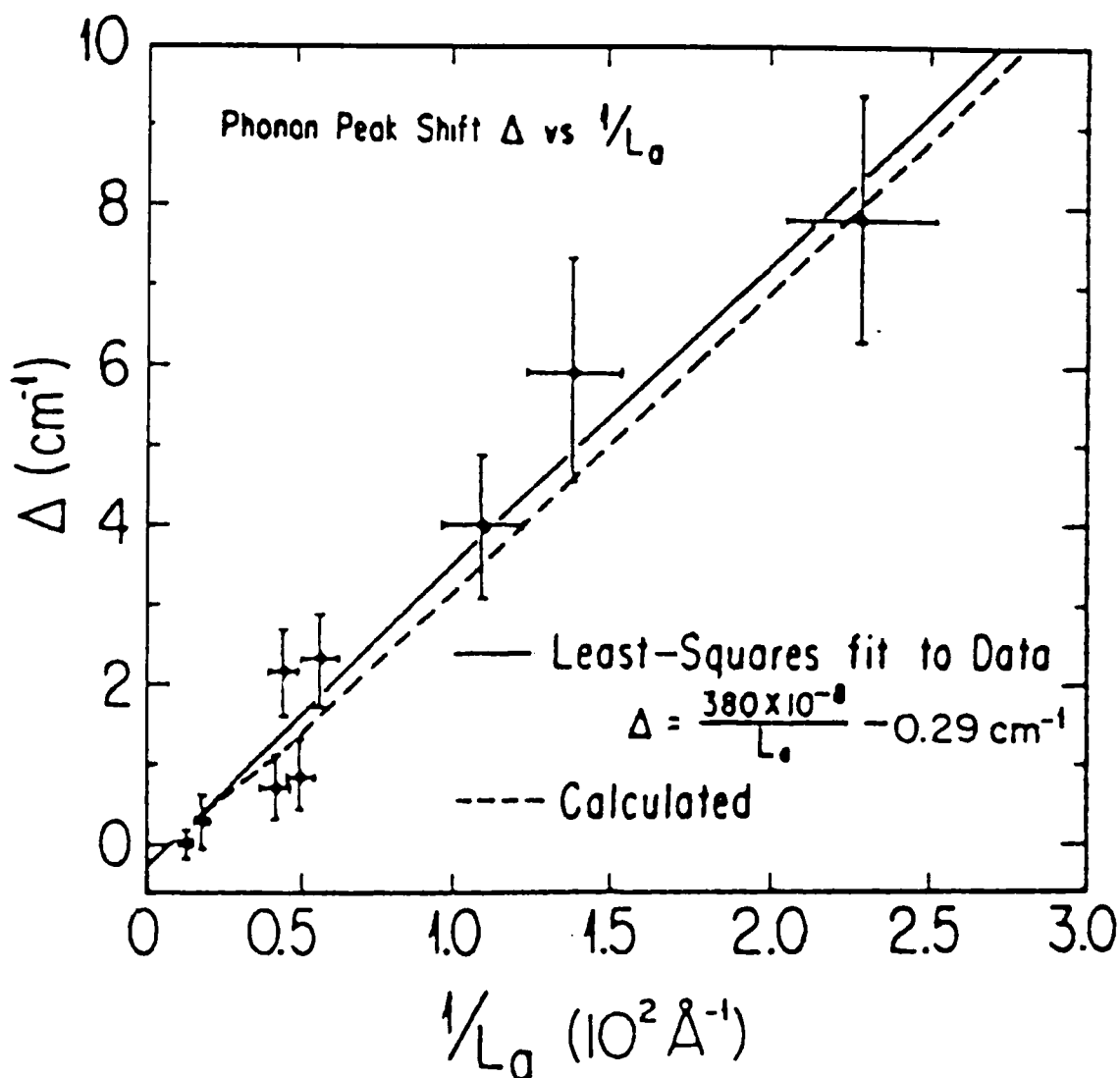
FIGURE 5. The dependence of the peak position (Δ) of the high-frequency E_{2g} mode vs. $1/L_a$ in microcrystalline BN.[28] The solid line is a least-squares fit to the data with the indicated values. The dashed lines represent the calculated peak position.

phonon Raman spectrum using the SC model with a Gaussian correlation function. As shown in Figure 7, the agreement between theory and experimental points is quite good over the entire range of Γ broadening and asymmetry Γ_a/Γ_b ($\Gamma = \Gamma_a + \Gamma_b$). In this case, alloying induces alloy potential fluctuations and hence the mode correlation becomes finite, giving rise to a relaxation of the q = 0 selection rule.[35]

2. DIRS (Disorder Induced Raman Scattering) Spectra

Figure 8 shows Raman spectra of several microcrystalline graphite samples with varying crystallite sizes (La).[38] While the spectra of the samples with small La show a DIRS line around 1360 cm^{-1} (D-peak), all spectra display the usual first order Raman line (G-peak) around 1580 cm^{-1}. Second-
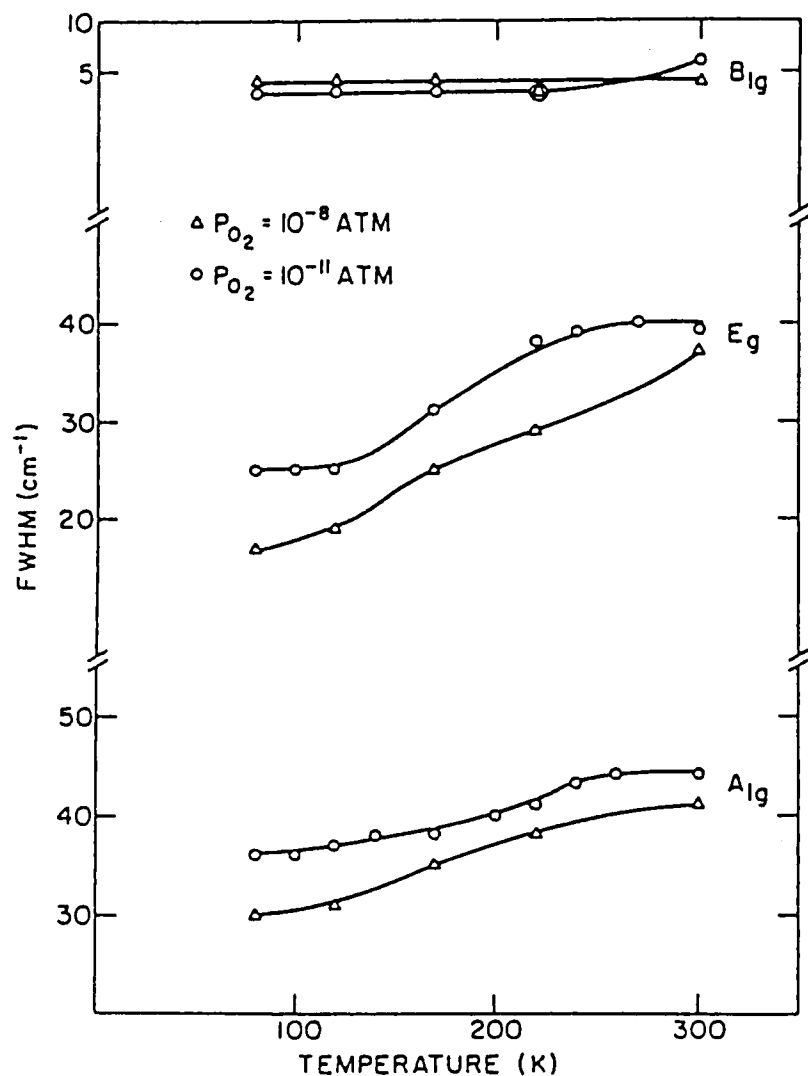
FIGURE 6. Raman linewidths for rutile crystals reduced at 10^{-8} and 10^{-11} atmospheres oxygen pressures.[33] The bands in highly reducing atmospheres are broader due to introduction of O-vacancies.

order Raman lines[39] are also shown in this figure. As La decreases, the intensity of the D-peak increases and in addition all the lines broaden. Nakamura et al.[50] studied a finite size effect for an electron-irradiated graphite with a wide variety of crystal size using microprobe Raman spectroscopy. The results indicated up and down shifts of the G-peak with decreasing crystal size. They showed that both shifts were explained in terms of the phonon dispersion relation and the wave vector uncertainty from La (q =

$2\pi/La$) and concluded that the La corresponds to the in-plane phonon correlation length (Figure 9).[25,50]

The Raman spectra of graphite are known to be very sensitive to structural changes. Even mechanical polishing induces a clear change in the spectra. After polishing a microcrystalline graphite sample, the intensity of the D-peak increased.[26,38]

Intercalation compounds of graphite were well characterized using Raman spectroscopy.[22,40] The intercalation stage depen-
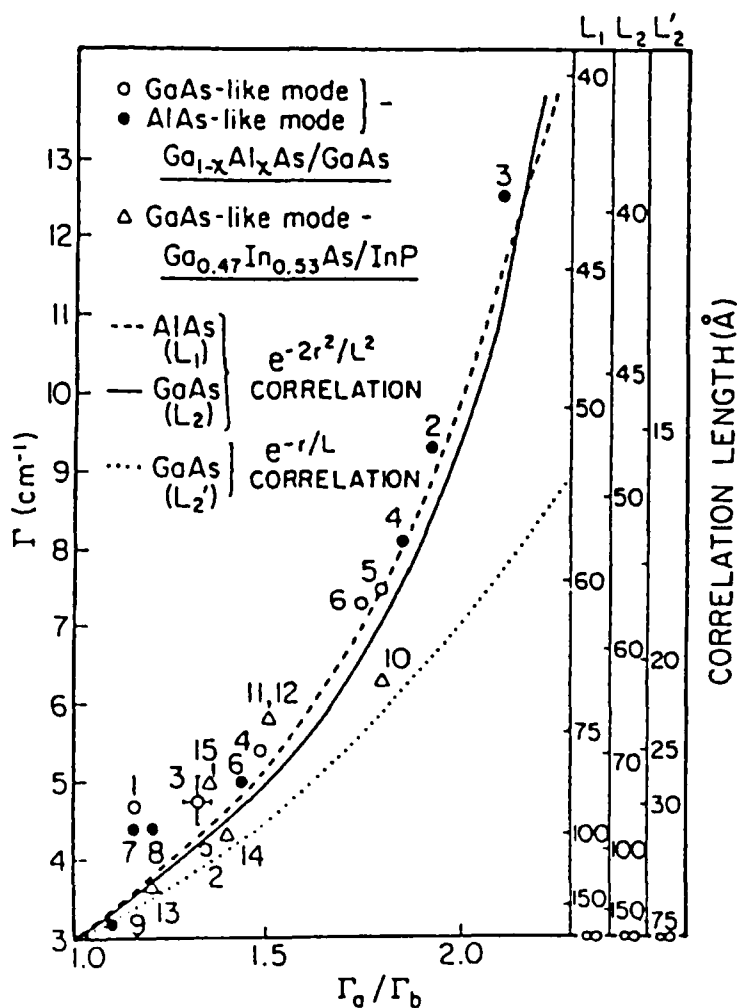
FIGURE 7. The relationship between broadening Γ and asymmetry Γ_a/Γ_b as a function of correlation length L in $Ga_{1-x}Al_xAs/GaAs$ and $Ga_{0.47}In_{0.53}As/InP$. The dashed line and solid line are calculated for AlAs dispersion (L_1) and GaAs dispersion (L_2), respectively, with use of exp $(-2r^2/L^2)$ as the correlation function. The dotted line shows the relationship for GaAs dispersion (L_2') using exp $(-r/L)$ spatial correlation. The experimental points for the various samples are also shown. (For details, see Ref. 34.)

dence of the Raman-active modes was found to correlate with a stage-dependent strain.

There are other reported DIRS lines in graphite by several authors. A phonon line at 1620 cm⁻¹ (D'-peak) was attributed by Lespard et al. to a nonzero phonon in a similar manner to the D-peak.[19] On the other hand, Nakamizo et al.[26] observed this line in oxidized graphite and suggested that it arises from CO stretching. Thus, for this line there is still room for argument. Recently, low-frequency DIRS bands have been reported for nanocrystalline glassy (g-) carbon having an in-plane correlation length of 3 nm.[27] Six major bands of DOS were observed at a frequency range of 100 to 1200 cm⁻¹ after annealing of amorphous carbon films at 600°C, suggesting the formation of quite small nanocrystallites having $La \approx 1.3$ nm (Figure 10).

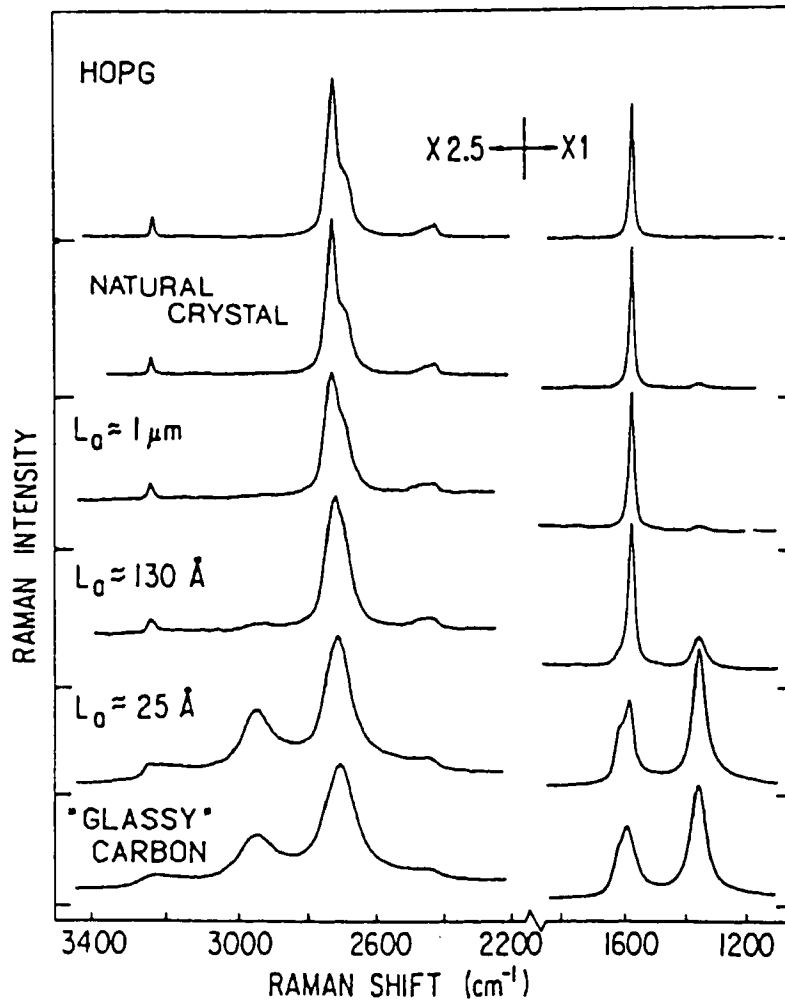DIRS spectra also occurs in other crystals. Let us make a brief description. Car-

FIGURE 8. First- and second-order Raman spectrum of several different forms of graphite.[38]

bon vacancies in cubic TiC_x induced a first-order Raman spectrum,[45] in the three independent components that were studied for x = 0.97, 0.90, and 0.80. In these non-stoichiometric titanium carbides, the spectra were not characteristic of isolated vacancies. The probabilities for clustering of vacancies were discussed, and the vacancy clusters may have been of finite size for $TiC_{0.90}$ and $TiC_{0.80}$. In rutile, a broad band at 235 cm^{-1} was considered to be disorder-induced.[46-48] In As^+-, Si^+-, or Sn^+-implanted GaAs crystals, three broad bands around 80, 175, and 250 cm^{-1} were reported to be DIRS peaks[6,15,54] (the effects of ion-implan-

tation will be discussed in detail in the following sections). For μc - silicon, a relaxation of the selection rules allowed strong scattering around 630 cm^{-1} from (TO + TA) combinations. This line could be a second-order DIRS line.[36,37]

B. Ion-Implantation Effects

Ion implantation provides a physical mechanism for the introduction of foreign species into host materials. Simultaneously the kinetic energy introduces lattice disorder and radiation damage that affects vari-

288
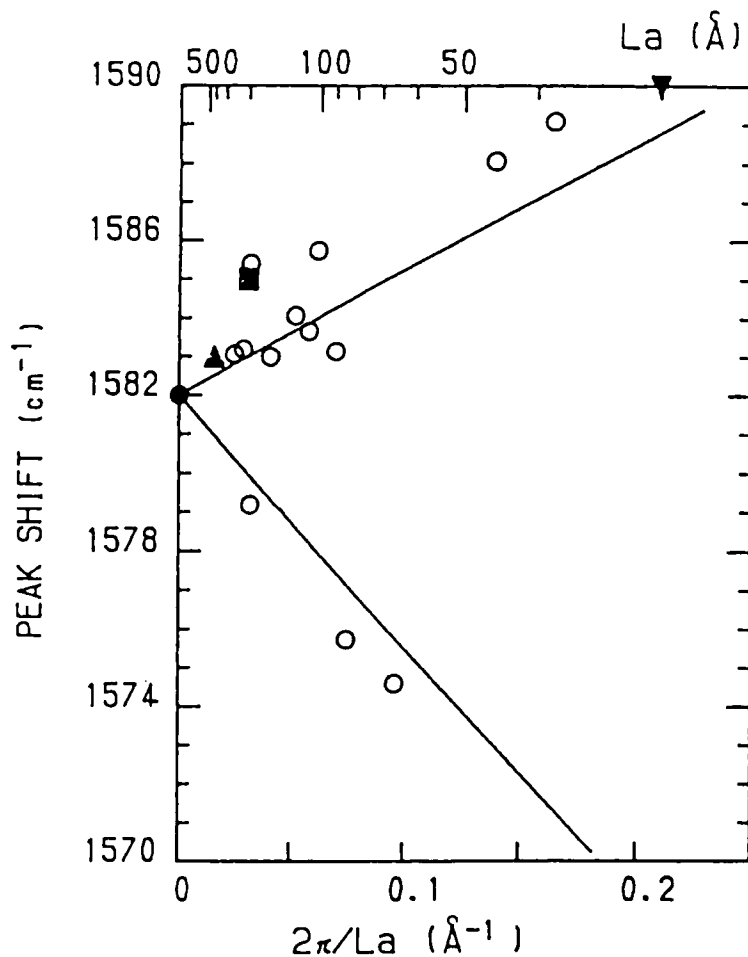
FIGURE 9. Raman shift of E_{2g} mode peak vs. $2\pi/La$ in graphite with a wide variety of crystal size; open and solid points indicate experimental values. The solid line shows the result of calculation with the phonon dispersion relation. (See Ref. 50 and references therein.)

ous physical properties of the host material. Therefore, the lattice damage must be probed.

1. Damage Profile and Optical Penetration

The implanted crystals exhibit damage profiles depending on the ion energy, ion mass, and substrate material. Detectable Raman scattering intensity depends on the optical penetration depth because the incident and scattered light are absorbed by the substrate material. In Figure 11, examples of damage profiles for Si^+ ion bombardment into silicon are shown. This figure includes the profiles for 200 keV and 1.5 MeV Si^+ ion implantation calculated[14] using TRIM-code,[58] to demonstrate a difference in the profile caused by the large difference in energy. The optical penetration d_{opt} in virgin silicon is approximately 500 nm for 488-nm incident laser. The depth distribution of damage for the 200 keV Si^+ implantation
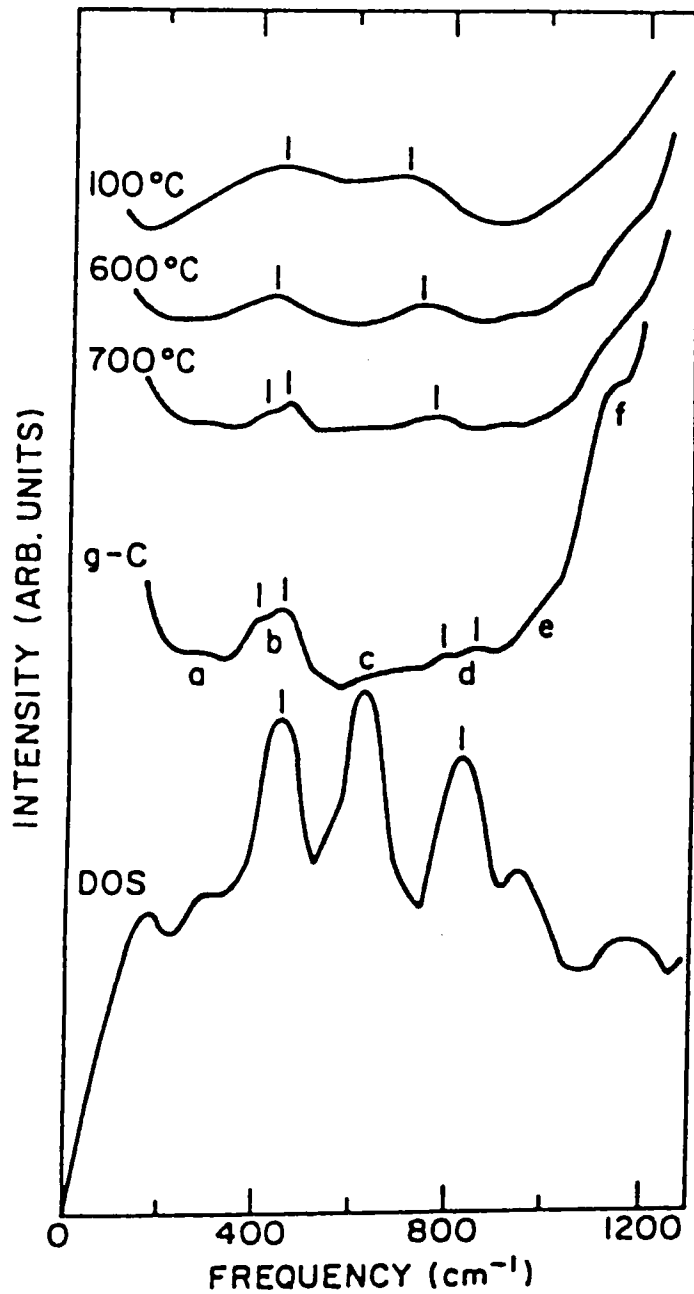
FIGURE 10. Comparison of the low-frequency DOS of *g*-C with Raman spectra of *g*-C and initially *a*-C films annealed to 100, 600, and 700°C.[27] Vertical lines denote selected peak positions.

is within the probing depth, and the Raman technique covers all the damaged region for keV ion implantation, although the damage distribution is highly non-uniform. On the other hand, for 1.5 MeV, the damage is reasonably flat within the optical penetration depth of the laser to detect a unique level of damage, although Raman techniques monitor only a portion of the damage within d_{opt}.

The optical penetration depth d_{opt} is dependent on the material, incident light
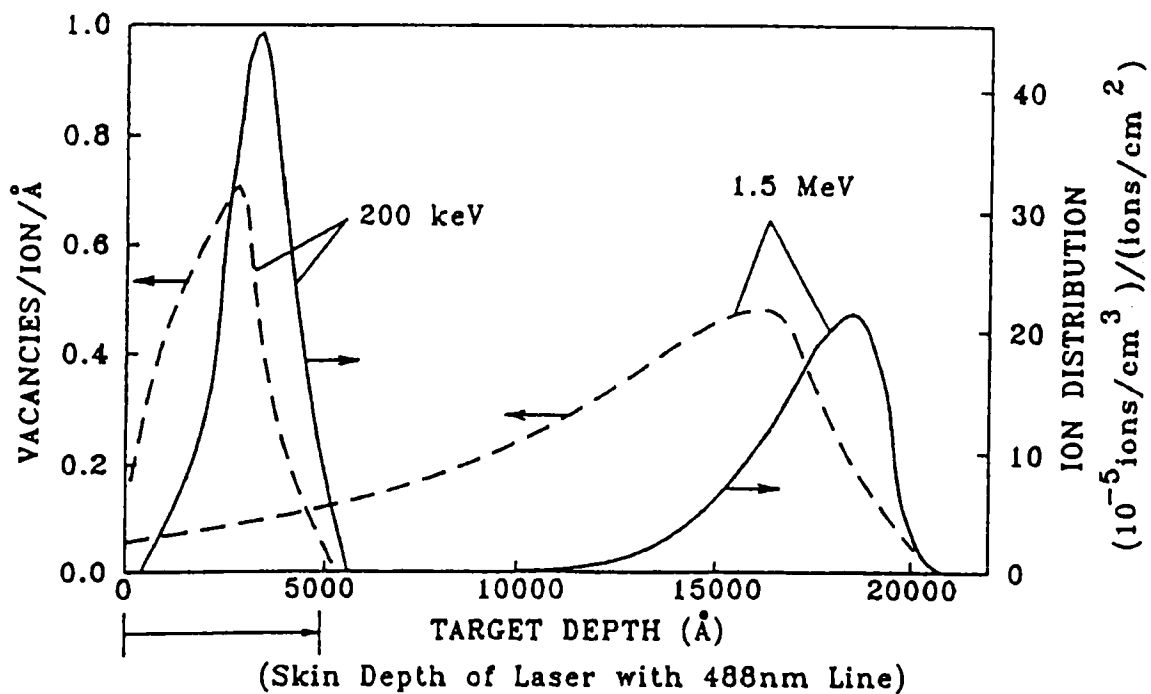
FIGURE 11. The distributions of implanted Si ions (solid line) and total target vacancies (dotted line) for 200 keV- and 1.5 MeV-Si ion implantation into silicon.[14]
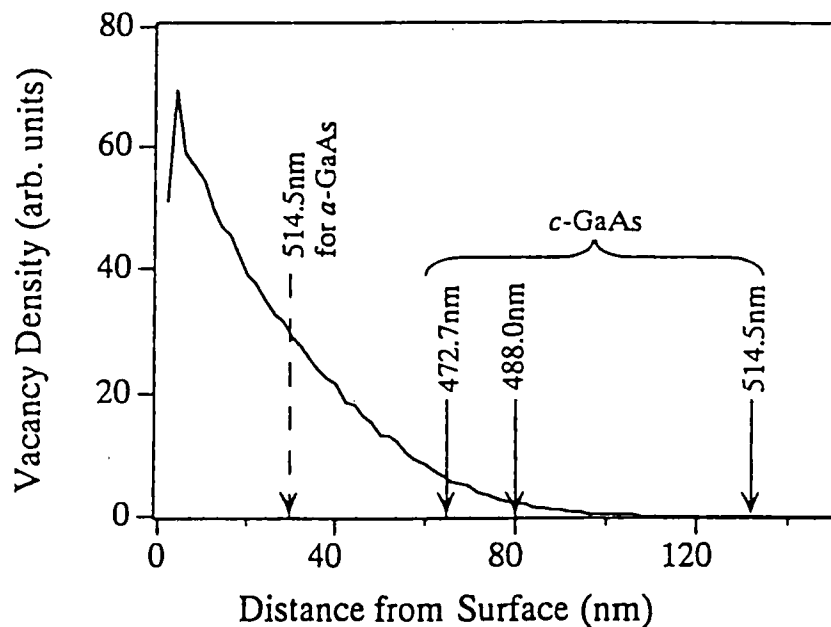
FIGURE 12. The depth profile of the vacancy distribution for 5-keV He+ ion irradiation on GaAs obtained from TRIM calculation. The solid arrows indicate the optical penetration depths of the 514.5-, 488.0-, and 472.7-nm lights in crystalline GaAs (c-GaAs), and the broken arrow indicates that of the 514.5-nm light in amorphous GaAs (a-GaAs).[59]

wavelength, and incident angle. This effect is delicate for keV order ion bombardment because the penetration depth is comparable with the depth of damage profile. In Figure 12 the damage profile for 5-keV He$^+$ ion bombardment and the optical penetration depth for GaAs[59] are shown. d_{opt} for 488-nm wavelength light in crystalline GaAs is 80 nm and comparable with the damage profile for 5 keV He$^+$ ion bombardment. d_{opt} is smaller for shorter wavelengths of light. Further, it also depends on the degree of disorder. For wavelengths of about 500 nm (this is a usual wavelength of the incident laser), d_{opt} decreased as the structure became disordered due to ion bombardment;[60–63] as an extreme case d_{opt} of amorphous GaAs reduced to about 1/5 of the single crystal.[62]

2. Semiconductors

Ion implantation in semiconductors is a process of considerable technological importance as well as a method of producing controlled damage for studying the nature of these solids. Raman spectroscopy is an extremely useful tool for obtaining information about the state of materials, as it depends on lattice excitations and is therefore an important complement to spectroscopies depending on electronic state. A lot of Raman studies on lattice disorder in ion-implanted or etched semiconductors have been reported.[6,14–16,51–56] In this section we discuss in detail the phonon correlation length, spectral asymmetry, Raman scattering depth profile, and other related properties that have been obtained from Raman scattering from ion-implanted semiconductors.

a. Ion Implantation and the SC Model

First we discuss applications of the SC model to Raman spectral shape changes in ion-implanted semiconductors. Tiong et al.[15] showed for the first time that phonon line shapes (broadening and asymmetry) and position changes resulting from ion implantation in semiconductors could be explained in terms of the SC. They investigated Raman scattering from (100) GaAs samples implanted with 270-keV As$^+$ ions with various doses up to $3.2 \times 10^{14}/cm^2$. In Figure 13, the longitudinal-optic (LO) phonon for both unimplanted and $2.4 \times 10^{13}/cm^2$ implanted samples is shown. The full width at half-maximum (FWHM), $\Gamma = (\Gamma_a + \Gamma_b)$, is indicated on both spectra, where Γ_a is the left half width and Γ_b the right half width. The LO phonon line for the implanted sample has (a) shifted to lower frequencies and (b) broadened asymmetrically ($\Gamma_a > \Gamma_b$), following the phonon dispersion relation as was discussed in Section III.A. The frequency shift and broadening of the LO phonon line was analyzed based on the SC model. Γ_0 was 3.0 cm^{-1}, and for the dispersion $\omega(q)$ they used an analytic model relationship $\omega(q) = 269.5$ cm^{-1} + 22.5 cm^{-1}, which closely reproduced the actual dispersion relation of GaAs along (100).[57] Figure 14 shows the shift $\Delta\omega_{LO}$ and Γ of the LO line as a function of L as evaluated from Eq. 14 (solid line). From Eq. 14 we are also able to evaluate the asymmetry Γ_a/Γ_b in relation to $\Delta\omega_{LO}$ for various L. This is represented by the solid line in Figure 15 together with the experimental values. The agreement in both cases is quite good. Thus, they claimed that from the SC model, Eq. 14, it is possible to relate the shift, broadening, and asymmetry of the LO phonon for a given dose to an average (undamaged) particle size.

Next we show another example of Raman scattering in an ion-implanted semiconductor with an ion energy of MeV order, where the implanted sample has a nearly uniform distribution of defects within the optical penetration depth (Figure 11). Figure 16 shows phonon Raman spectra of 1.5 MeV Si$^+$ ion-implanted silicon with doses
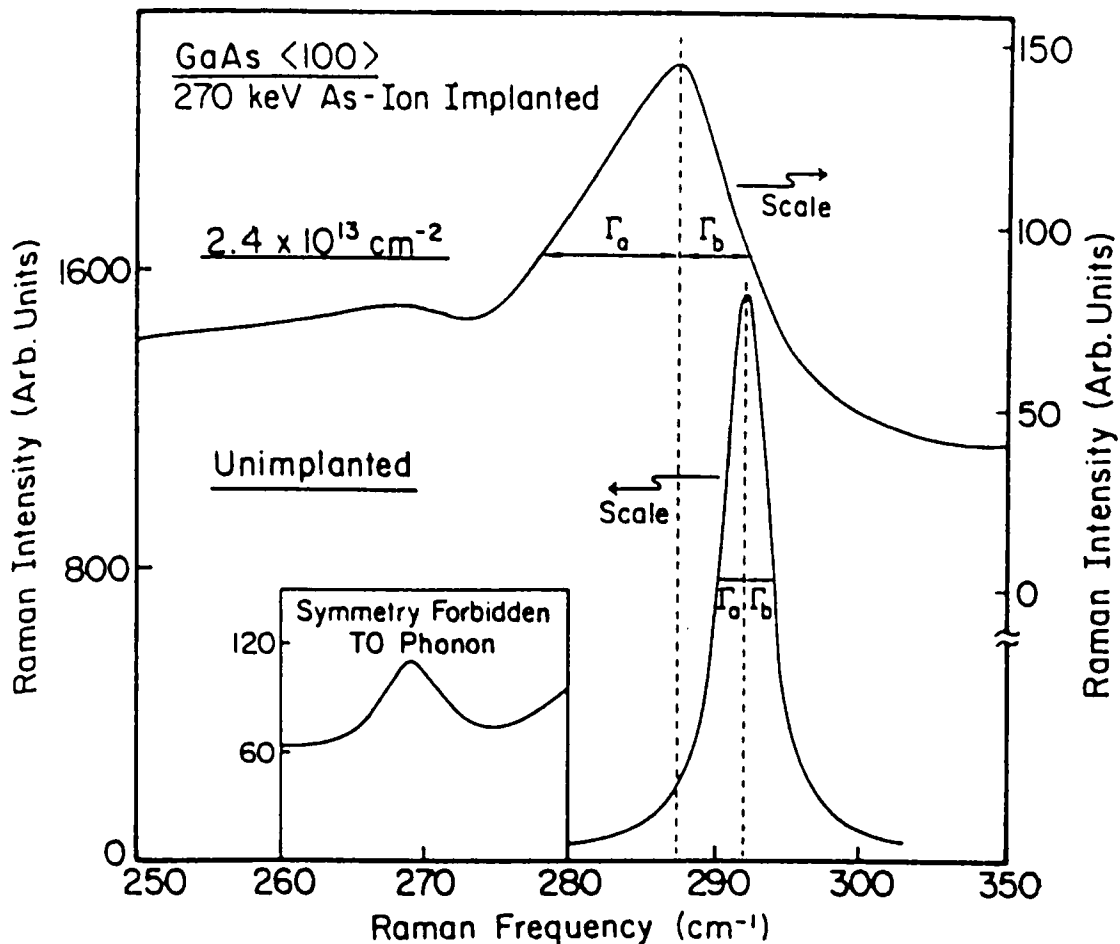
FIGURE 13. LO phonon Raman spectra of GaAs (100) before implantation and implanted up to a dose of 2.4 × 10¹³ As/cm² for 270 keV As⁺ implantation.[15]

ranging from 1×10^{11} up to 1×10^{15} Si/cm². The Raman lines start to broaden asymmetrically for doses above 1×10^{13} Si/cm². The solid lines are fitted curves to the experimental values using the SC model modified by introducing a term attributable to residual stress. In Figure 17 the asymmetry Γ_a/Γ_b as a function of the ion dose is plotted. Γ_a/Γ_b increases with increasing the ion dose, and the model quite well reproduced the experimental curve.[14]

b. Optical Absorption by Defects

The spectral effects produced by very low-energy bombardment are very differ-ent from those by high-energy ion implantation. Raman spectroscopy on GaAs surfaces bombarded with 3.89 keV Ar⁺ ions showed no line shift and broadening of LO Raman line for a dose of 1×10^{17} Ar/cm².[64] This is because the full damage layer is very small compared with d_{opt}, and the Raman technique probes even undamaged layer structures. Thus the Raman intensity of the LO line was only about 1/5 that of crystalline (c) -GaAs. The optical absorption coefficient in the damaged layer near the surface increased, due to the high density of point defects. In other words, d_{opt} decreased, resulting in a decrease in the Raman intensity[62,64] (Section IV.B.1). This also provides
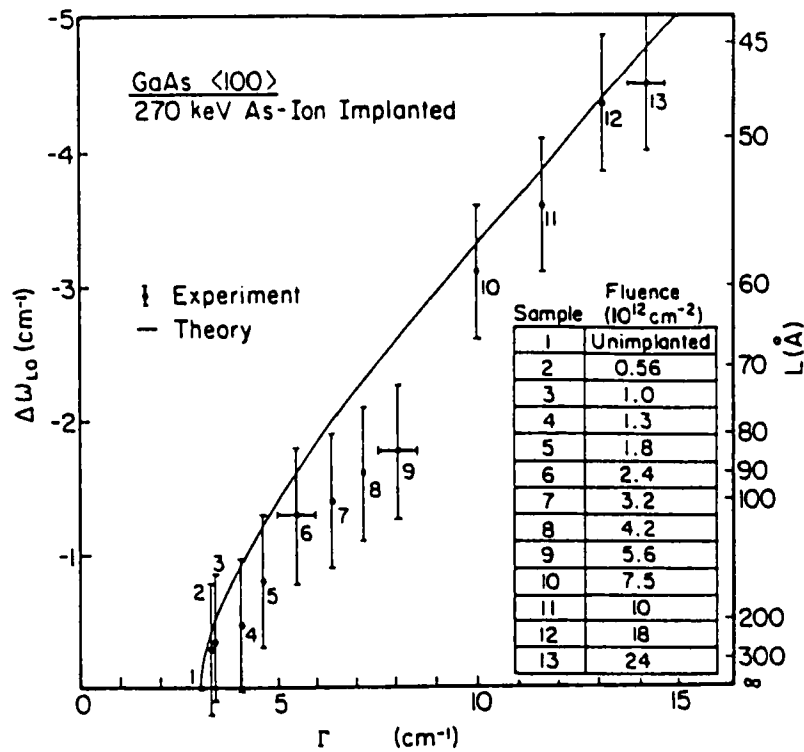
FIGURE 14. LO phonon Raman shift $\Delta\omega_{LO}$ and broadening Γ as a function of L as determined from Eq. 14 (solid line). Also shown are the experimental values of $\Delta\omega_{LO}$ and Γ for various doses.[15]

information on the defect density near the surface, as described later.

c. Raman Scattering Depth Profile

Implanted samples exhibit a damage distribution in the implanted area (Section IV.B.1). It is of interest to use Raman scattering depth profile analysis to reveal the structural damage dependence on depth. The combination of Raman scattering with chemical-etch removal of near surface layers makes it possible.[6,16,52] Figure 18 shows Raman spectra for a c-GaAs sample implanted with 1×10^{14} Si/cm^2 at 1 MeV, taken by Braunstein et al.[16] at the original surface of the sample and after etching 400, 900, and 1400 nm. The chemical etching for the

depth profiling was performed using a solution 50:3:3:CH$_3$OH:H$_3$PO$_4$:H$_2$O$_2$. The LO phonon seen around 290 cm^{-1} shifts to lower frequencies, broadens, and decreases in intensity with increasing depth, from the surface down to 900 nm. However, after 1400 nm were removed, the LO line becomes narrow again and returns almost to the frequency shift corresponding to unimplanted GaAs. The intensity of the transverse optic (TO) mode around 260 cm^{-1} showed a little different behavior: the intensity increased with increasing depth from the surface down to 900 nm. The frequency shift of the LO mode as a function of depth for a GaAs sample implanted with 1 MeV Si$^+$ ions is shown in Figure 19. In the same figure the nuclear energy loss of the implanted ions is drawn. The energy loss, which results in the creation of lattice disorder, was calculated
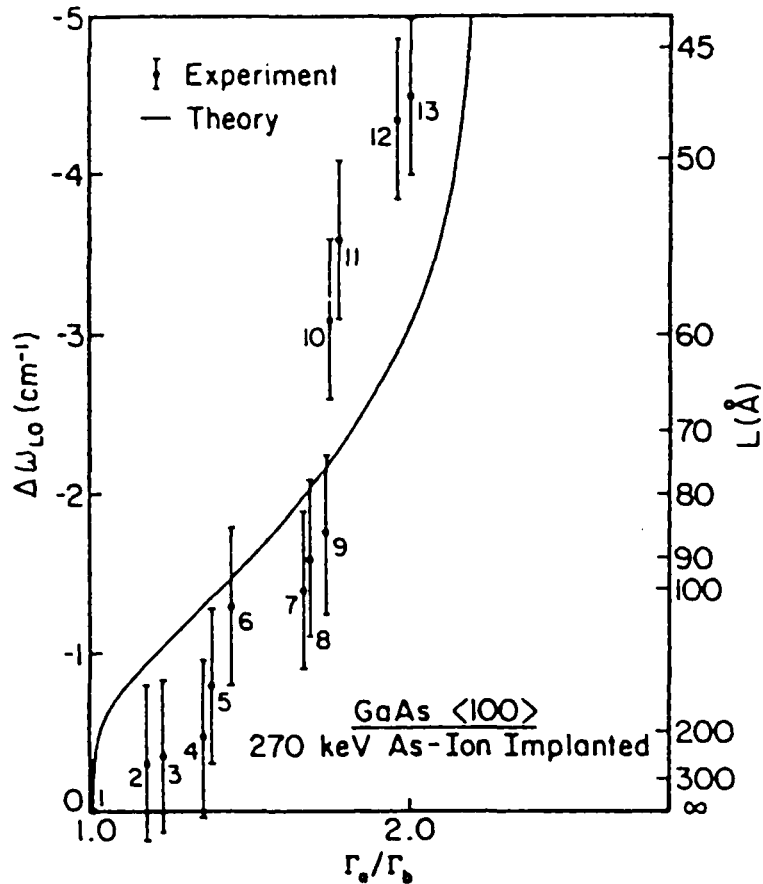
FIGURE 15. Relationship between the LO Raman shift $\Delta\omega_{LO}$ and asymmetry, Γ_a/Γ_b as a function of L as determined from Eq. 14 (solid line). Also shown are experimental values for $\Delta\omega_{LO}$ and Γ_a/Γ_b for various doses.[15]

by TRIM code. It is evident that the LO shift follows well the nuclear energy loss curve. This observation has two implications: first, the shifts in the LO frequency provide a good gauge of the lattice disordering, and, second, the depth profile of the lattice disorder monitored by the Raman technique is closely related the nuclear energy loss.

The depth profile of L was obtained for an ion implanted GaAs. Figure 20 shows a comparison of experimental and theoretical damage profiles for GaAs implanted with 45 keV Be^+ at a dose of 5×10^{14} Be/cm².[52] Data points symbolized by solid circles are $1/L$. L was obtained from the line widths and frequency shifts of the LO mode based

on the SC model. For comparison with experimental results, Figure 20 also includes two widely used theoretical estimates of damage profiles: (Lindhard-Scharff-Schiott)[65] LSS and TRIM. The broad maximum in the TRIM calculation agrees fairly well with the extent of the high-damage (short L) plateau of the experimental curve. To restate, the idea of phonon confinement well explains the observed Raman line shape changes during depth profile analysis of lattice disorder produced by ion implantation to semiconductors.

The depth profiles could also be obtained by using incident laser lights with different wavelengths. The Raman scattering depth profile obtained by this method
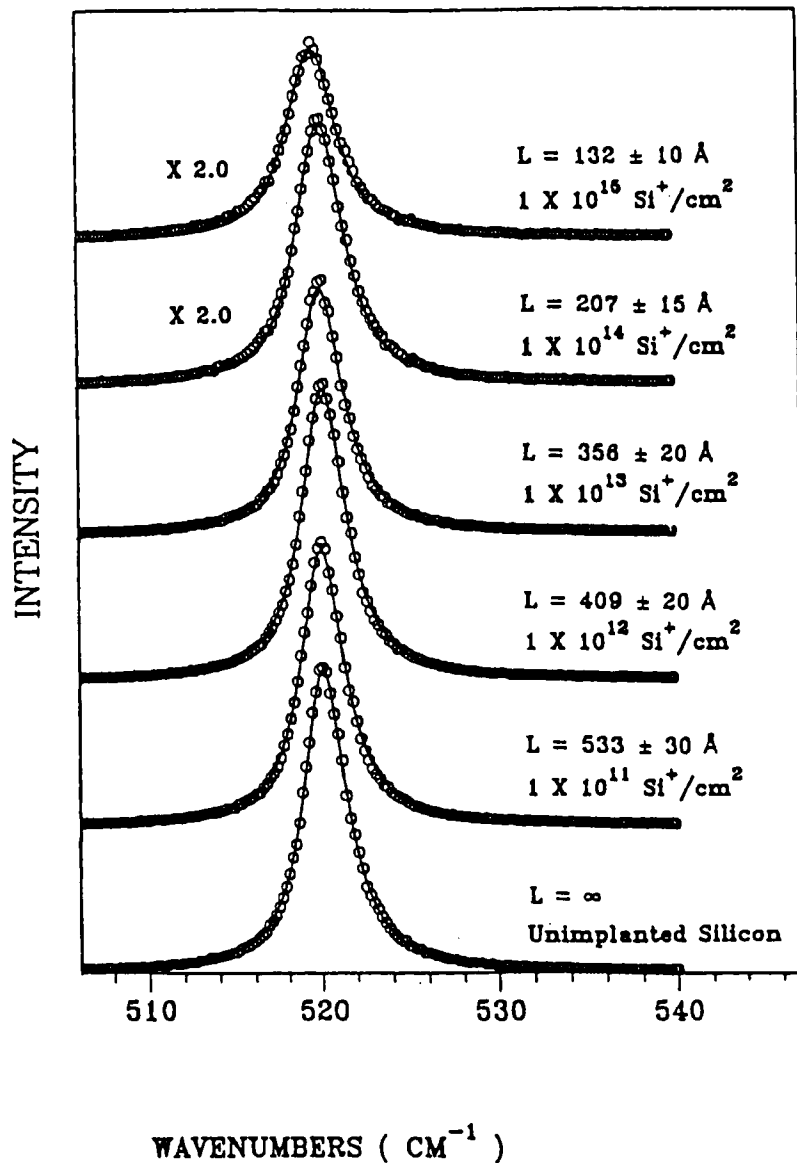
FIGURE 16. Raman spectra of 1.5 MeV Si+ implanted silicon with doses ranging from 1 ×10^{11} Si+/cm^2 to 1 × 10^{15} Si+/cm^2. Circles: experimental spectra; solid line: the modified SC model fit to the data.[14]

revealed a weaker long-range disordering in the surface area (≈20 nm) followed by a stronger long-range disordering in an amorphous Si produced by self-ion implantation.[56]

d. Resonant Raman Scattering and the LO Phonon-Plasmon Coupling

Resonant Raman scattering can be a sensitive probe of defects in ion-implanted semiconductors. Holtz et al.[53] observed a strong feature near 47 cm^{-1} (A) in the first-order Raman spectrum of c-GaAs implanted with 45-keV Be+ ions as shown Figure 21. As the implant dose increases, the LO line (292 cm^{-1}) shifts downward or decreases, broadens, and the amorphous (a)-GaAs three-band continuum increases in intensity. Simultaneously, line A increases in intensity with dose. There was a clear photon

FIGURE 17. The asymmetric broadening of Raman peak of Si as a function of ion dose (1.5 MeV Si⁺). The solid line is a guide to the eye.[14]
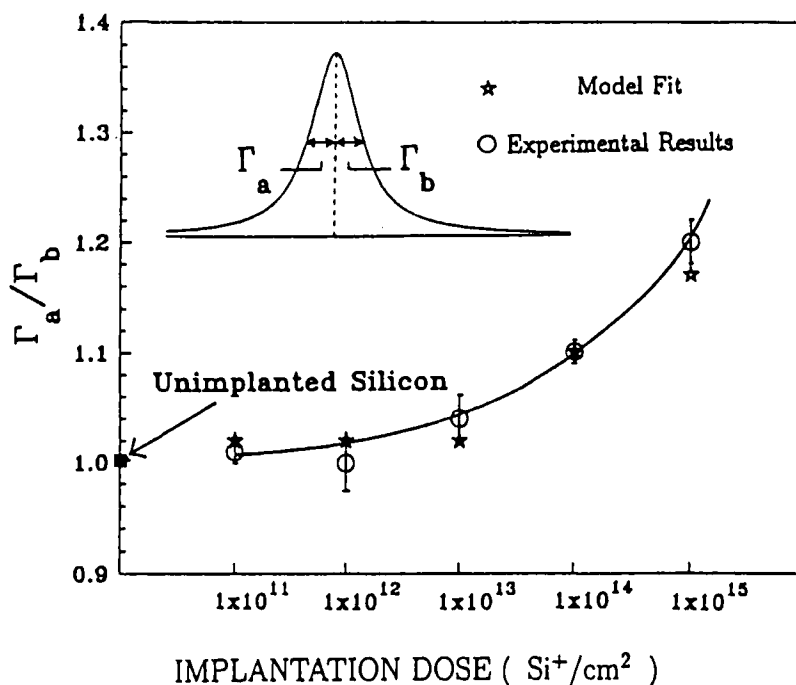
energy dependence of the A line intensity with a peak around 1.7 eV (730 nm) (Figure 22). This result was interpreted as strong evidence of a resonance at an energy midway between the E_0 and $E_0+\Delta_0$ interband electronic transitions. They further measured the hydrostatic-pressure dependence on the Raman spectra in the implantation disordered GaAs and found that the A mode shifts weakly (-0.07 ± 0.15 cm^{-1}/GPa), while the LO mode shifts strongly (3.6 ± 0.1 cm^{-1}/GPa). Then they identified the resonant vibration (A) of this band as stemming from the breathing mode of the Ga vacancies.[66] It was reported that resonant two-LO phonon scattering is also very sensitive to either ion implantation-induced disorder or the increase in lattice perfection by thermal annealing.[51]

For heavily doped n-GaAs (2×10^{18}/cm^3), Wang et al. found that Raman scattering of coupled LO phonon-plasmon

modes proves to be a very sensitive tool for assessment of dry-etch-induced damage.[67] The etch-induced damage can be both structural and electronic. The electronic damage acts as electronic traps that can reduce or deplete the free carriers in the materials and can be assessed by analyzing the relative intensity changes with respect to unscreened LO phonons in the surface depletion layer. They demonstrated that electron cyclotron resonance radio frequency reactive ion etching (ECR-RIE) produced little damage compared with conventional RIE or ion beam etching and is an attractive technique for semiconductor nanostructures.

3. Graphite and Related Materials

Raman spectroscopy is a sensitive tool for monitoring ion irradiation processes
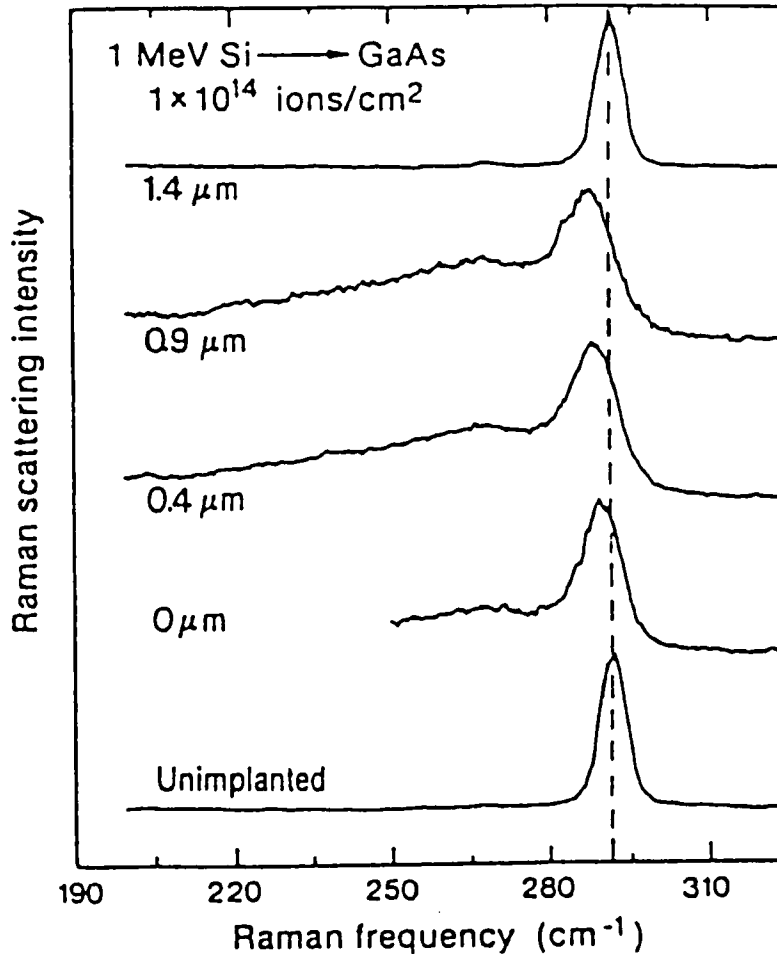
FIGURE 18. First-order Raman spectra of GaAs implanted with 1-MeV Si⁺ ions to a dose of 1 × 10¹⁴ cm⁻² taken on the original surface of the sample and after etching away. 0.4, 0.9, and 1.4 μm, respectively.[16]

in graphite, as ion implantation usually takes place within the optical penetration depth and Raman scattering in graphite is very sensitive to the lattice disorder (Section III.B). There are a large number of papers on Raman scattering from carbon materials irradiated with energetic ions. These papers are characterizing microscopic structural properties, in connection with the studies of ion implantation,[69,70] intercalation graphite compounds,[22] and plasma surface interactions of first wall in fusion devices.[71-73]

As an implanted ion (typically an order of keV energy) slows down and comes to

rest, it makes many violent collisions with lattice atoms, displacing them from their lattice sites. Some of these displaced atoms have enough kinetic energy to displace others, giving rise to a cascade process. The net result is the production of a highly disordered region around the path of the ion with the dominant disorder occurring near the end of the ion trajectories, as shown Figure 23a.[70] At sufficiently higher doses, the individual disordered regions begin to overlap (Figure 23b) until finally a noncrystalline or amorphous layer is formed (Figure 23c). Such a mechanism is well known for Si and Ge.[70]
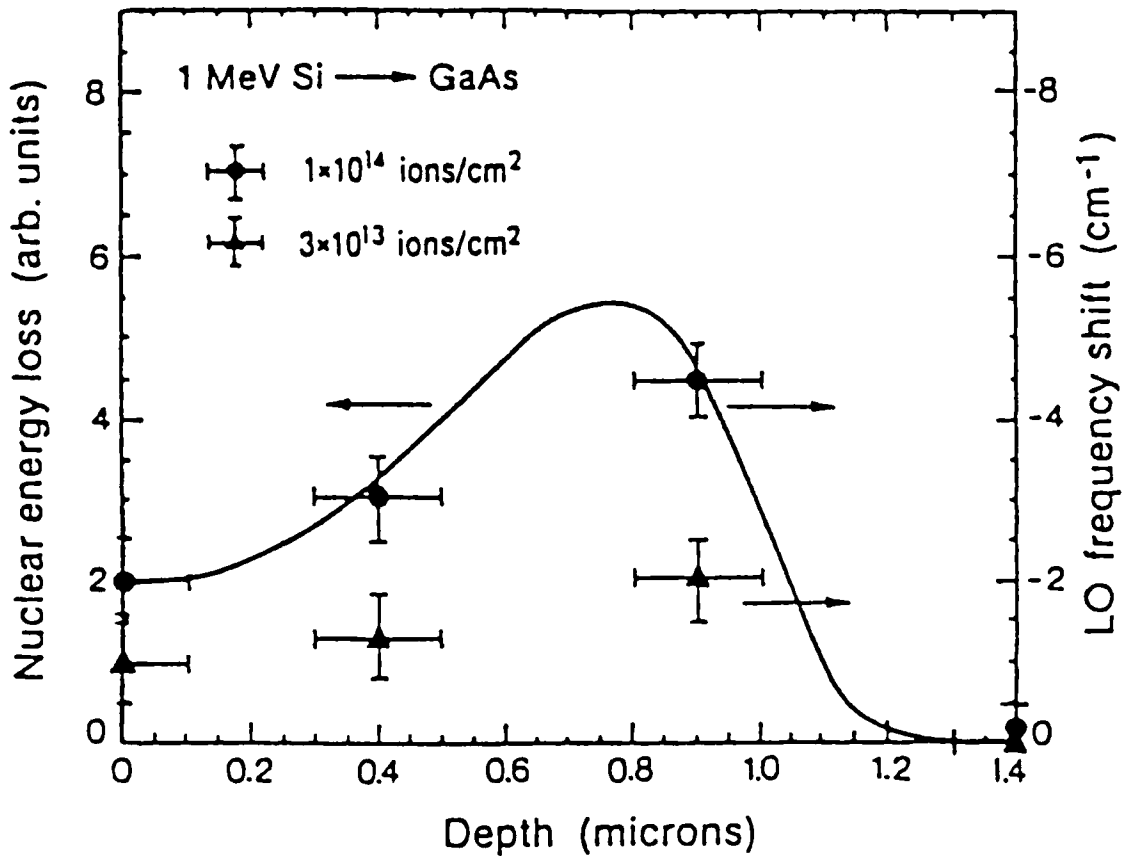
FIGURE 19. LO-phonon frequency shifts, after various etch steps, for 1-MeV Si⁺ implanted into GaAs at doses of $1 \times 10^{14} \text{cm}^{-2}$, and $3 \times 10^{13} \text{cm}^{-2}$ compared to the depth profile of nuclear energy loss (i.e., radiation-damage depth profile) (solid line).[16]

a. Ion Dose and Mass Dependence

Since the first measurements by Smith et al.[68] on graphite irradiated with Ar⁺ ions, ion-irradiated graphite has been studied extensively using Raman scattering. Elman et al.[69,70] systematically studied Raman scattering from graphite (highly oriented pyrolytic graphite: HOPG) implanted with ion doses in the range $1 \times 10^{14} - 2.5 \times 10^{16}$ ions/cm² with various ions and energies in the range 40 to 200 keV. We can say that the technical information obtained there underlay the Raman spectroscopic studies on the ion irradiation-induced defect structure in graphite. Let me explain their results. Figure 24 shows Raman spectra of HOPG

graphite irradiated with 100 keV B⁺ ions at various doses. The Raman spectrum of the virgin HOPG has only a sharp G-peak at 1580 cm⁻¹ (Figure 8). Disorder produced by ion bombardment induced the D-peak near 1360 cm⁻¹. This figure shows a gradual increase in the relative intensity ratio (R) of the D-peak and linewidths of both lines as the dose increased from 1×10^{14} to 1×10^{15} ions/cm², indicating an increase in the degree of disorder. As the dose is further increased to 5×10^{15} ions/cm², a dramatic change in line shape occurred. The dose dependent linewidth of the D-peak shown in Figure 25 indicates that an abrupt transformation to an amorphous layer occurs at a critical dose.
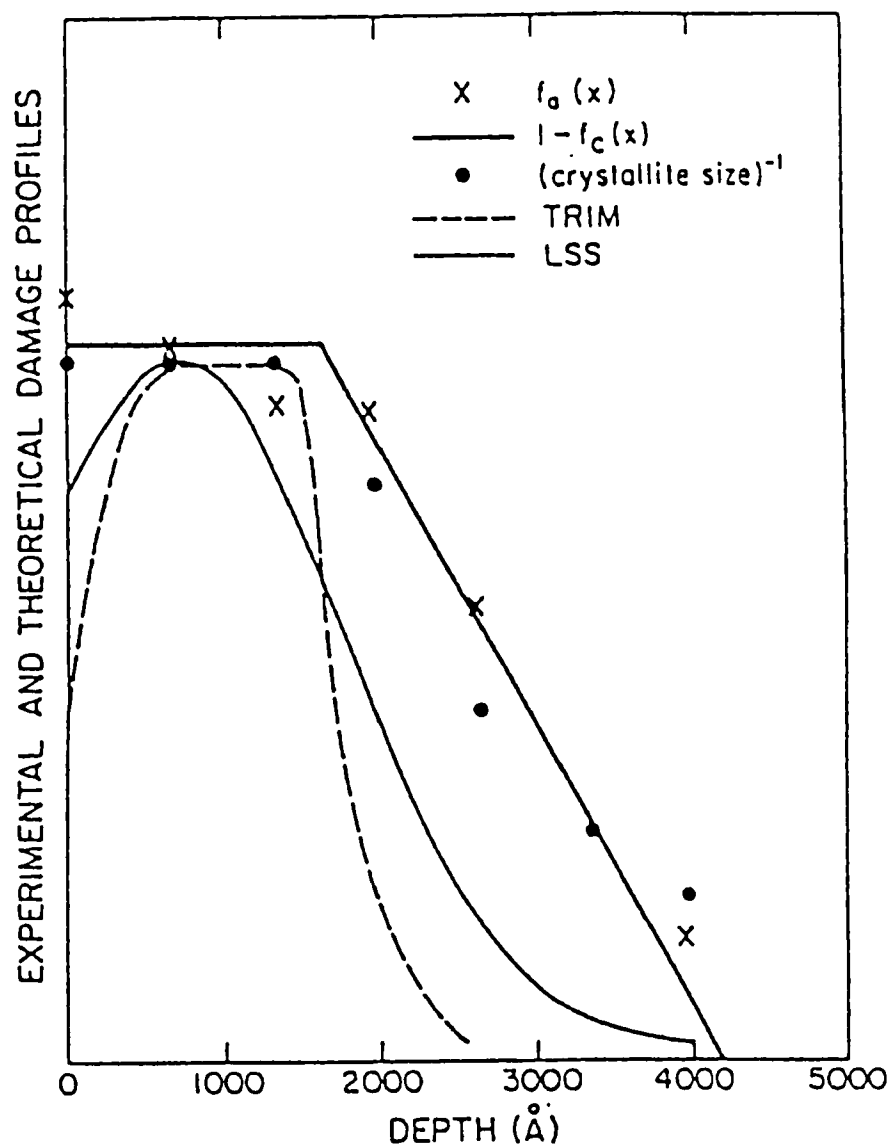
FIGURE 20. Experimental results for the structural depth profile of ion-implanted GaAs (45-keV Be$^+$, 5 × 10^{14}-cm^{-2} case). Solid circles denote reciprocal crystallite sizes L obtained from the LO line-shape data. The two curves are theoretical calculations included for comparison.[52]

The Raman spectra of ion-implanted graphite also depends on the atomic mass of the implanted species.[69] In Figure 26 the FWHM of the D-peak vs. the ionic mass for different doses at 100 keV are shown. The figure shows the onset of a rapid increase in the linewidth of the D-peak for ion mass m > 27 (i.e., Al ions) and a dose of 1 × 10^{14} ions/cm^2. Elman et al. explained the onset of the rapid increase by comparing the val-

ues of d_{opt} and $(P - \Delta P - P_s)$, where P is the projected range of the ion, ΔP the ion straggling, and P_s the length of highly damaged graphite region.[70] The onset of the rapid increase corresponded to satisfying the condition $d_{opt} = P - \Delta P - P_s$. For lower doses (then small P_s) and very light ions, the highly damaged region could not be probed by the Raman scattering, because $(P - \Delta P - P_s)$ in general larger than d_{opt}. Therefore, the

300
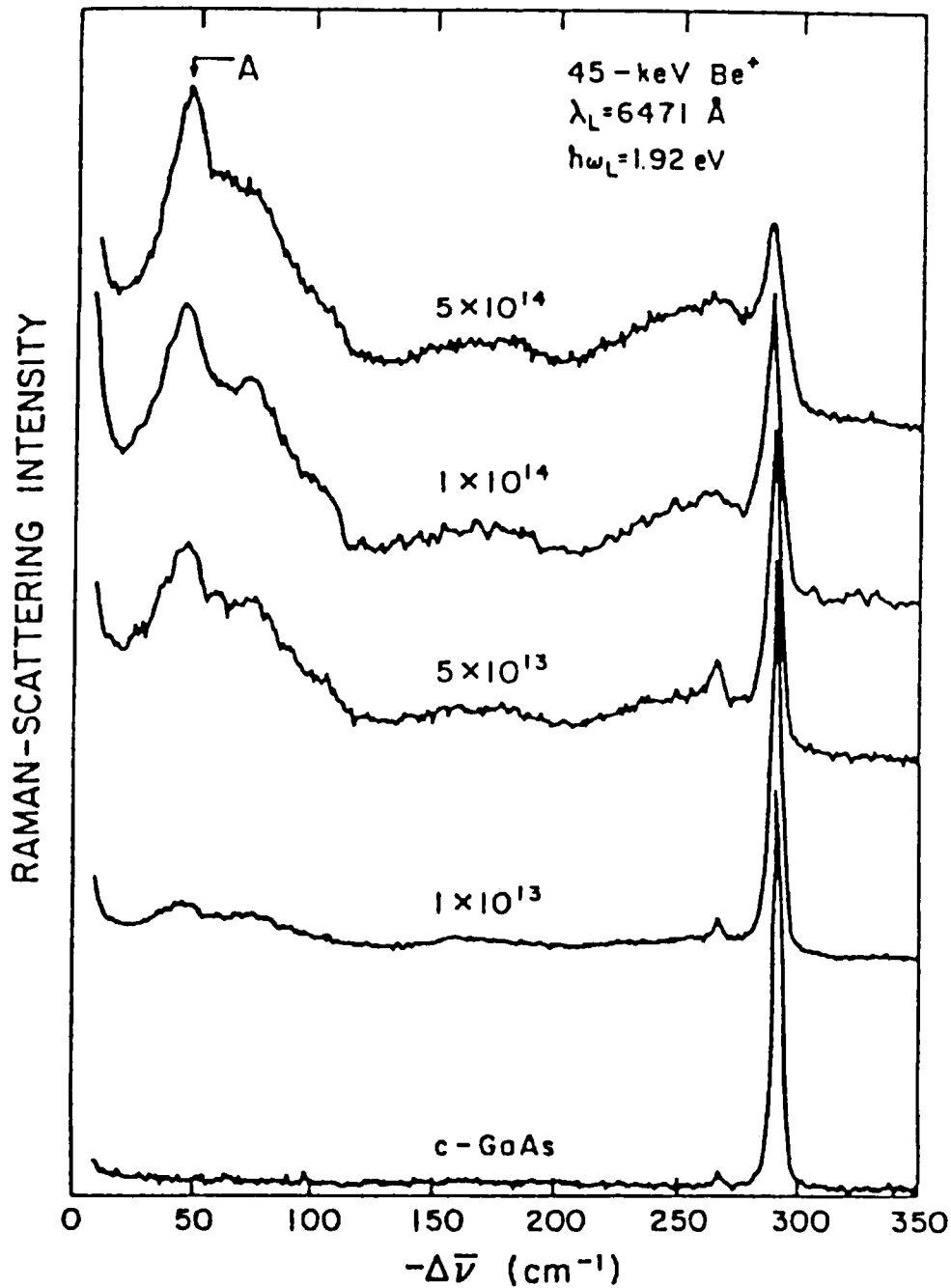
FIGURE 21. Unpolarized, room-temperature Raman spectra for (100)-oriented GaAs crystals and for crystals implanted with 45-keV Be⁺ ions to various doses, measured in ion/cm². Excitation was with a red light.[53]

observed line is narrow. When the ions are heavy, the damaged region could be probed because $(P - \Delta P)$ is small, resulting in the wide Raman line. The onset occurs for lower ion masses as the ion dose increases, because P_s becomes large in this case. Thus, it is possible to estimate the length of the highly damaged region (P_s) from the onset of the rapid increase in the linewidth, as d_{opt} and $(P - \Delta P)$ are known.[70]

A similar ion mass dependence was observed on R (Eq. 15) as shown in Fig-
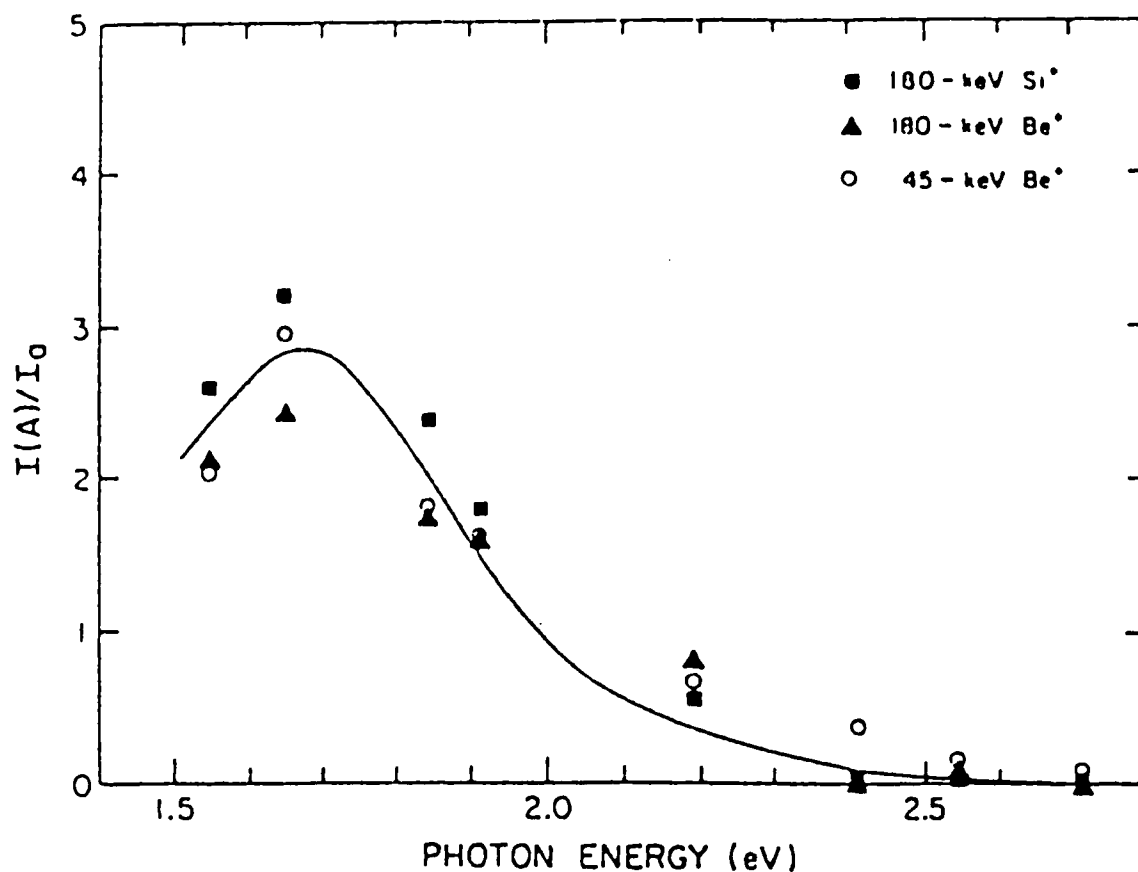
FIGURE 22. Intensity of band A (47 cm⁻¹), relative to that of amorphous band vs. excitation energy for ion-implanted GaAs.[53]

ure 27. R starts to saturate above a certain ionic mass, depending on the ion dose, with maximum value of approximately 1.6, which corresponds to $L_a \approx 2.5$ nm. They further confirmed that the D′-peak near 1620 cm⁻¹ is another type of DIRS induced by ion irradiation (Section IV.A.2).

Recently, Niwase and Tanabe performed a series of studies on the defect structure and amorphization of graphite irradiated by light ions (proton, helium ions, etc.).[72,74,75] They summarized the disordered structures by mapping with the line width of the G-peak and R. Figure 28 is the schematic drawing of the change in the linwidth and R (I_{1355}/ I_{1580} in their notation) on irradiation, which was obtained based on an accumulation of

experimental data with Raman and high-resolution transmission electron microscopy (HRTEM).[72,74] The picture shows the domains of the formation of in-plane defects in the first stage (small FWHM and R), turbulence and disordering of the basal plane in the middle stage (large FWHM and small R), and the amorphization in the final (large FWHM and R). They suggested the first stage structure may correspond to the TEM-lattice image in Figure 29c, and the middle stage structure to that in Figure 29d.[74]

Raman scattering on severe lattice disordering of graphite was also reported for neutron irradiation,[76] plasma irradiation,[71] and electron beam irradiation[77,78] along the same line as discussed here.

302

(a) Low Fluence   **(b)** Intermediate Fluence   **(c)** High Fluence
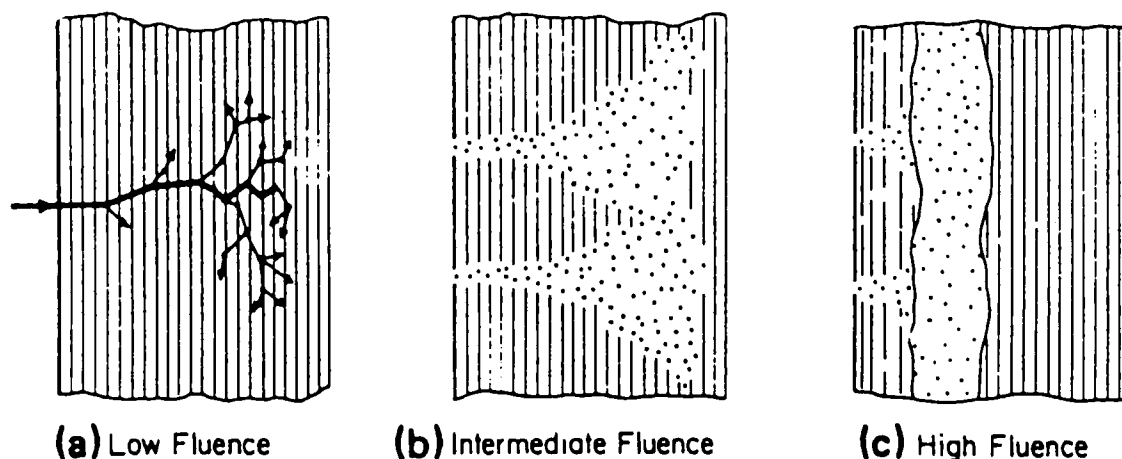
**FIGURE 23.** Schematic view of the disordered region in graphite caused by implantation at (a) low, (b) intermediate, and (c) high fluence (dose).[70]

b. SERS and Damage of Outmost Surface

Observation of disorder on the outermost surface is possible with surface-enhanced Raman scattering (SERS). SERS measurements were performed on Ag-overlayered surfaces of carbon materials such as graphite, glassy carbon, diamond and carbon fibers.[41,42] Figure 30 shows the Raman spectra from a surface of HOPG that was irradiated with 3-keV deuterium ions to a dose of 5×10^{13} ions/cm^2 after the Ag deposition. The spectrum from the unirradiated region is a sharp singlet (Figure 30a), which is essentially identical to virgin HOPG. On the other hand, the spectrum (Figure 30b) from the ion-irradiated region is markedly different from that without the Ag-overlayer. It is evident that surface roughness induced by ion irradiation yields measurable SERS of the outmost surface. The FWHM of the G and D peaks of the SERS spectrum (Figure 30b) was ≈ 240 to ≈ 360 cm^{-1}. Both G- and D-peaks are extremely broad and poorly resolved. A similar broad doublet feature was observed for high flux ion irradiation of deposited carbon films (Figure 24). The spectrum

corresponds to highly disordered carbon materials. The La was calculated from R to be ≈ 3.6 nm using Eq. 15. The value was about 1/3 of that from Raman scattering from an HOPG sample without the Ag overlayer. Because d_{opt} for 514.15 nm light used in this experiment is about 50 nm and the depth of the damage distribution is about 15 nm, the Raman without the Ag-layer is made up by the superposition of the scattering from both damaged and undamaged regions. La estimated from the Raman without the Ag-layer is then an average for both regions. It was proven with SERS that the outmost surface is highly damaged by ion irradiation. Recently, Raman scattering from microcluster silicon was detected by a kind of SERS mechanism.[154]

It is hard to observe the ion-implantation-induced disorder in diamond because it has a quite large d_{opt} (transparent). Ion implantation of diamond led to a formation of a graphite phase in the diamond matrix by a destruction of sp^3 bond to sp^2, and finally the diamond exhibited quite similar features to amorphous carbon structure.[72] Compared with graphite and diamond, to our knowledge, the Raman scattering on ion-irradiated fullerenes has not been studied.
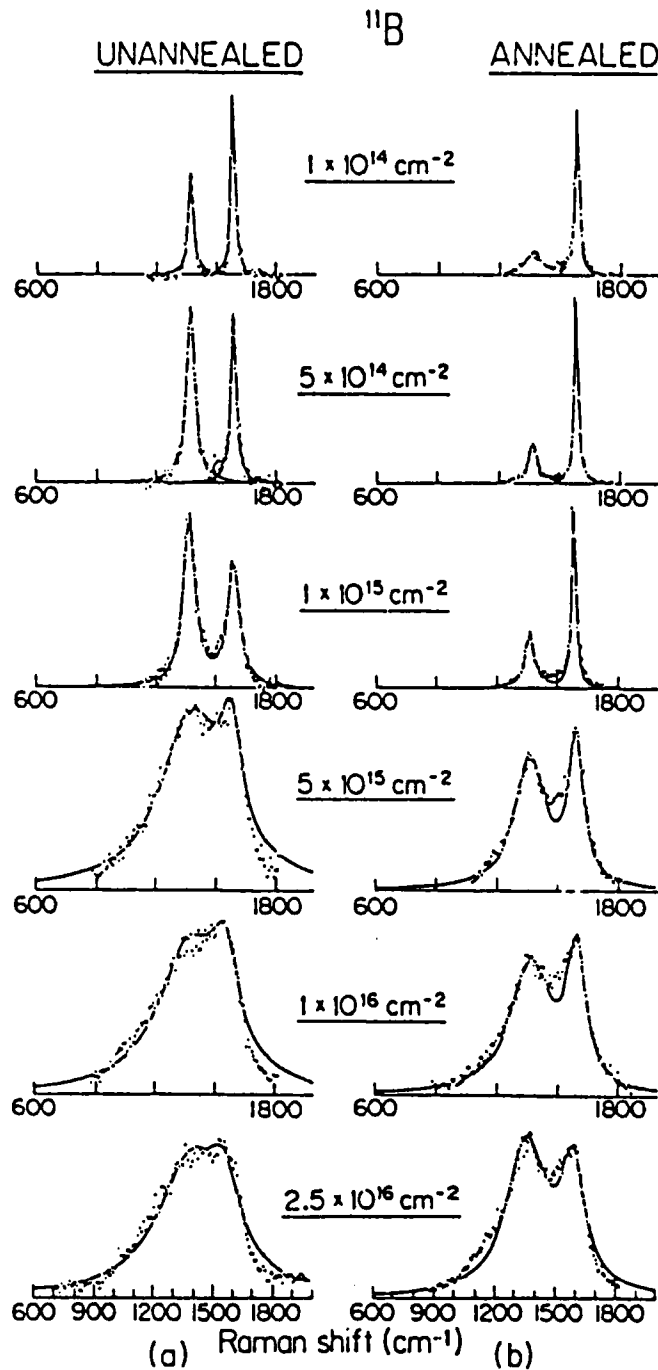
FIGURE 24. Raman spectra for various doses (1×10^{14} to 2.5×10^{16} ions/cm^2) of 100 keV ^{11}B$^+$ ions implanted into six HOPG samples. The spectra on the left (a) are for the unannealed samples, and on the right (b) are for the same samples annealed at 950°C for 0.5 h.[69] The abscissa is linear in wave number and the points are experimental.

4. Defects-Induced Stress

Defects typically strain the lattice. The lattice strain causes changes in Raman lines. That contributes typically to frequency shifts of phonon Raman line, while its relation with line broadening is experimentally not clear.[6] Huang et al.[14] discussed the strains
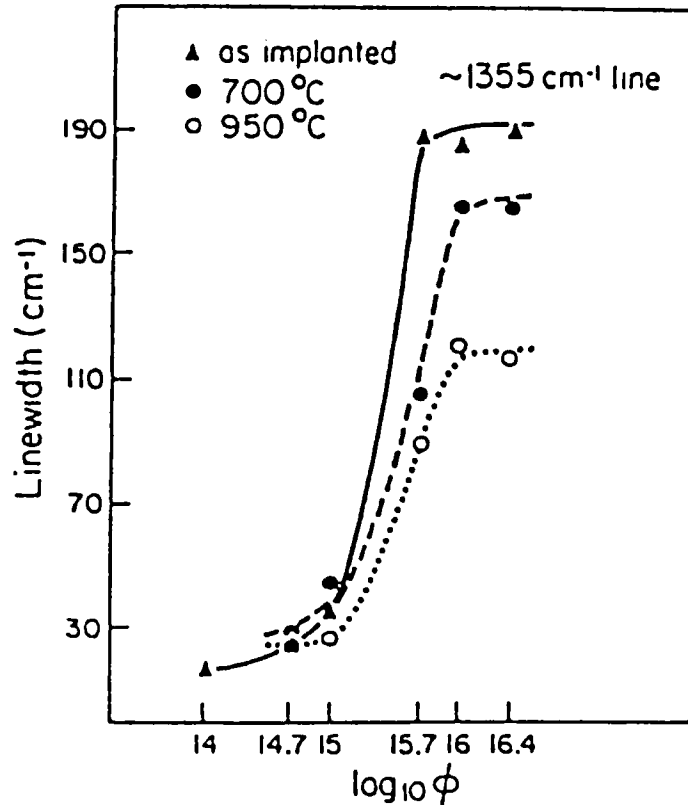
FIGURE 25. Graph of the 1360-cm^{-1} (D-peak) linewidth (FWHM) vs $\log_{10} \phi$ for[11] B^{+} ion-implanted HOPG, where ϕ is the boron dose. Results are presented for unannealed samples and for the same samples annealed at 700°C and 950°C.[69]

(and the corresponding stress) in the 1.5 MeV Si^{+} ion-implanted silicon. They took this effect into account by introducing a parameter ω_{strain}, which represents the strain-induced line shifts, and replacing the term $[\omega - \omega(q)]$ with $[\omega - \omega_{strain} - \omega(q)]$ in the SC model (Eq. 14). In other words, in their model a deviation of the phonon line frequency from the dispersion relation was referred to the strains. The shifts in the optical phonon Raman frequency of single crystals of silicon were, experimentally, known as a linear function of hydrostatic pressure, and then the magnitude of stress due to the strains was estimated from ω_{strain}. The stress was always compressive in an ion dose range of 0 to 1 × 10^{15} Si^{+}/cm^{2}. The most likely source of the stress was specu-

lated to be due to the nuclear energy deposited by the ion beam near surface layer. Probably the compressive stress is caused by an agglomeration of point defects that would lead to a local volume expansion. The stress increased monotonically with ion dose. However, it decreased following reaching a maximum at a dose of 1 × 10^{14} Si^{+}/cm^{2}. This suggested the stress relaxation through near-surface amorphization at higher doses.[14]

Kitajima and Nakamura[150] obtained a local stress in carbon materials irradiated by a high-density electron beam from a microscopic Raman measurements. The local stress was evaluated from the frequency shift of the G-peak by considering the microcrystallite size effect on the phonon
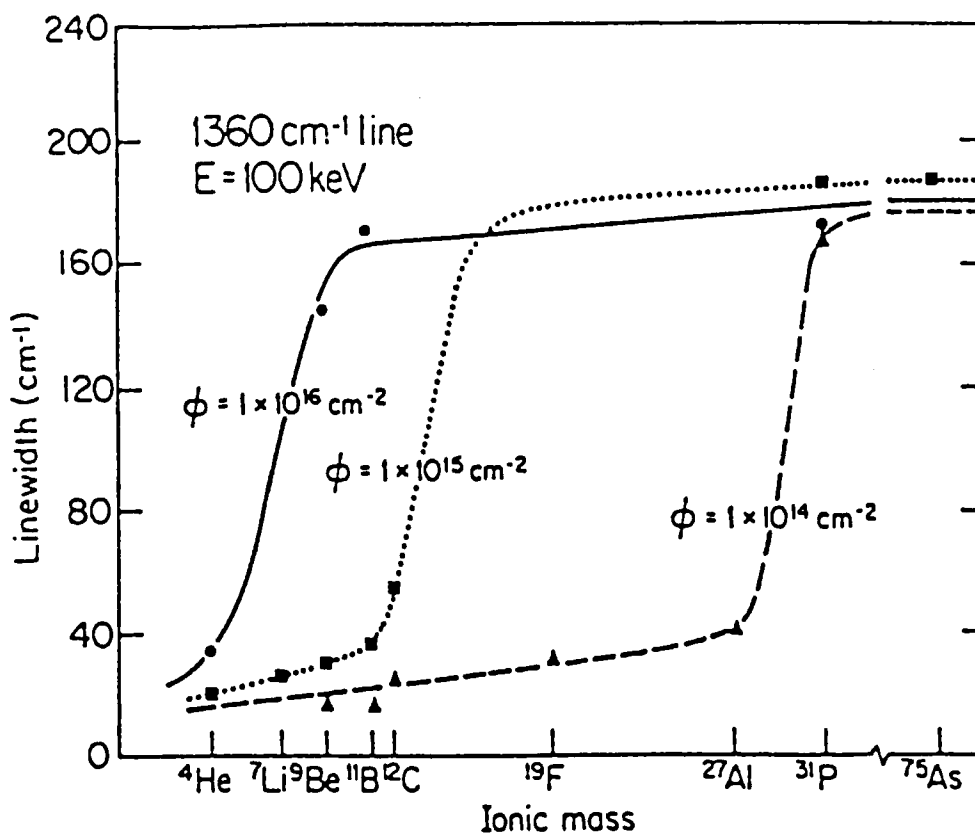
FIGURE 26. Plot of the linewidth (FWHM) of the D-peak at ~1360 cm⁻¹ vs. ionic mass for HOPG implanted with 100-keV ions at different doses.[70]

dispersion. The magnitude of the stress was also calibrated from the hydrostatic pressure dependence of the line shift.[40] Graphite was compressively stressed by electron irradiation. On the other hand, C/C composite exhibited little stress. This suggests a relaxation of the compressive stress by the existence of carbon fibers in the C/C composite.

Concerning the defects-induced stress, mechanical polishing is known to induce surface strain.[6,149] Polished surfaces of (100)-GaAs and InP by alumina powders exhibited upshifts (by 9 to 13 cm⁻¹) of the LO optic phonon lines, which correspond to the compressive surface strains of about 4% for GaAs and 5% for InP.[149]

The influences of lattice strains on vibrational spectra have not been well studied (although this is a personal feeling). Systematic Raman (and also infrared) investigations, which would be combined with theoretical calculations on bonding stress based on, for example, *ab initio* molecular orbital theory or density functional theory, are of great interest for the quantitative understanding.

V. KINETIC STUDY ON LATTICE DISORDERING

In the following two sections, we discuss kinetic studies on disordering and its

FIGURE 27. Ratio of intensities of the D-peak at ~1360 cm⁻¹ to the G-peak at ~1580 cm⁻¹ line (R) vs. ionic mass for implantation at 100 keV for two doses.[70]

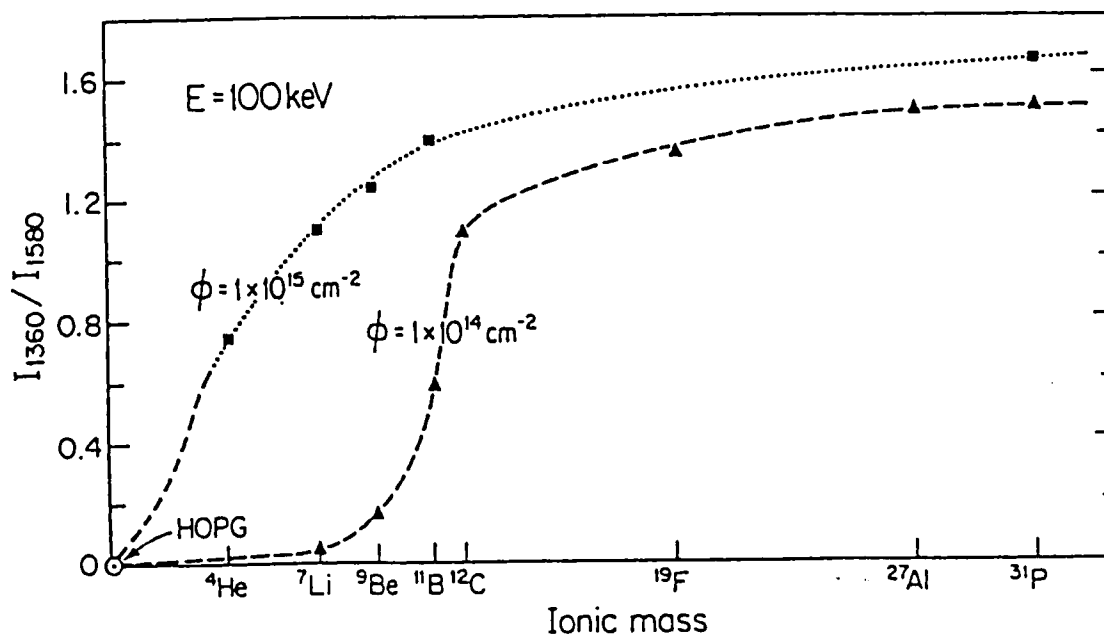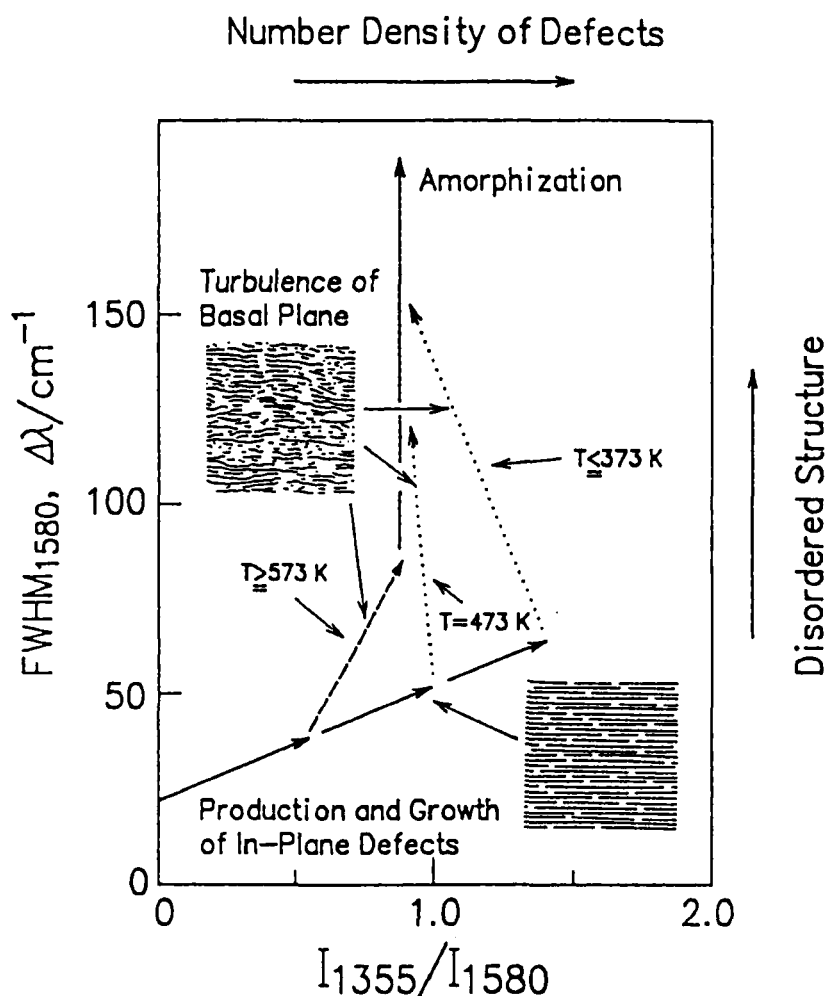relaxation in ion-irradiated crystals. Despite a large number of Raman studies on crystals irradiated with energetic ions for characterizing microscopic structural properties (Section IV), the lattice disordering kinetics in the early stage of irradiation was not well understood. To study rapid phenomena in the early stage irradiation on a time scale of seconds, real-time measurements are required; however, ion irradiation and Raman measurements had been performed separately, until the experimental system of the real-time Raman measurements were developed by the author and the co-workers.[79-84] In this section we first explain the kinetic studies on lattice disorder induced by ion irradiation in graphite and semiconductors, using the real-time system. Attention is focused on the initial change in the Raman spectrum caused by ion irradiation.

A. Experimental Setup

Figure 31 shows a schematic drawing of the experimental setup for the real-time Raman measurements during ion irradiation.[79,82] The ion irradiation was performed in an ultrahigh vacuum chamber (base pressure < 10⁻⁸ Pa). The incident angle of the ion beam was 55 degrees normal to the c face. Incident radiation of 514.5 nm was provided using a cw Argon-ion laser. The scattered radiation was collected through the sapphire window of the chamber in backscattering configuration, analyzed by a double-grating monochromater, and detected by a spectrometric multichannel analyzer. The minimum exposure time of the detector was 33 ms, and the exposure time used for the experiment was 180 times the minimum exposure time (about 6 s) to get intense signals.[79,80] Because of the existence

Number Density of Defects →

(Figure axes: FWHM$_{1580}$, $\Delta\lambda/cm^{-1}$ — 0, 50, 100, 150; Disordered Structure; Amorphization; Turbulence of Basal Plane; T≤373 K; T≥573 K; T=473 K; Production and Growth of In–Plane Defects; horizontal axis I_{1355}/I_{1580} — 0, 1.0, 2.0)

FIGURE 28. Schematic drawing of the change in peak width of ~1580 cm^{-1} and intensity ratio of I_{1355}/I_{1580} (R) on irradiation. Schematic pictures of graphite layers considered from the Raman and HRTEM results are shown in the figure. The solid line, long- broken and short-broken lines can, respectively, be assigned to the formation of in-plane defects in the first stage, the turbulence and disordering of the basal plane in the middle stage, and the amorphization in the final stage.[72,74]

of the DIRS peak, the Raman scattering in graphite is much more sensitive to lattice disorder than those in semiconductors. The real-time Raman measurements were first applied to the disordering of graphite.

B. Graphite

1. Real-Time Observation of Raman Spectra during Ion Irradiation

Cascade process caused by ion irradiation produces a disorder region around an ion trajectory. In crystalline graphite, the Raman spectrum exhibits a double-peaked spectrum. The relative intensity between two peaks varies as a degree of disorder (Sections III.B, IV.A.2, and IV.B.3). At a sufficiently high dosage, an amorphous layer is formed and the Raman spectrum exhibits a broad asymmetric line at around 1500 cm^{-1}. As studies[69-72,74] of Raman scattering from ion-implanted graphite have shown, the rapid reduction in crystallite size was supposed in the early stage and the abrupt transformation to an amorphous structure occurred
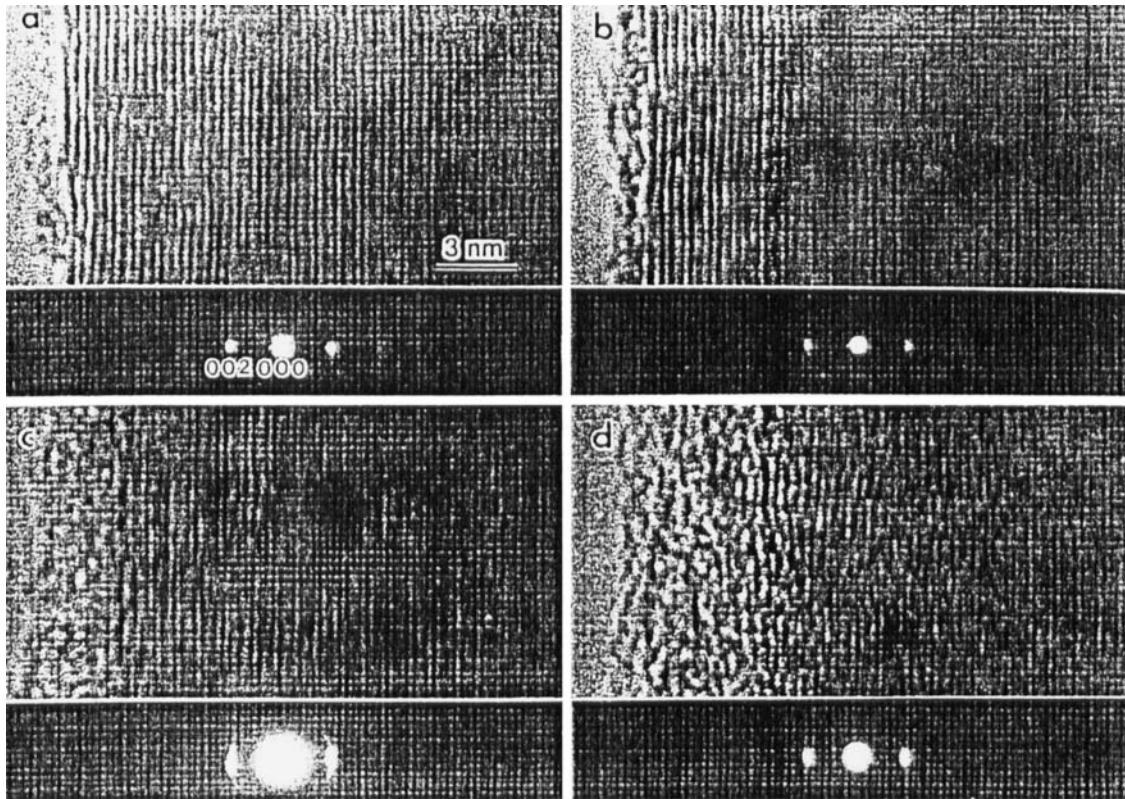
FIGURE 29. Lattice images and diffraction patterns in high-resolution TEM for carbon fibers (a) unirradiated and irradiated with (b) 3.6×10^{18} m^2, (c) 1.4×10^{23} m^2, and (d) 1.9×10^{24} m^2.[74]

under ion irradiation (Section IV.B.3). Therefore, it is of importance to perform real-time Raman measurements of graphite during ion irradiation.[79]

Figure 32 shows the first observation of real-time change of first-order Raman spectrum of HOPG before and during 3 keV Ar$^+$ ion irradiation at room temperature. Only a sigle crystal peak was observed at ~1580 cm^{-1} (G) before irradiation (Figure 32a). Ion irradiation induced a peak at ~1360 cm^{-1} (D) as shown in Figures 32b thru e, which were measured during ion irradiation at 18, 48, 78, and 108 s after the beginning of irradiation at a flux of 2.5×10^{11} Ar/cm^2 s.[79,81] The peak height of the D-peak increased and that of the G peak decreased with an increase in the irradiation time. The line width of both D and G peaks, on the

other hand, increased with irradiation (Figure 33). A drastic change in width and intensity and a broad asymmetric Raman line centered at about 1500 cm^{-1}, characteristic of the amorphous regime, were not observed. The peak intensity ratio R is plotted as a function of irradiation time in Figure 34. We see an abrupt increase in R after the irradiation start. The increase in the D-peak was slower for ion irradiation at lower flux (3.3×10^{10} Ar/cm^2 s) than that for irradiation at a flux of 2.5×10^{11} Ar/cm^2 s (Figure 35a).

The optical skin depth of 514.5 nm light in graphite is usually larger than an ion trajectory of ion irradiation with ion energy of keV order. For example, the ion ranges of 3 keV He$^+$ and 3 keV Ar$^+$ in graphite are 19 nm and 3 nm.[80] The optical penetration depth of 514.5 nm is about 40 nm. There-
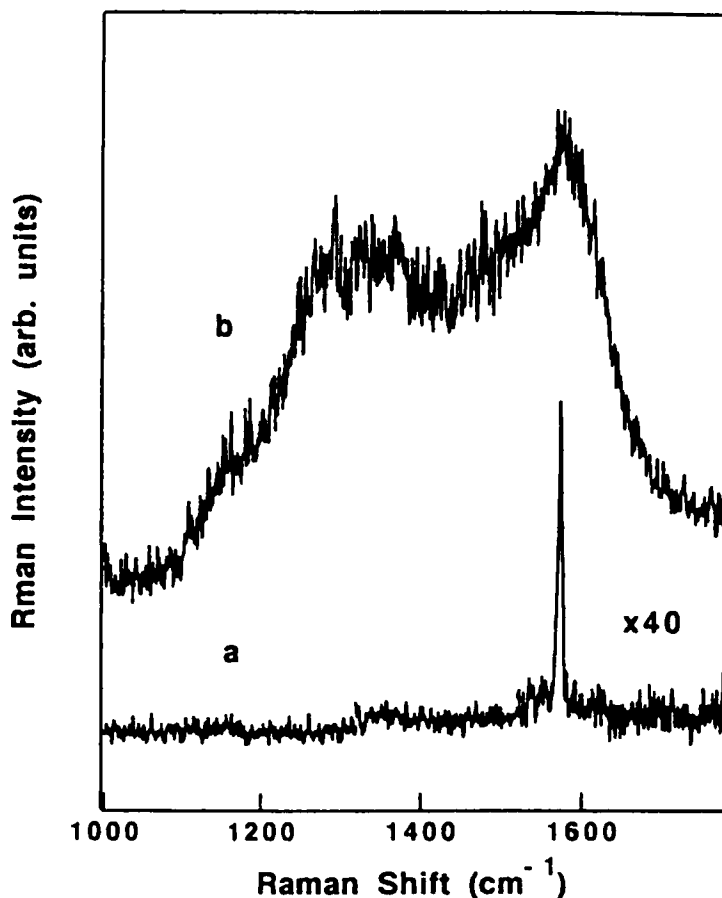
FIGURE 30. Raman spectra of HOPG after 480 s deuteron irradiation after evaporation of an Ag film: (a) unirradiated region, and (b) irradiated region with 3 keV deuteron.[42]

fore, the observed Raman spectrum is made up of the superposition of scattering from both damaged and non-damaged layers. It is then important to estimate contributions from damaged layers to study the actual ion irradiation effects. Damaged profiles due to ion irradiation are not uniform (Figures 11 and 12) and can be well approximated by a Gaussian function. The relation between the mean value of the peak intensity ratio of the D-peak with respect to the G-peak in the damaged region, R_0, and the observed intensity ratio, R_{obs}, is given by[81]

$$R_{obs} = \frac{R_0 P \lambda}{8 \pi m} \int_0^\infty F(x) \exp(-8\pi mx/\lambda) dx \quad (16)$$

where P is the whole range of energy deposition, m is the optical parameter (0.9 for carbon material), λ is the wave length of exciting light, x is the depth, and $F(x)$ is the normalized depth profile of the damaged layer. R_{obs} is corrected to the mean actual relative peak intensity ratio R_0. Comparing R_{obs} (Figure 34) and R_0 (Figure 35), the calculated peak intensity ratio of the damaged area is much larger than the experimentally observed one.

Figure 36 is the time dependence of R_0 for irradiation of 3 keV He[+]. R_0 is proportional to the square root of the irradiation time[82-84] for a short time of irradiation. Similar behavior was observed
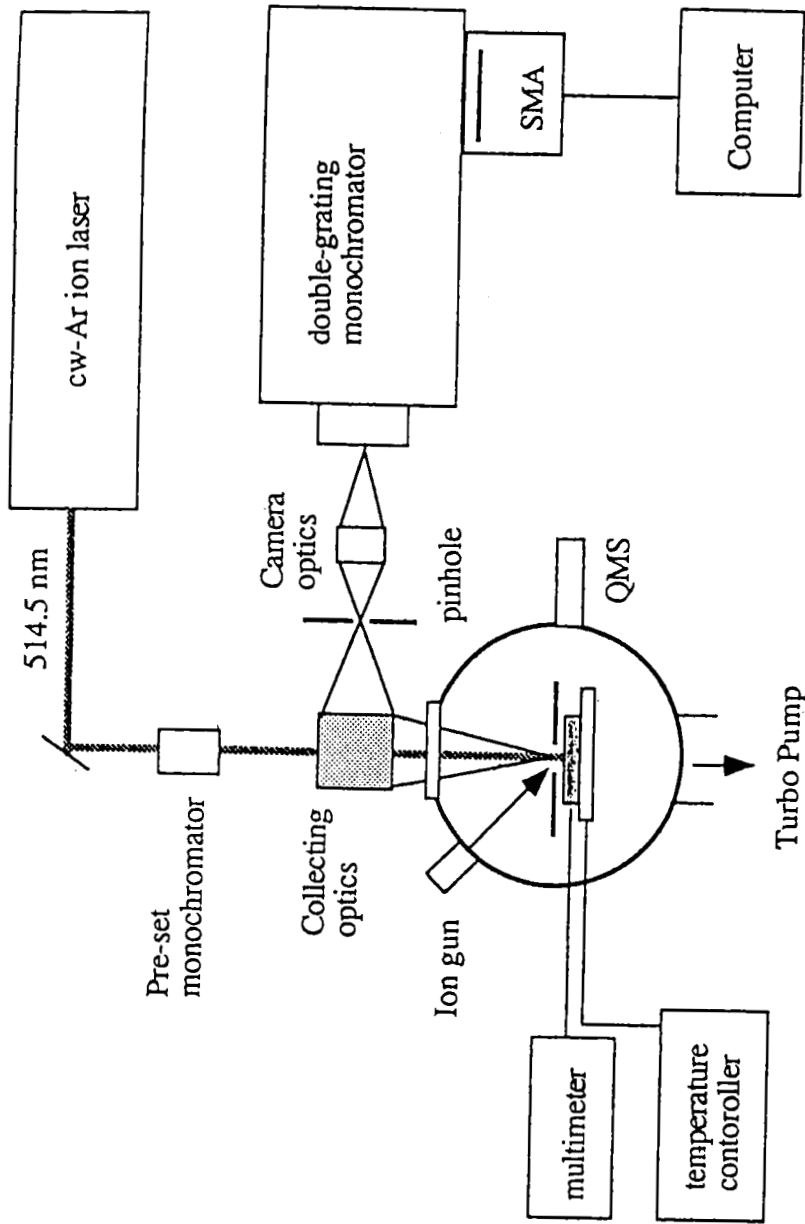
FIGURE 31. Schematic drawing of experimental set up. SMA: spectrometric multichannel analyzer.[82]
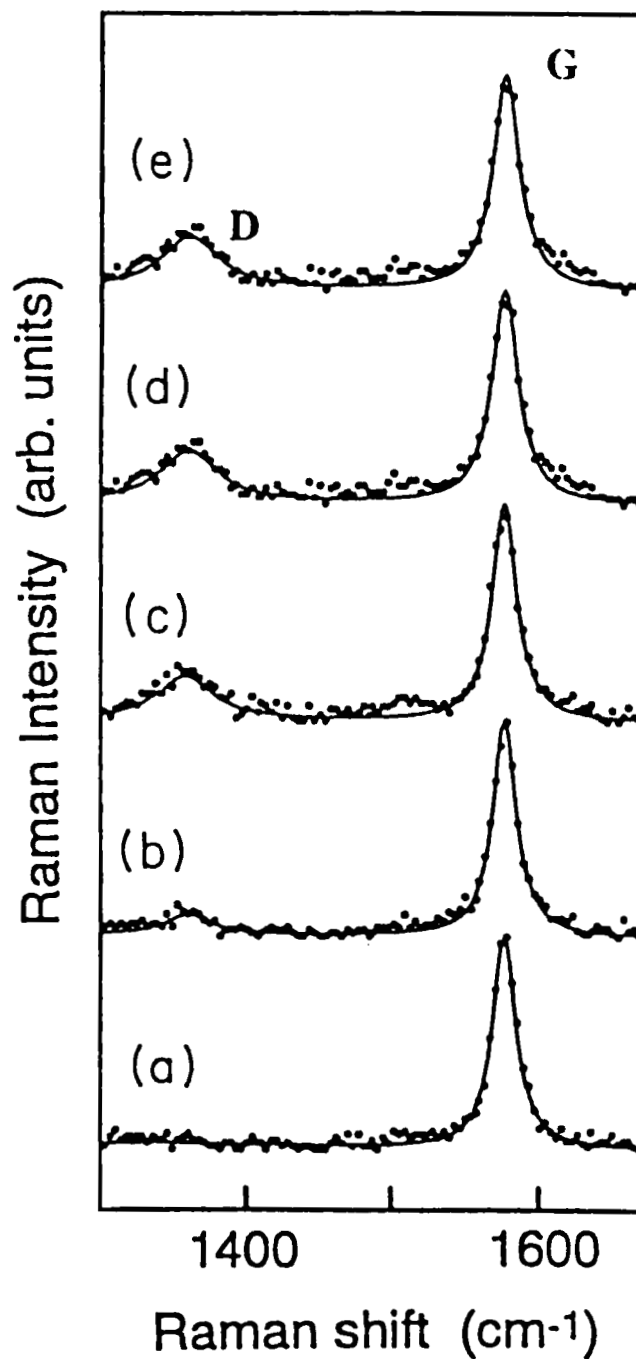
FIGURE 32. Raman spectra of highly oriented pyrolytic graphite (HOPG) (a) before ion irradiation and obtained during the irradiation after (b) 18, (c) 48, (d) 78, and (e) 108 s from the beginning of the irradiation of 3-keV Ar$^+$ at a flux of 3×10^{11} ions/cm^2 s. Solid curves are the computer simulation results. The peak at ~1580 cm^{-1} (G) is a Raman active E_{2g} mode peak and the peak at ~1360 cm^{-1} (D) is a disorder-induced peak.[79,81]
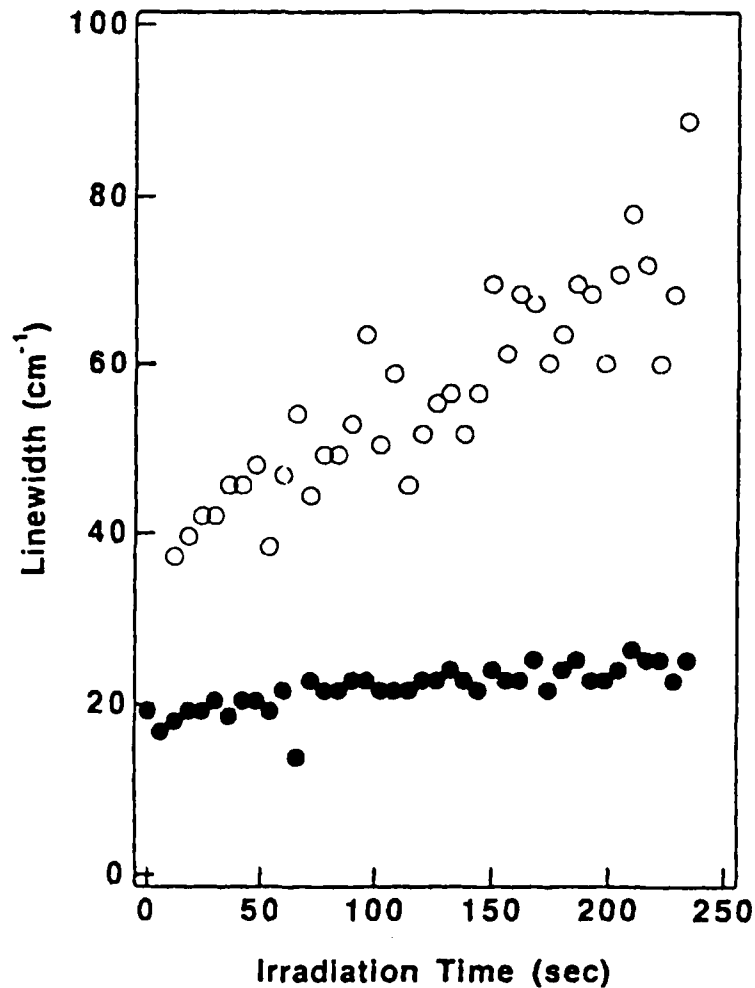
FIGURE 33. Time dependence of the linewidth of HOPG for the irradiation of 3-keV Ar* at a flux of 3 × 10¹¹ ions/cm² s, the disorder-induced line (D-peak, circle) and the Raman active line (G-peak, solid circle).[81]

for irradiation with Ar⁺, Ne⁺,[30,88] and hydrogen ions.[42]

2. Interdefect Distance (IDD) Model: Phonon Confinement Due To Single Vacancies in the Graphite Plane and Disordering Rate

The ion doses used in the real-time Raman measurements mentioned above were on the order of 10¹³ ions/cm² at most. Here we discuss a model of disordering where the basal plane structure is main-

tained and only very local defects exist in the plane, that is, to be a structure like a model (a) of Figure 23 or a lattice image between (a) and (b) in Figure 29. In general, the mean number of defects per layer (N_L) induced by ion irradiation is given by

$$N_L = Nf\sigma v \varphi t \qquad (17)$$

where N is the density of the target (1.25 × 10²³ atoms/cm³), σ is the displacement cross section, φ is the incident ion flux, v is the mean number of displaced atoms in the cascade per primary knock-on, f is the dis-

313

FIGURE 34. Time dependence of the relative intensity ratio (R) of the D-peak with respect to the G-peak of HOPG for the irradiation of 3-keV Ar+ at a flux of 3 × 10^{11} ions/cm^2 s.[79,81]

tance between graphite layers (0.335 nm), and t is the irradiation time. The mean distance (ℓ_d) between in-plane defects can be given by

$$\ell_d = N_L^{-1/2} = (Nf\sigma v\varphi)^{-1/2} \quad (18)$$

Assuming that ℓ_d corresponds to the in-plane phonon correlation length La because the defects should cut or change the interaction between lattice atoms, the mean relative intensity ratio of the Raman peaks within the ion penetration depth is expressed using Eq. 15 as

$$R = C(N\sigma\varphi vt)^{1/2} = \alpha(\varphi t)^{1/2} \quad (19)$$

Eq. 19 explains the square root dependence of the irradiation time to R, which was observed by the real-time measurements (Figure 36). The displacement cross-section σ and the total displaced atoms v can be calculated by the Sigmund theory[85] and a simplified model of the Kinchin-Pease theory,[86] respectively, α is the disordering rate constant and a quantity that depends on incident ion energy and ion mass through σ and v. An experimental value α_{obs} of the disordering rate constant is also estimated from the gradient of R_0 to ion dose.

The relative intensity (R) by calculated Eq. 19 is shown in Figure 35 and agrees well with experimental data for both Ar+

314
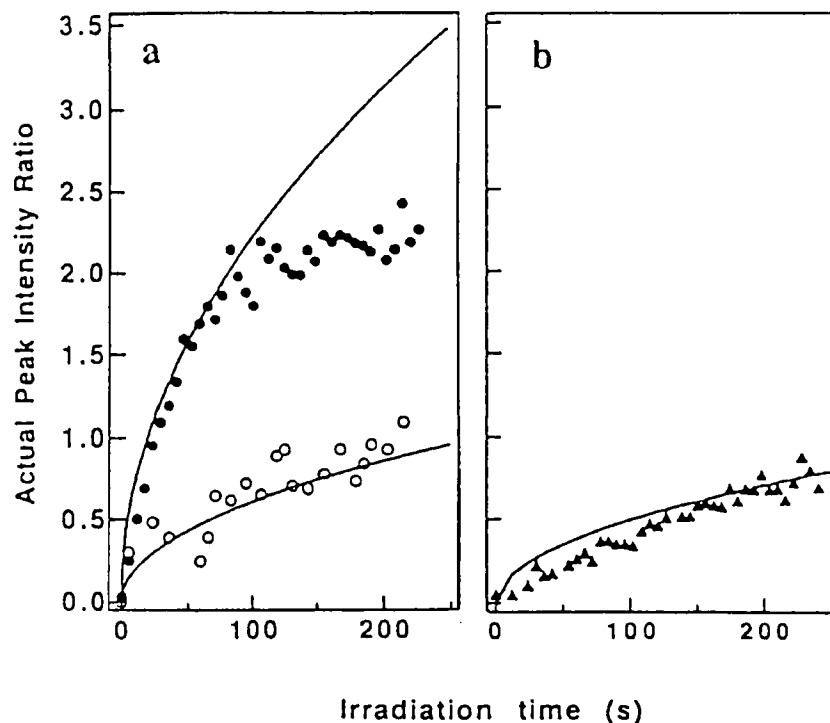
FIGURE 35. Time dependence of the actual relative intensity R_0 of HOPG for (a) 3-keV Ar^+ at a flux of 2.5 × 10^{11} ions/cm^2 s (solid circle) and 3.3 × 10^{10} ions/cm^2 s (circle), and (b) 3-keV He^+ at a flux of 2.0 × 10^{11} ions/cm^2 s (solid triangle). Solid curves are the results of calculation with the IDD model.[80,81]

and He^+ irradiation. It is evident that the theory explains the ion flux effect on the time dependence (Figure 35a). We can speculate on the deviation from theory at longer times. Creation of the defect clusters was suggested to be one of the reasons for the deviation between calculation and experiments. If defects aggregate and create clusters, the effective distance between defects or clusters should increase.[81]

The effect of ion energy on the disordering rate is not large for ion energies in the keV range, because the (v × σ) does not change much when the ion energy changes. Actually, the disordering rate constant obtained experimentally under He^+ irradiation was almost the same for all ion energies of (0.5 to 5 keV).[87]

A systematic study on the effect of incident ion mass on the disordering rate e was performed.[30,101] The observed R for Ne^+, Kr^+, and Xe^+ ions was confirmed to also increase proportionally to the square root of irradiation time. Figure 37 shows a comparison of α_{calc} and α_{obs} plotted vs. ion mass. In the low-mass region, experimental values of the lattice disordering rate increases steeply as the ion mass increases, slowly reaching a saturation value in the high-mass region. The calculation reproduced this tendency and the values are consistent with experimental values. All parameters used for the calculation and experimentally obtained values are listed Table 1. It was evident that the ion mass effect on the disordering rate is well explained by the interdefect distance (IDD) model calculation.

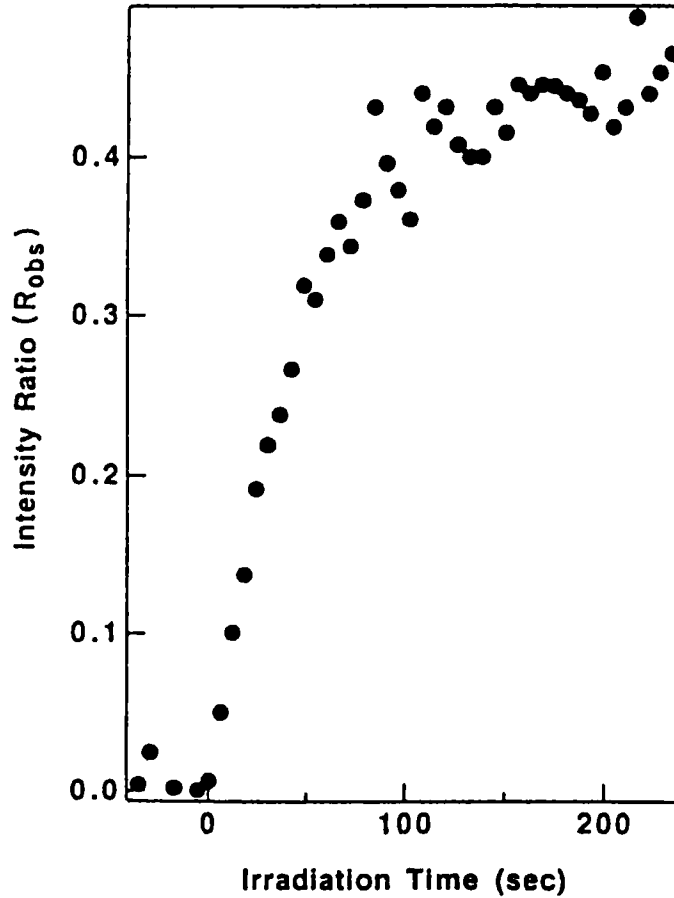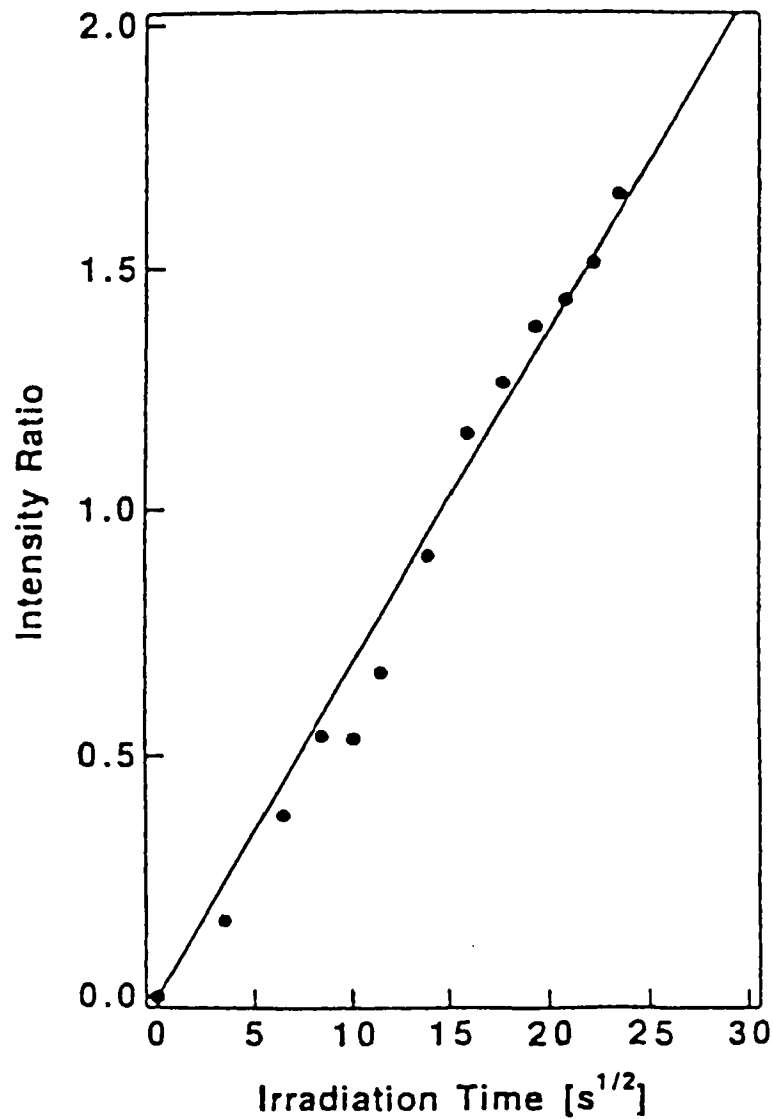**FIGURE 36.** Time dependence of the peak intensity ratio of the D-peak with respect to the G-peak (R) of HOPG for irradiation of 3-keV He+. Solid line is the least square fitting.[82]

The simplified calculation based on the IDD model suggests that the in-plane phonon correlation length is in agreement with the mean distance between defects in the graphite plane at the lower dose range. This is reasonable because defects or vacancies induced by the ion-irradiation have to terminate the phonon propagation in the graphite plane.

C. Semiconductors

1. The IDD Model and Three-Dimensional Crystals

Disorder induces a DIRS peak near 1360 cm^{-1} (D-peak) in graphite that is very sensitive to the disordering. However, in semiconductors such a sensitive
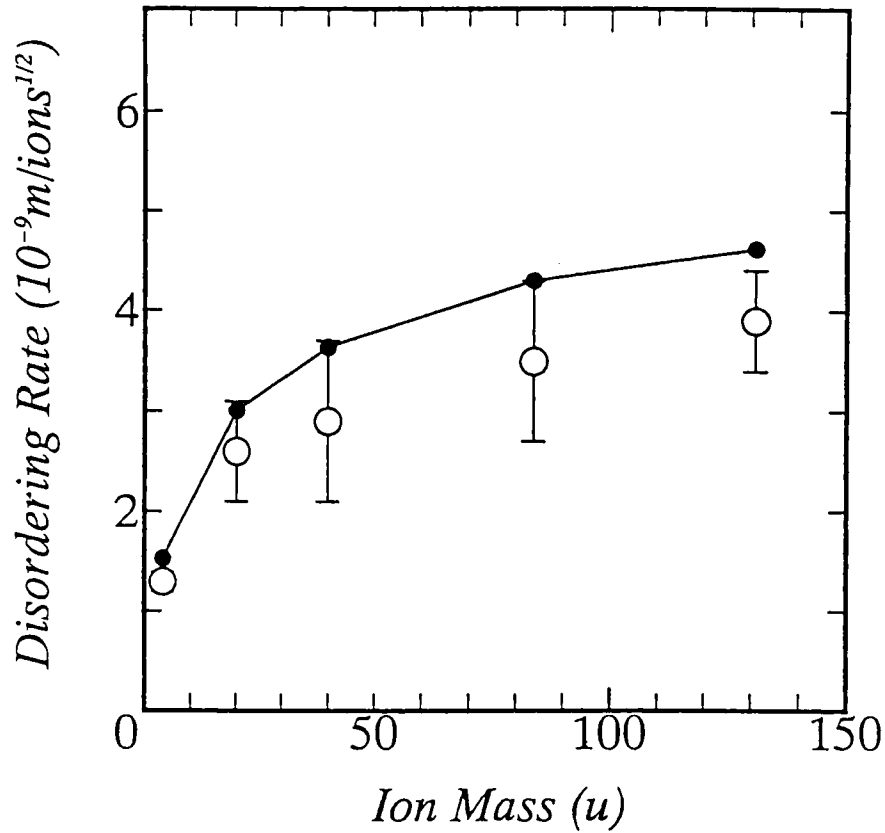
FIGURE 37. Ion mass number dependence of disordering rate of HOPG: (circle) experimental value, calculated (solid circle) value by Eq. 19.[30]

TABLE 1
Calculated Displacement Cross-Section σ, Damage Function ν, and the Disordering Rate Constant α in Graphite

Ion	ν	σ (10^{-21} m²)	α_{obs} (10^{-9} m/ions^{1/2})	α_{calc} (10^{-9} m/ions^{1/2})
He⁺	2.32	1.25	1.3 ± 0.1	1.53
Ne⁺	2.43	4.59	2.6 ± 0.3	3.01
Ar⁺	2.29	7.12	2.9 ± 0.8	3.64
Kr⁺	2.05	11.1	3.8 ± 0.5	4.30
Xe⁺	1.87	14.1	4.1 ± 0.6	4.62

Note: α_{exp} and α_{calc} are experimental values of the disordering rate and calculated value by the IDD model, respectively.[30]

DIRS peak does not exist. Therefore, we obtain the phonon correlation length L from the changes in linewidth and frequency. In this section the time dependence (ion dose dependence) of L is compared with that of graphite, and kinetics of the damage formation by ion irradiation is discussed.

Figure 38 shows first-order Raman spectra of the (100) surface of the GaAs crystal before and during 5-keV He⁺ion irradiation measured with Raman excitation of 488.0 nm. The optical penetration depth is comparable with the projectile range for the ion irradiation (see Figure 12). The damaged region near surface accounts for the majority of the measured Raman spectra. The spectra measured with 514.5 nm and 472.7 nm lights also appeared very similar to Figure 38(a). A peak at 292 cm^{-1} is assigned as the LO phonon peak, and its line shape was used as a criterion of crystallization. Figures 38b to d show that the spectral profile of the LO phonon is changed with ion irradiation: the peak shifts toward lower frequency, the width increases asymmetrically, and the intensity decreases.[59]
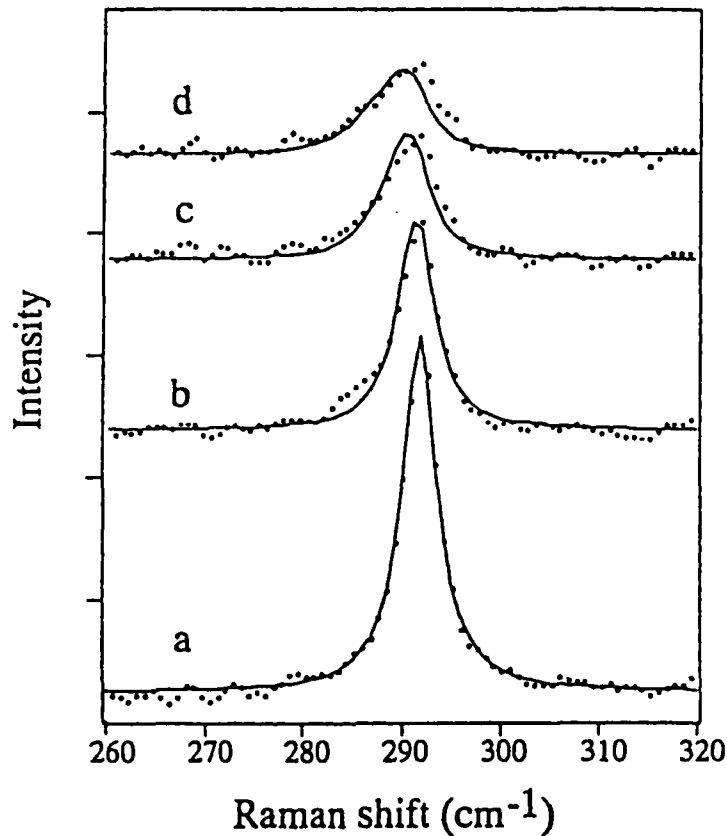
The solid lines in Figure 38 represent the fitting curve calculated using the SC model (Eq. 14) to obtain the optimum L value for each spectrum. The L values are plotted in Figure 39 as a function of ion dose $(=\varphi t)$. L is very large for the unirradiated crystal and decreases as ion dose increases for each wavelength of incident light.[59,89]

The IDD model was originally proposed to explain the disordering kinetics in graphite as a two-dimensional crystal. In the model the in-plane phonon correlation length L_a is assumed to correspond to the mean distance between vacancies in a graphite plane, ℓ_d, because the propagation of the E_{2g} phonon

FIGURE 38. Typical first-order Raman spectra of the (100) surface of the GaAs crystal with incident light of 488.0 nm: (a) before irradiation, (b) after 5.6 × 10^{19} m^{-2}, (c) after 1.4 × 10^{20} m^{-2}, and (d) after 3.4 × 10^{20} m^{-2} of 5-keV He⁺ irradiation. The solid lines represent the fitting curve calculated after Eq. 20.[59]
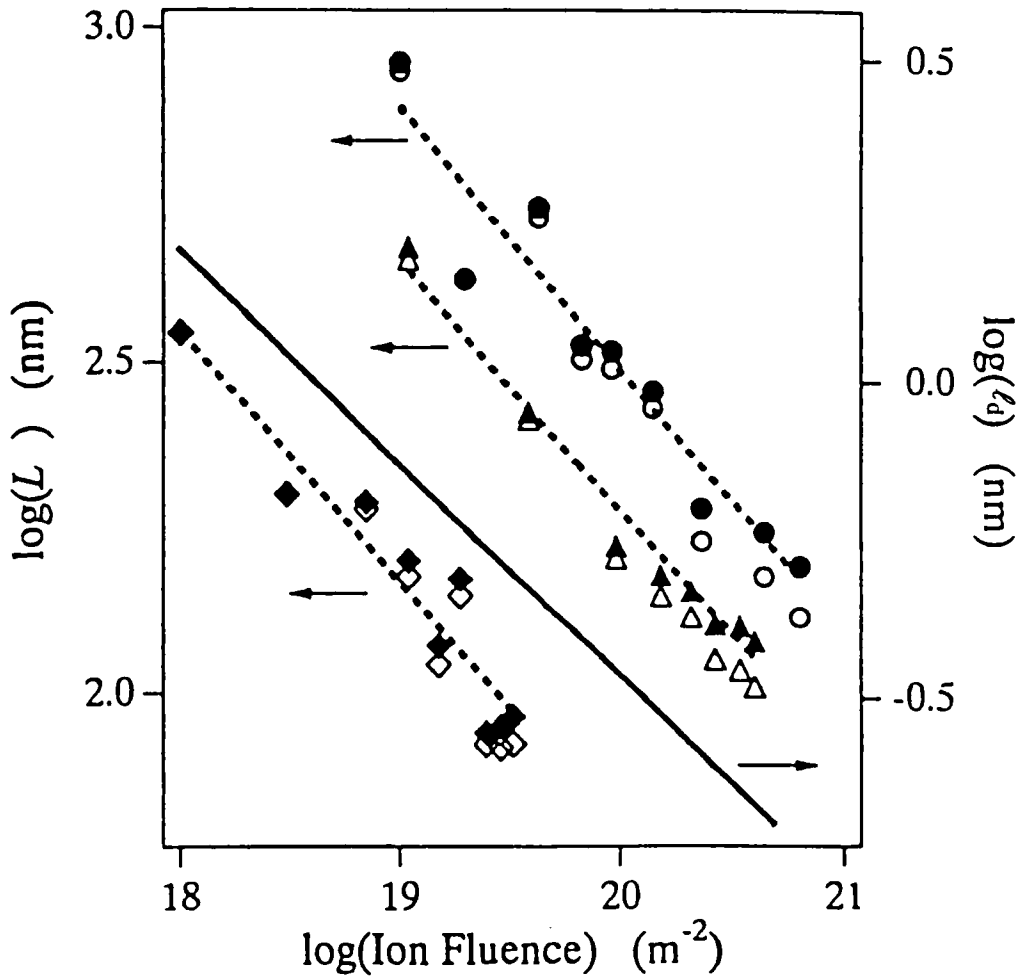
FIGURE 39. L of GaAs during 5-keV He⁺ irradiation as a function of ion fluence (dose) estimated from the curve fitting to the Raman spectra measured with incident light of 514.5 nm (circle), 488.0 nm (triangle), and 472.7 nm (square), respectively. The filled symbols represent the values of L after Eq. 14 for each wavelength. The broken lines are the least-squares fitting to the corrected values. The solid line represents ℓ_d calculated after Eq. 20.[59,89]

is restricted in the plane (Eq. 18). Let us redraw Figure 36 with the in-plane phonon correlation length La for R. The solid line in Figure 40 represents ℓ_d calculated after Eq. 18. There is good agreement between La and ℓ_d, which directly supports the correspondence of L_a to ℓ_d in ion-irradiated graphite. Here we extend the IDD model to three-dimensional crystals such as GaAs. The decrease in L with increasing ion dose (Figure 39) suggests that the localization of phonons occurs in GaAs under ion irradia-

tion as well as in graphite. Correspondence is also expected for GaAs between L and the mean distance between defects, ℓ_d, in the damaged region. Because the propagation of the LO phonon in GaAs is three dimensional, ℓ_d is expressed by

$$\ell_d = N_L^{-1/3} = \left(N\sigma\nu\varphi t\right)^{-1/3} \quad (20)$$

The actual slopes of the least-square-fitting lines to log(L) vs. log(Ion Dose) plot (broken lines in Figure 39) were –0.385 ±
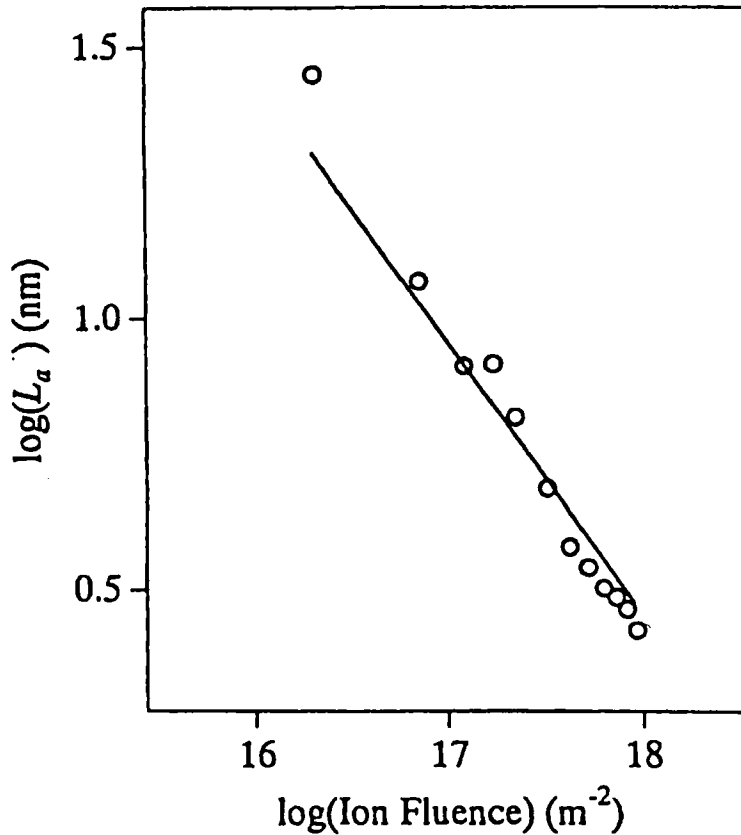
FIGURE 40. L_a of graphite under 3 keV He$^+$ irradiation, estimated from Eq. 15. La decreases inversely proportional to the square root of ion dose (fluenec). The solid line represents ℓ_d calculated after Eq. 18.[89]

0.044, -0.369 ± 0.015, and -0.322 ± 0.045 for Raman excitation of 514.5 nm, 488.0 nm, and 472.7 nm, respectively,[59,89] which are close to that expected from the IDD model, -1/3. The agreement of ion-dose dependence of L and ℓ_d implies the linear correspondence of ℓ_d to L in GaAs, showing that the IDD model is applicable to the three-dimensional crystals as well as two dimensional (Figure 41). In other words, the LO phonon becomes localized in a small volume surrounded with defects as the ion dose increases.

The phonon localization due to defect formation was confirmed also in Ge under ion irradiation, as shown in Figure 42. L in Ge (obtained using the SC model) is seen to decrease monotonically with increasing ion dose during 5-keV He$^+$ ion irradiation.[91]

The calculated value of ℓ_d for GaAs by Eq. (20) is shown in Figure 39 using the right-hand axis. It is noted that L obtained from the spectral fitting, which is plotted in the same figure using the left-hand axis, is larger than ℓ_d by more than one order of magnitude. Transmission electron microscopy (TEM) of a 1-MeV Si$^+$-implanted GaAs sample revealed no clear correlation between L and ℓ_d.[16] A similar disagreement between L and ℓ_d greater than one order of magnitude was observed for 1.5 MeV Si$^+$-ion implanted GaAs[14] and 5-keV He$^+$-irradiated Ge.[91] The discrepancy could be accounted for by three main factors: first the complete termination of the phonon propagation requires a series of dampening by defects in the three-dimensional crystal such as GaAs,[16,89] second, as point defects form
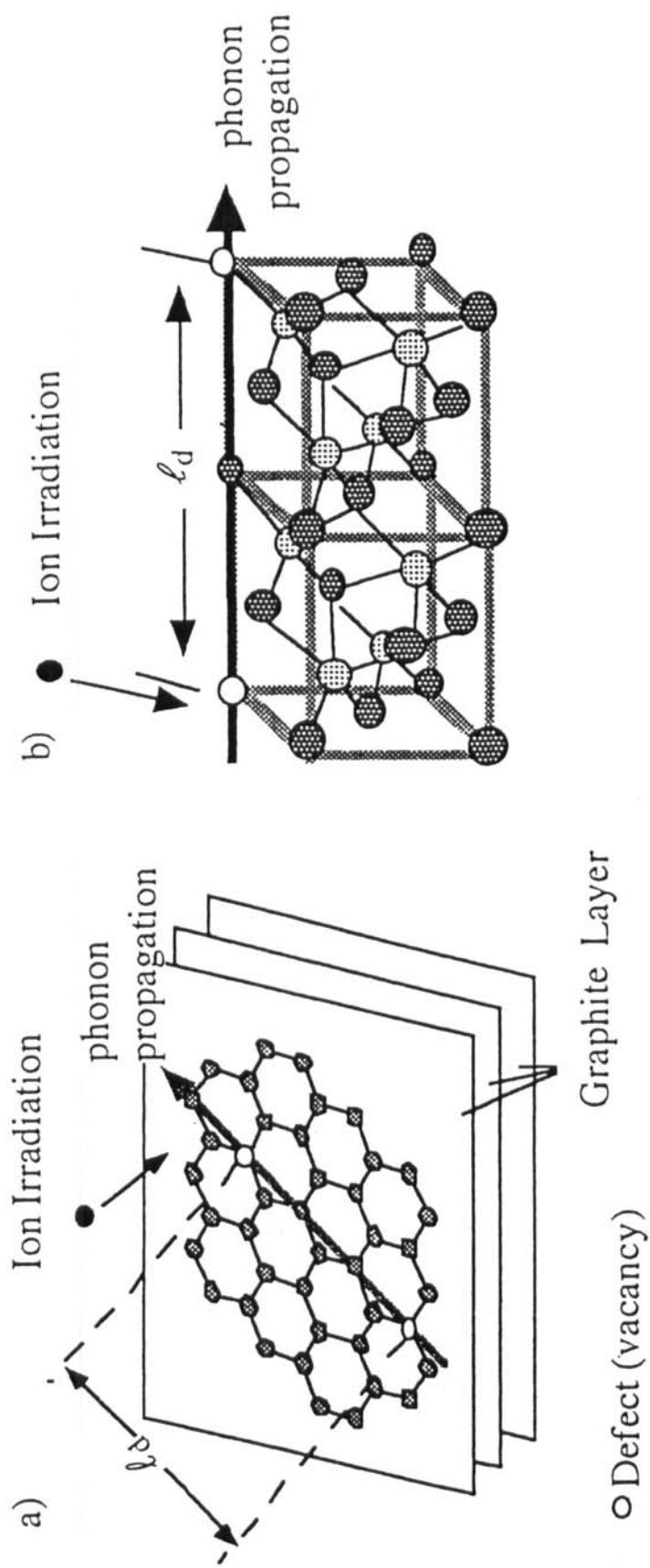
FIGURE 41. Defects and phonon propagation: interdefect distance IDD model, (a) graphite, (b) GaAs.[90]
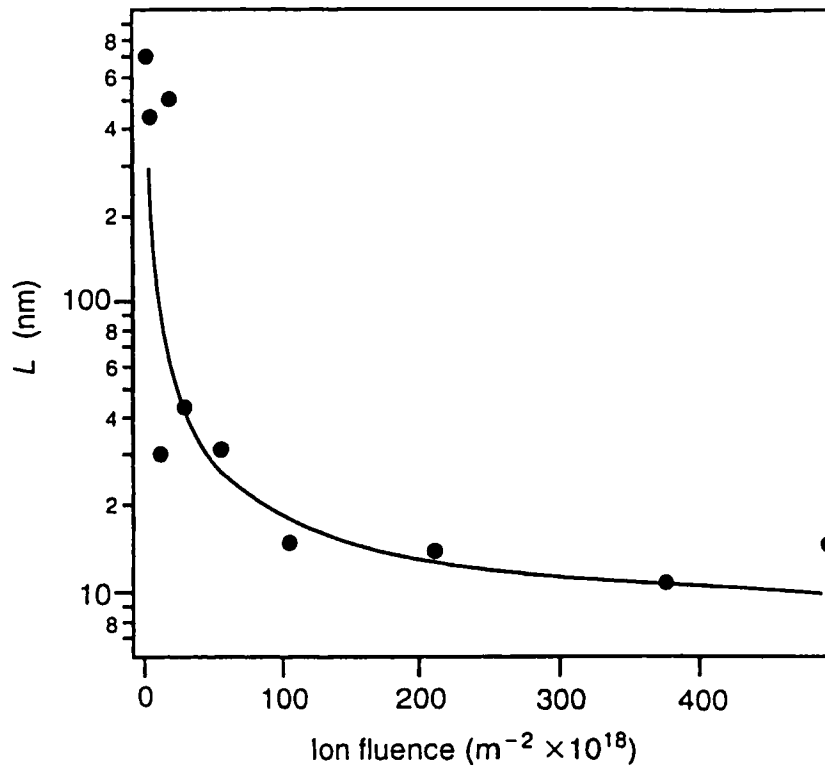
FIGURE 42. Phonon correlation length, L, of the (100) surface of Ge crystal under irradiation of 5 keV He[+], as a function of ion dose (fluence). The solid curve is a guide for the eye.[91]

aggregates (clustering),[14,89] the concentration of such aggregates or clusters is expected to be much less than the point defect concentration, and third point defects disappear during ion and laser irradiation at room temperature.[16,89]

2. Reduction in the Raman Intensity Due To Defect Formation

It is possible to discuss the disordering kinetics with respect to the reduction in Raman intensity. No change in the line width and frequency shift is expected to be observed under ion irradiation when the projectile ion range is much less than the optical penetration depth d_{opt} of Raman scattering. For example, d_{opt} of 457.9 nm light is about 500 nm for crystalline Si and 100 nm amorphous Si,[61,92] and the projectile ranges are 6.0, 7.6,

and 45 nm for 5 keV Kr[+], Ar^{+}, and He^{+} ion irradiation, respectively. In the crystals, the observed Raman scattering should be mainly from the non-damaged crystalline substrate. Actually, little change was observed in the Raman line shape of the optical phonon peak of Si at 521 cm^{-1} during 5 keV Kr[+], Ar^{+}, and He^{+} ion irradiation.[93] Only the intensities were seen to decrease. The integrated intensity of the phonon line is plotted vs. ion dose in Figure 43(a). The reduction rate of the intensity is larger for heavier ion irradiation.

The reduction of the integrated intensity of the phonon line in Si was interpreted as an increase in the absorption coefficient near the surface that was damaged by ion bombardment. The absorption coefficient is about 10^4 cm^{-1} for crystalline Si, about 10^5 cm^{-1} for amorphous Si, and in between for
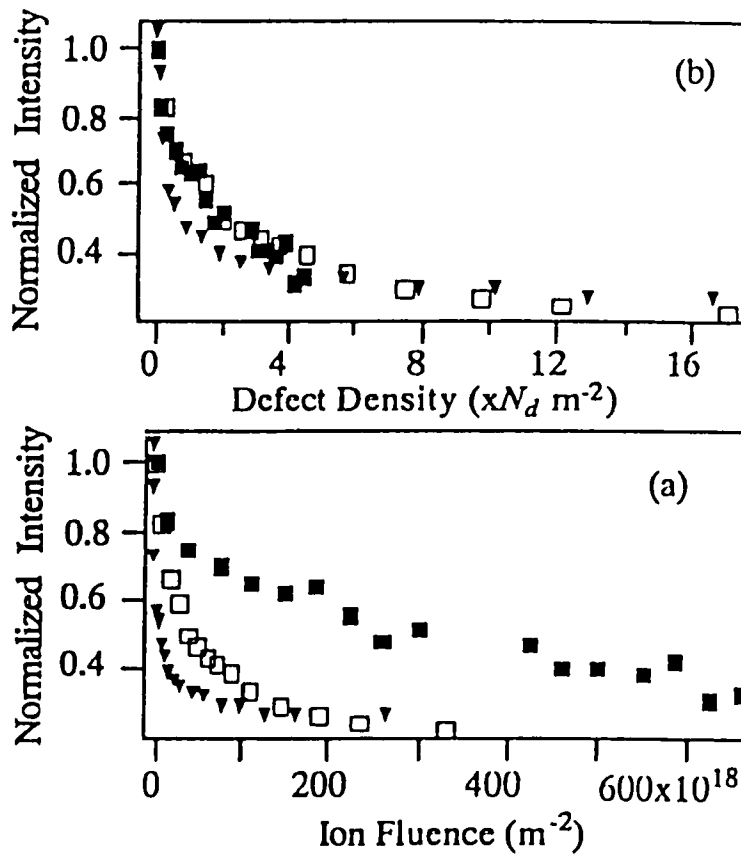
FIGURE 43. The normalized intensity of the phonon line of Si under irradiation of 5 keV He+ (solid rectangle), Ar+ (square), and Kr+ (triangle): (a) as a function of ion dose (fluence) and (b) as a function of areal density of defects (N_s) in the unit of the effective areal density of Si (N_d).[93]

the disordered medium for the wave lengths applied in the study.[61,92] The incident light and the scattered light from non-damaged Si crystal are absorbed when they go through the damaged region near the surface.[59]

There was an ion mass effect on the reduction rate of the phonon line intensity: the heavier the ion, the larger the reduction rate (Figure 43a). On the other hand, lattice disorder can be evaluated by the number of vacancies. The total number of ion-bombardment-induced defects, N_s, is given by the formula $N_s = \sigma N_d v \phi$, where N_d is the effective area density of Si, and ϕ is the ion dose (= φt). The phonon line intensity is shown as a function of N_s in Figure 43(b). No significant difference is seen among the intensity decay curves for He+, Ar+, and Kr+

irradiation. Figure 43 (b) implies that the intensity of the phonon line is dominated by the number of vacancies within the optical penetration depth. To restate, the near surface optical absorption changes through vacancy formation.

VI. KINETIC STUDY ON THERMAL RELAXATION

Because of the high sensitivity of the Raman scattering to structural changes in graphite, restoration of the disordering was well investigated.[43,44,69,74,94] In this section, Raman spectroscopy studies on annealing of ion-irradiated graphites are described briefly. We then discuss relaxation kinetics

of the lattice disorder in ion-irradiated graphite using real-time Raman measurements.

A. Thermal Annealing and Raman Spectra

Dillon et al. applied Raman spectroscopy to the study of crystallite graphite film growth,[43] and investigated annealing effects (room temperature up to 950°C) on disordered carbon films prepared by sputter and RF-discharge deposition. Their results were given in terms of R. frequency shift, and width of Raman lines as a function of annealing temperature. The R and linewidths vs. the anneal temperature indicated that substantial structural changes occur over the 400 to 600°C annealing temperature range. The decrease of R data at higher temperatures indicated a growth in crystallite dimensions. The as-deposited films changed structures from C–C bond angle disorder to threefold-coordinated crystallites, as the annealing proceeded. Shifting of the D- and G-peaks were found to be the most sensitive indications of this transformation.[43]

The lattice damage produced by ion irradiation can be relaxed and the crystal structure recovered by thermal annealing. Elman et al.[69] studied thermal annealing processes using Raman scattering on HOPG samples implanted with 100 keV B⁺ ions at doses of 1×10^{14} to 2.5×10^{16} B⁺/cm². They observed a partial restoration of crystalline order with a decrease in the D-peak for the annealing at 1223 K for 1800 s (Figure 24). Niwase et al.[94] used Raman scattering to study isochronal annealing following 25 keV D^+ irradiation of HOPG below 1×10^{16} ions/cm² and found a relaxation of disorder below 873 K; a result that was suggested to indicate the presence of dose-dependent stable/unstable defects. Of interest is that this temperature is lower than that for bulk graphitization of carbon films and precursor carbons.

B. Real-Time Observation of Raman Spectra and Thermal Relaxation of the Lattice Disorder

With respect to transient behaviors and thermal annealing, few papers had existed until kinetic studies on thermal relaxation of ion-irradiated graphite were performed using real-time Raman measurements.[95-101] For the real-time Raman measurement studies, ion irradiation was performed for 300 s giving a total ion dose of 3×10^{13} ions/cm² in which graphite loss due to sputtering was negligible, and the basal plane structure of graphite was maintained. Figure 44 shows typical first-order Raman spectra of HOPG during and after 3-keV He⁺ irradiation at a sample temperature of 453 K.[96,98] The D-peak induced by irradiation increased as the irradiation time increased (curve b and c). After which ion irradiation was stopped, Raman measurements were continued while maintaining the sample at 453 K. Curves d and e show the spectra obtained at 700 and 3000 s, respectively, after stopping ion irradiation, where the D-peak markedly decreases in comparison to that in curve c.

Figure 45a shows the corresponding time dependence of the peak intensity ratio (R = D/G) at room temperature up to a time period of 5 ks, where R increases proportionally to the square root of ion irradiation time ($t < 300$ s) and reaches ≈ 0.8 at $t = 300$ s.[96] After ion irradiation is stopped ($t > 300$ s), R remains almost constant. At 393 K (Figure 45b), R shows a similar behavior to that for room temperature, although it slowly decreases after irradiation stops. With a sample temperature of 453 K (Figure 46c), R increases during irradiation to a maximum of ≈ 0.7, where the increase is not proportional to the square root of the irradiation time. Once the irradiation is stopped, it rapidly decreases ($t > 300$ s) to 0.37 within 700 s. After $t > 1000$ s, R slowly falls to ≈ 0.3. Figure 45(d) shows corresponding results at 473 K, where R only increases to

324
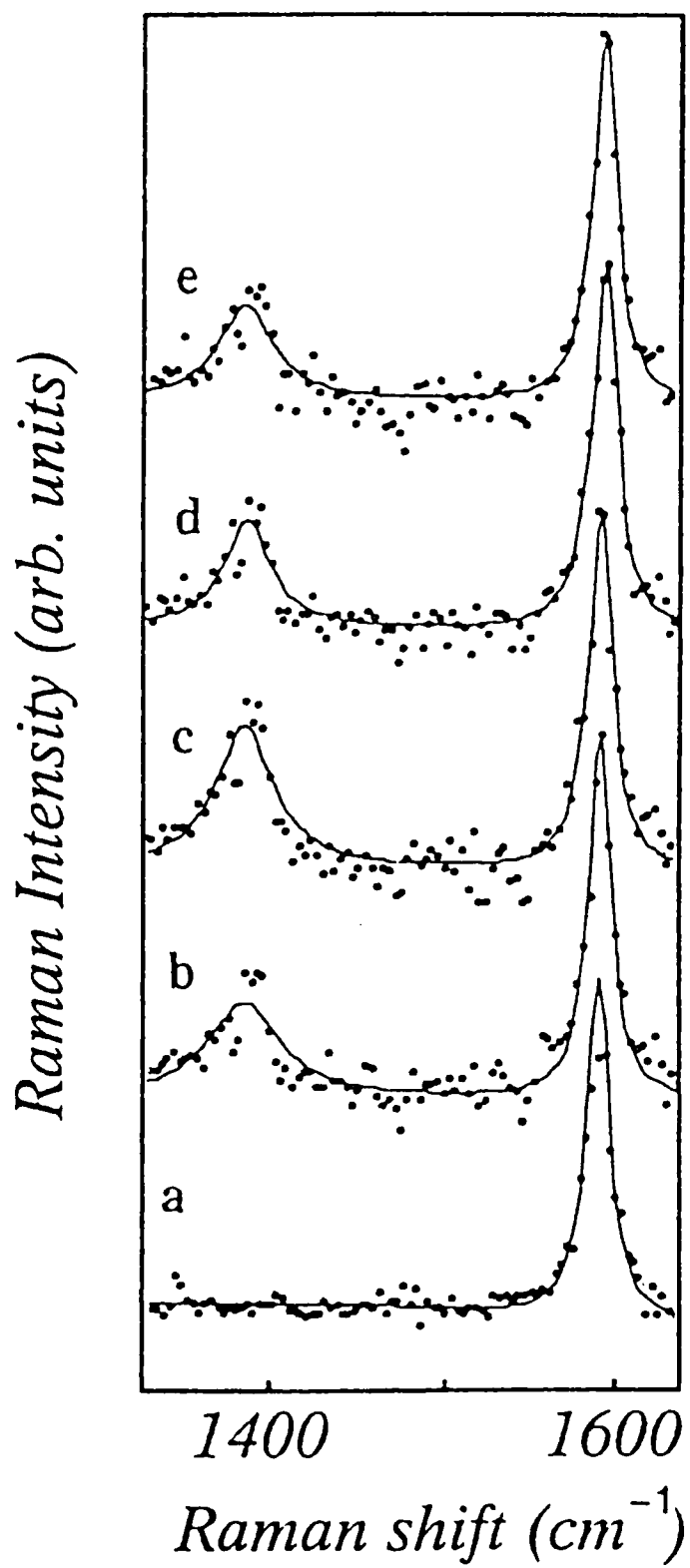
FIGURE 44. Raman spectra of HOPG at 453 K: (a) before ion irradiation, (b) and (c) obtained after 150 and 300 s of 3 keV He^+ irradiation at a flux of 1×10^{11} ions/cm^2 s, respectively, and (d) and (e), respectively, obtained at 700 and 3000 s after the stop of irradiation.[96]
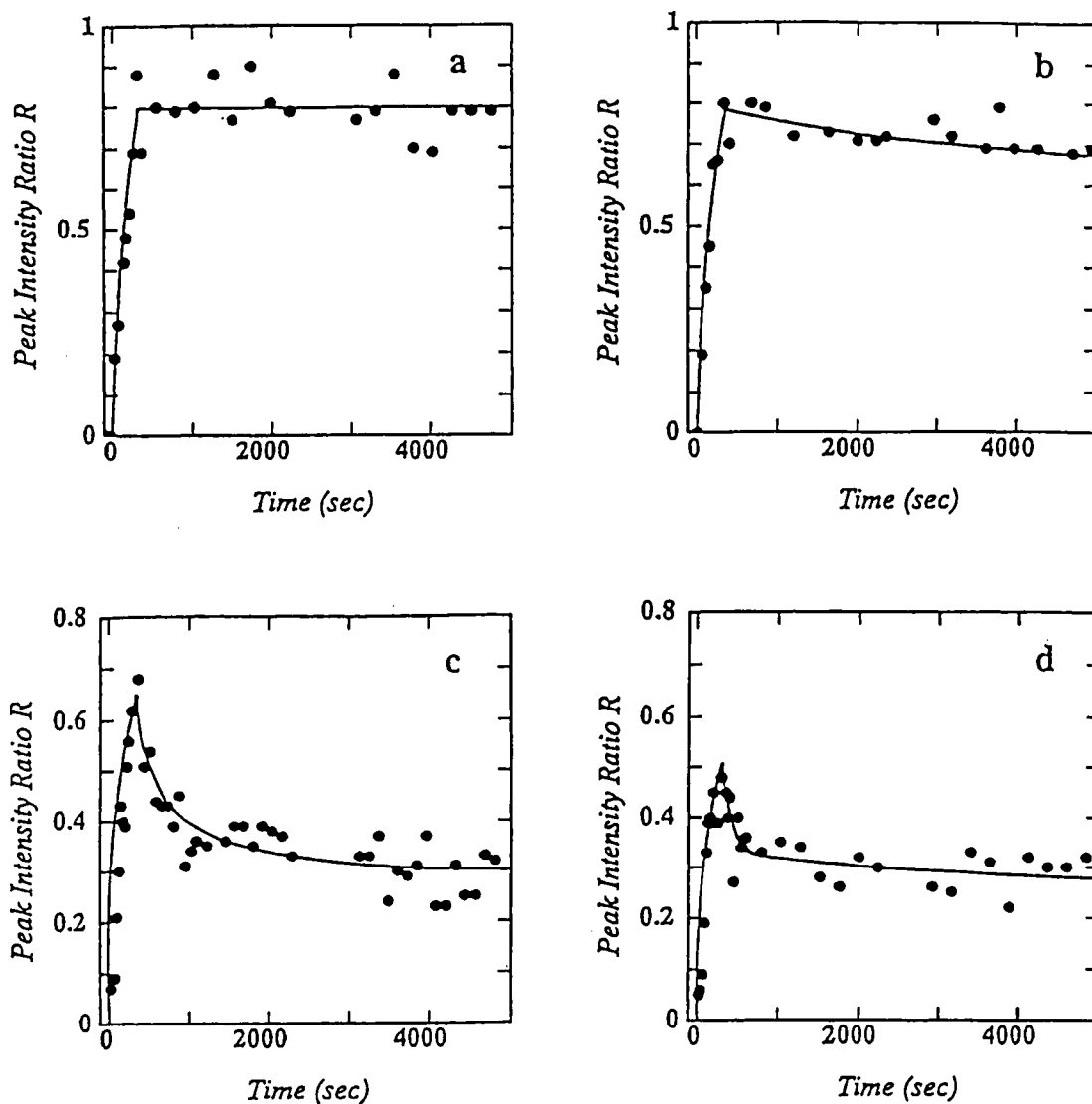
FIGURE 45. Time dependence of the relative intensity R for 3 keV He$^+$ irradiation of HOPG at (a) room temperature, (b) 393 K, (c) 453 K, and (d) 473 K. He$^+$ irradiation was performed under 1.0×10^{11} ions/cm^2 s in the first 300 s. Solid curve is a result of a least-squares calculation based on Eq. 21 (<300 s) and Eq. 22 (>300 s).[96]

≈0.48, and decreases slightly to 0.37 immediately after irradiation, followed by a gradual reduction. The results show thermal relaxation of the irradiation-induced lattice disorder following the creation of the disorder during ion irradiation ($t < 300$ s). It should be noted that the thermal relaxation may include two processes (at least) having fast and slow relaxation rates.

C. Thermal Relaxation Rate

The thermal relaxation behavior of the lattice disorder is discussed in terms of the IDD model modified to incorporate defect annihilation effects. The model was inspired by the measured time dependence of the Raman spectrum (Figures 45c and 45d), which suggests the presence of two pro-
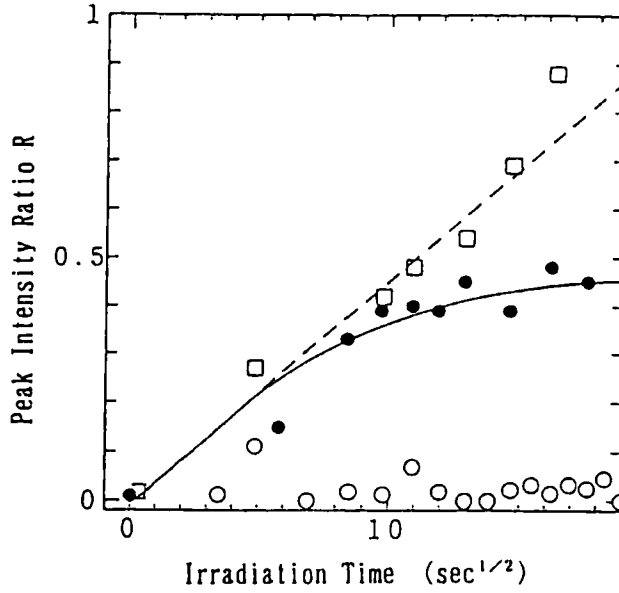
FIGURE 46. Time dependence of R for HOPG during 3 keV He⁺ irradiation at a room temperature (square), 473 K (solid circle), and 573 K (circle), respectively. Solid curve is a result of least-squares root calculation by Eq. 21, and the dashed line that of Eq. 21 neglecting the fast relaxation process(I).[96,98]

cesses that increase the phonon correlation length, that is, a fast process (I) and slow one (II). It is assumed that some of the defects are annihilated by the fast process (I), and the rest are annihilated by the slow process (II), and that both processes occur independently. The rates of defect density are expressed by a sum of defect creation term and the defect annihilation term due to thermal relaxation. The time dependence of R during irradiation is given by[96]

$$R = B\left\{A\left[1 - \exp\left(-k_I t\right)\right]/k_I\right.$$

$$\left. + (1 - A)\left[1 - \exp\left(-k_{II} t\right)\right]/k_{II}\right\}^{1/2} \quad (21)$$

and R after stopping irradiation is

$$R = B\left\{A\left[1 - \exp\left(-k_I t_0\right)\right]\exp\left[-k_I\left(t - t_0\right)\right]/k_I\right.$$

$$\left. + (1 - A)\left[1 - \exp\left(-k_{II} t_0\right)\right] \times \exp\left[-k_{II}\left(t - t_0\right)\right]/k_{II}\right\}^{1/2} \quad (22)$$

where k_I and k_{II} are the thermal relaxation rates of the defects, t_0 is the time at which ion irradiation is stopped, A is a constant and $B = C(fN\sigma v\phi)^{1/2}$. If the relaxation rate is small enough, the value of R during irradiation becomes equal to Eq. 19 and is proportional to the square root of the irradiation time that corresponds to the result of room temperature. Essentially, the same thermal relaxation behaviors were confirmed for graphite under irradiation of hydrogen and neon ions.[97,99]

Figures 45a to d also show the calculation results using Eqs. 21 and 22. Note the good agreement between the calculation and the experimental data. The calculation reproduced especially well the decay curve for the two relaxation rates observed at 453 and 473 K. The rate constant k_I was much higher than k_{II}, for example, k_I and k_{II} at 453 K are $(4.6 \pm 0.8) \times 10^{-3}$ and $(1.4 \pm 0.4) \times 10^{-4}$ s⁻¹, respectively. Figure 46 shows R vs. the square root of the irradiation time during ion irradiation.[96,98] R calculated with the small rate constant $(k_I < 10^{-6}$ s⁻¹) is propor-

tional to the square root of irradiation time (dashed line), following Eq. 19. The solid line shows the calculation with the rate constant k_I at 473 K (1×10^{-2} s^{-1}). The deviation away from the straight line indicates that the fast process (I) for defect annihilation is also occurring strongly during ion irradiation. No increase in R is observed at 573 K, showing that the defect annihilation rate is higher than the creation rate at this temperature.

Figure 47 shows an Arrhenius plot of the rate constants k_I and k_{II}. Activation energies for relaxation process (I) and (II) were determined from the slopes to be 0.89 ± 0.10 and 1.8 ± 0.3 eV, respectively. Söder et al.[102] investigated ion-beam-induced self-diffusion in pyrolytic graphite using Rutherford backscattering and a model calculation, and subsequently obtained a rate constants for both interstitial-vacancy recombination and vacancy-vacancy annihi-

lation. On the basis of their study, the activation energy for the annihilation of vacancies through the vacancy-interstitial recombination process was 0.65 eV. It should be noted that this energy value is close to the activation energy of the fast relaxation process (I). Therefore, the fast relaxation process (I) was suggested to be a recombination of vacancies and single interstitials through in-plane migration of interstitials, resulting in increase in La (Figure 48).

A very recent measurement spanning a longer time period of 40 ks at 433 K made clear that the slow rate process (II) is further composed with two stages (stage II' and stage III') (Figure 49).[100] Single interstitials (single vacancies) migrate faster than the interstitials cluster (vacancies cluster), and the activation energies for in-plane migration for single-interstitial and di-interstitial are 0.14 and 0.86 eV.[75] The activation energy for vacancy diffusion in the basal plane
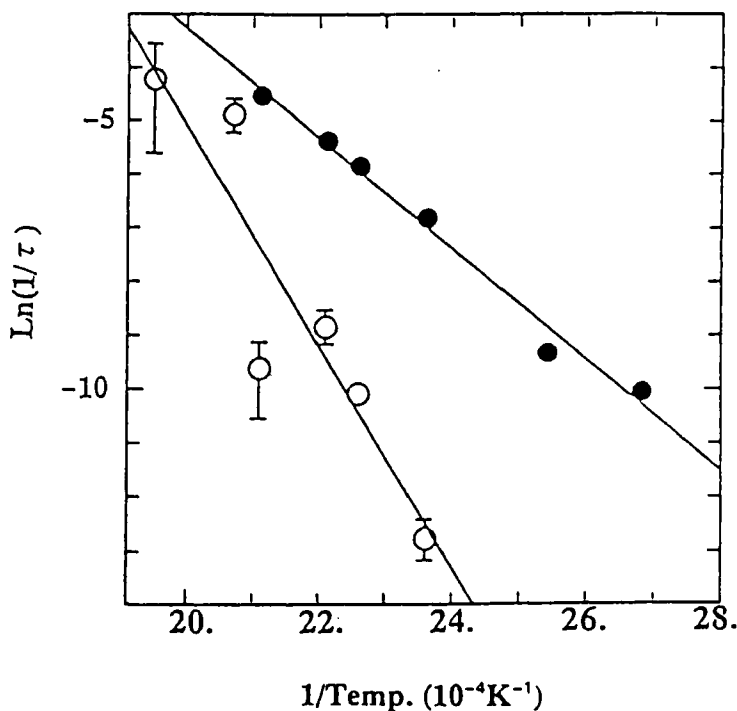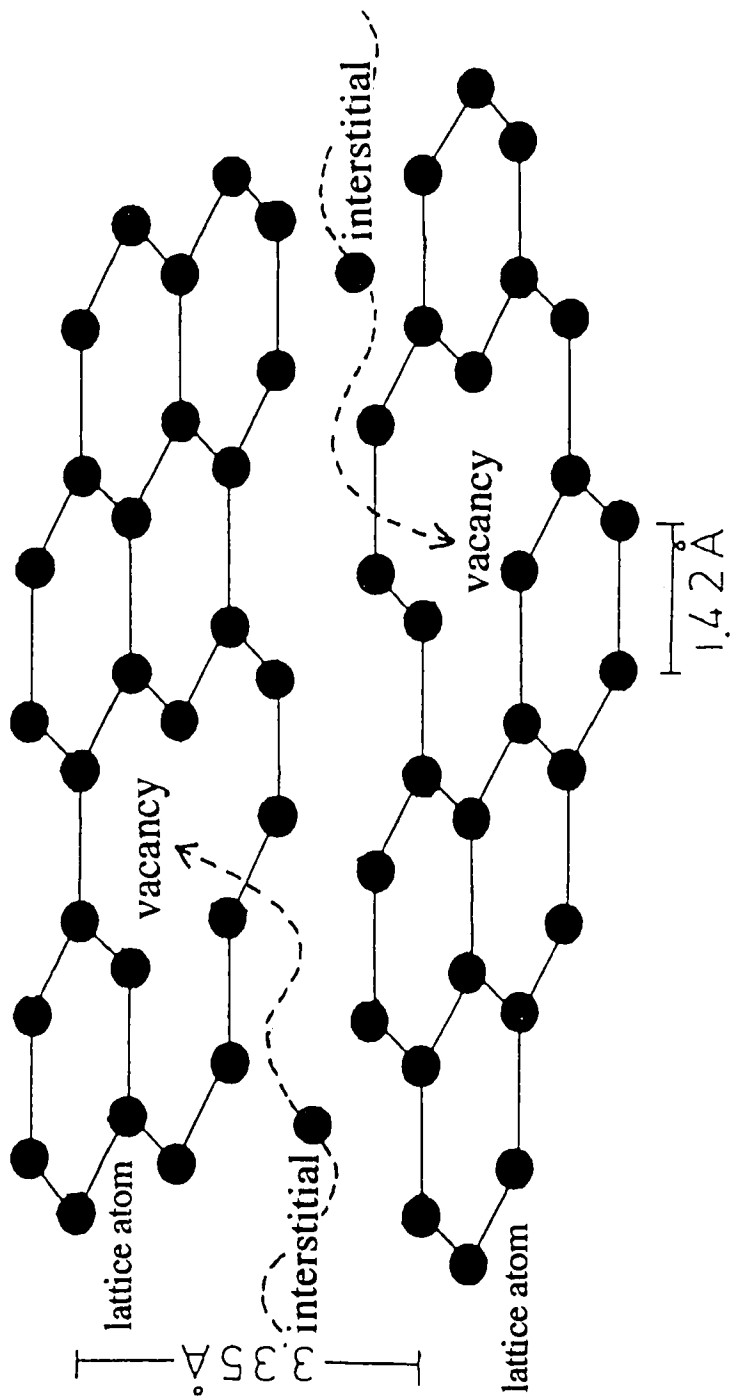

FIGURE 47. Arrhenius plot of reciprocals of time constants $1/\tau_1$ ($=k_I$) (solid circle) and $1/\tau_2$ ($=k_{II}$) (circle) for HOPG.[96]

FIGURE 48. Recombination process of vacancies and interstitials in graphite. The defects annihilate through the vacancy-interstitial recombination process, and the phonon correlation length would increase by thermal relaxation.[82]
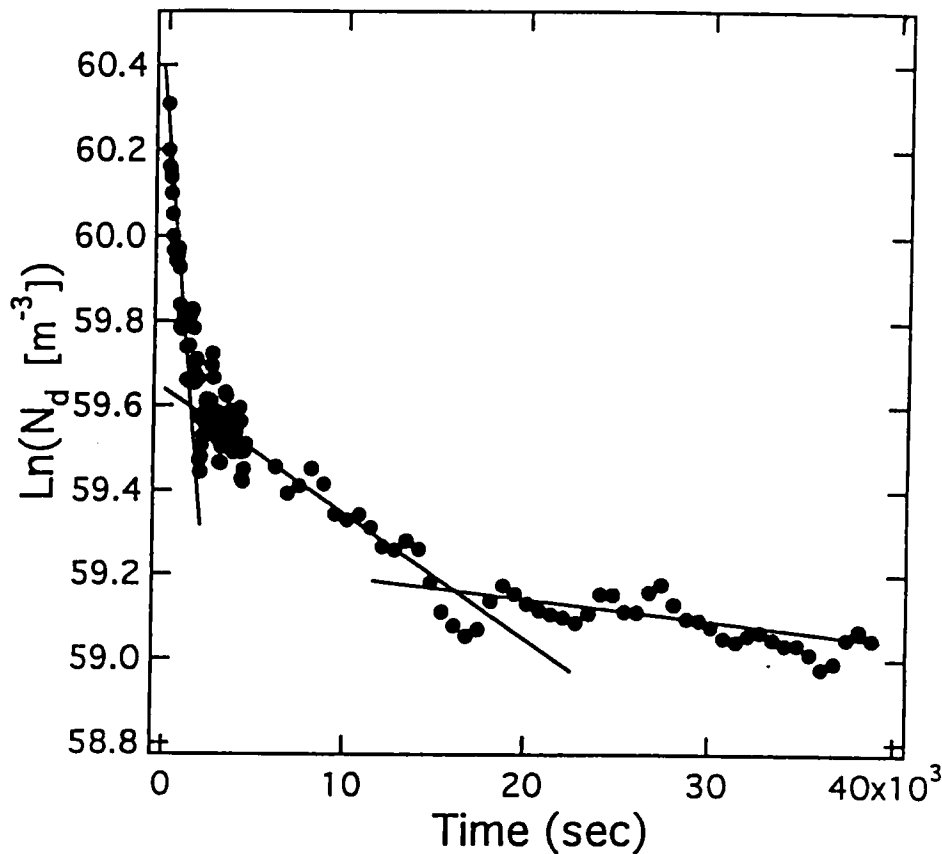
FIGURE 49. Plot of ln N_d vs. time at 433 K for HOPG after irradiated 2.7 × 10^15 ions/cm² s for 300 s at 5 keV deuterium ions.[100] For the notation, N_d means the number density of defects.

is ≈3.1 eV, being much higher than that for the in-plane interstitial migration.[103] Iwata et al.[104] pointed out that the single interstitials start to migrate around 10 K and the di-interstitials recombine with vacancies through di-interstitial diffusion around 473 K. The latter temperature, 473 K, is comparable to the Raman measurement temperature (433 K). Therefore, it is possible that the annihilation process of vacancies occurs through the in-plane migration of di-interstitials. The relaxation process II' was suggested to be a recombination process of single vacancies and di-interstitials that was proposed by Iwata et al. The slowest relaxation process III' was deduced to be dominated by a combination of other slower processes, for example, clustering of single

vacancies and migrations of larger interstitial clusters and vacancies clusters.[100]

VII. LOCALIZED MODES OF DEFECTS IN CRYSTALS

Localized vibration modes provide detailed and more intuitive information about identity and the lattice location of both isolated and compexed impurity atoms in crystals. Many papers have reported on chemical trapping of impurities in crystalline semiconductors[105-106] and other crystals. In particular, because hydrogen is an important impurity in semiconductors and is incorporated during the various stages of semiconductor processing, hydrogen-related

defects in semiconductors have been studied extensively using Raman and infrared (IR) spectroscopy. In this section, we first discuss vibrational modes of the hydrogen-related defects due to Si–H or C–H bonds in crystals. Next, Raman studies on hydrogen molecules in crystalline semiconductors, which is a recent topic in the field of defects in semiconductors, are discussed.

A. Vibrational Spectra of Hydrogen Related Defects

Hydrogen in crystalline silicon has several possible configurations. It terminates dangling bonds on the surface and passivates acceptors, donors, and deep-level impurities in the bulk by forming complexes with the dopants.[107,108] Much of the microscopic information about defect complexes that include hydrogen atoms has come from IR absorption and Raman scattering. Many papers have reported H-stretching vibrations of the acceptor-H and donor-H complexes using IR spectroscopy. Stavola and Pearton reviewed the observation of local vibrational modes for B–H, Al–H, Ga–H, Be–H, As–H, P–H, and Sb–H complexes and their configurations in Si.[109,110] In addition, recently vibrational modes of H-O and H-O-vacancy complexes were suggested to form.[111,112] Si–H,[109,113,114] C–H,[115,116] and C₂–H[110] complexes were also observed in GaAs with IR absorption. Here, we do not describe the details of the IR studies.

Using Raman spectroscopy, Stutzmann et al. investigated p-type crystalline Si doped with 1.3×10^{20} B cm^{-3} after exposure to a remote deuterium plasma.[117] When the D-content within the optical penetration depth was comparable to the B-concentration, only a characteristic vibration of the B-D complexes at 1365 cm^{-1} was observed at 300 K (Figure 50a). For D-concentrations largely exceeding the B-doping level, at least

four new deuterium related local modes (1405, 1602, 1623, and 1695 cm^{-1}) were observed (Figure 50c). These Raman lines were suggested to relate to formation of quite specific types of lattice defects: Si–D complexes (but not like "platelets").[120] They also investigated Si doped with 6×10^{19} B cm^{-3} and found a strong temperature dependence (5 to 300 K) of vibrational modes of Si–H complex.[118]

Chemical trapping of hydrogen in the substrate lattice can be evidenced by the appearance of local vibrational modes such as Si–H, and Ge–H in Si and Ge, respectively. Raman and IR spectroscopy are complementary tools to study the configurations of these hydrogen-induced defects. One of the advantages for using Raman spectroscopy is that we can compare local modes with optical phonon modes of the substrate lattice. To restate, it is possible to relate the configuration of hydrogen-related defects to the degree of lattice disorder. Gruen et al.[119] performed a systematic Raman measurement combined with IR on 5 to 15 keV proton and deuteron irradiated Si and Ge (Figure 51). The local vibrational mode frequency of Si–D is very broad and exhibited overlapping doublets around 1500 cm^{-1} for Si irradiated with 15 keV 0.8×10^{18} D$^+$/cm^2 at 23°C. Raman spectra of this sample showed essentially the same Si–D stretching mode feature observed by IR absorption. The optical phonon band of Si observed around 520 cm^{-1} was greatly broadened by deuteron irradiation, suggesting amorphization. After progressive annealing, one of the broad band components of Si–D disappeared (Figure 51), as well as sharpening of the optical phonon of Si: increasing the phonon correlation length (Figure 52). The similar annealing behaviors were confirmed for the irradiated Ge.[119] The results showed that one of the different trapping sites in Si and Ge is inferred to be less stable during recrystallization. These results are
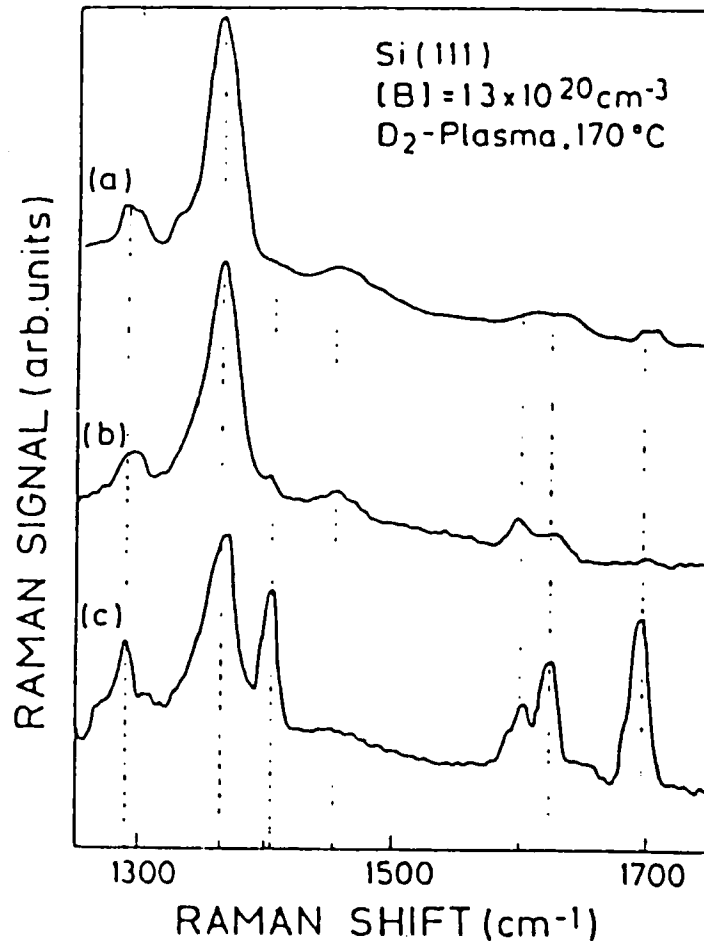
FIGURE 50. Room temperature Raman spectra of deuterium-passivated P-type Si. The total deuterium-concentration in the scattering depth probed by the experiment is (a) $\approx 2 \times 10^{20}$ cm^{-3}, (b) $\approx 5 \times 10^{20}$ cm^{-3}, (c) $\approx 2 \times 10^{21}$ cm^{-3}.[117]

important because they indicate a clear correlation between the hydrogen related local modes and the lattice disorder, although phonon confinement due to the defects was not discussed in a quantitative manner.

Hydrogen, introduced into n-type crystalline silicon at moderate temperatures (e.g., ≤250°C), can generate extended structural defects. These defects are planar in shape, are aligned predominantly along {111}-crystallographic planes, and a consequence of the coordinated formation of S–H bonds.[120,121] This platelet was suggested from TEM measurements to have an average di-

ameter of about 7 nm containing ~400 Si–H bonds.[120,121] This hydrogen-induced platelet was studied by several authors from Raman scattering.[117,120,122,123] Heyman et al.[122] performed a precise measurement on the local modes of S–H bonds of an n-type crystalline Si hydrogenated by a remote hydrogen plasma at 150°C. The Raman spectra of local vibrational modes at different annealing temperatures, together with the corresponding IR spectra, are shown in Figure 53. They attributed the local modes observed at 2065, 2095, and 2125 cm^{-1} to the hydrogen-induced platelets in crystalline Si.
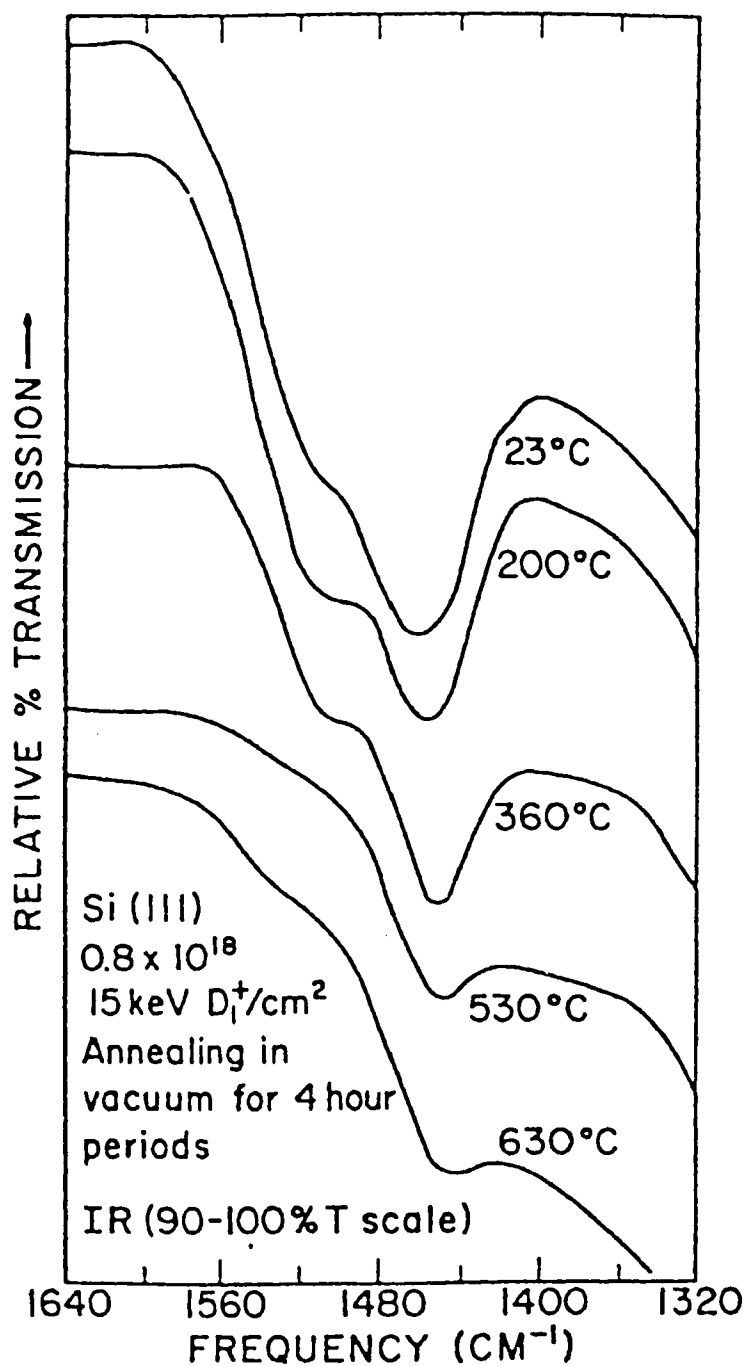
FIGURE 51. Infrared spectra of Si (III) disk bombarded with 15 keV 0.8×10^{18} D^+_I/cm^2; annealing in vacuum for 4-h periods at 23, 200, 360, 530, and 630°C.[119] A similar information was obtained from Raman measurements.

Recently, Fukata et al.[123] found two broad local vibrational modes of Si–H bonds at 2100 and 2130 cm⁻¹ in Raman spectra for

an n-type crystalline Si after a remote hydrogen atom treatment at hydrogenation temperatures of 150 to 180°C, as shown
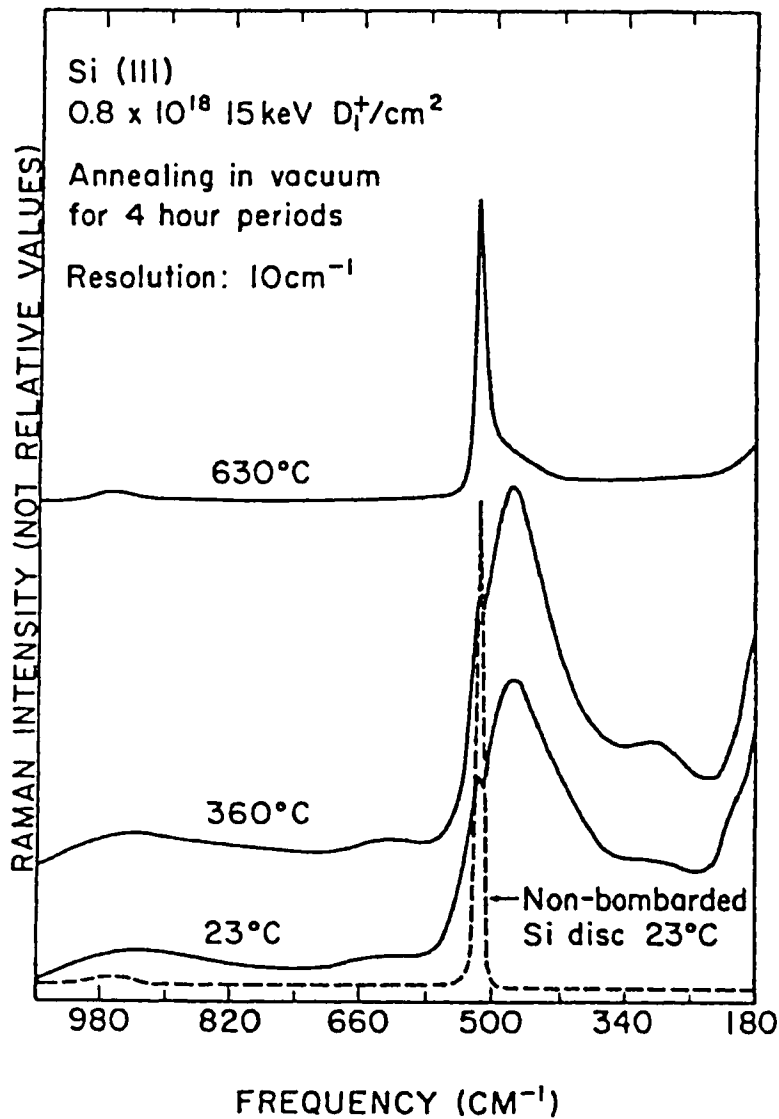
FIGURE 52. Raman spectra of Si (III) disk bombarded with 15 keV 0.8×10^{18} D^+_I/cm^2. Raman scattering spectra of ion-implanted surface were recorded at different stages of isochronal annealing.[119]

with a curve (b) in Figure 54. These frequencies were seen to correspond to the two of those observed by Heyman et al., and agree well with theoretical values, 2095 and 2122 cm^{-1}, obtained using the self-consistent semiempirical MINDO/3 Hamiltonian, where pairs of hydrogen atoms saturate the broken bonds between two adjacent Si atoms.[124] They further found a difference in the thermal stability between the two localized modes: the component at 2100 cm^{-1} was still present at hydrogenation up to 500°C, while that at 2130 cm^{-1} vanished for hydrogenation temperatures above 250°C. They attributed the peak component at 2130 cm^{-1} to the Si–H bonds in platelets and 2100 cm^{-1} to more isolated Si–H bonds than those in platelets, because the TEM observation showed that the platelets were not stable above 250°C.[120,121] The higher frequency of the platelet's Si–H band suggests that the Si–H bonds are constrained exhib-
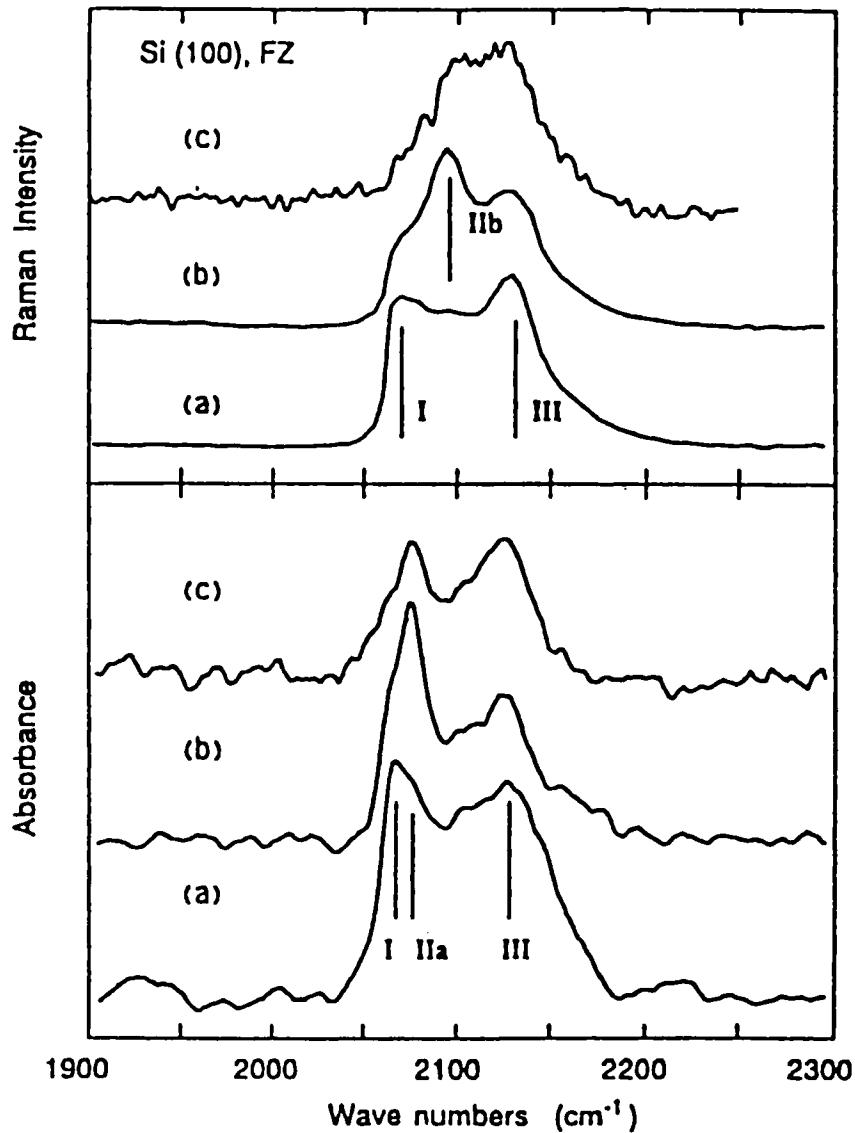
FIGURE 53. Raman (top) and infrared (bottom) measurements of the local vibrational models in the same FZ n-Si sample as a function of annealing. (a) After exposure to a hydrogen plasma for 150°C (20 min) and 275°C (60 min). (b) An additional vacuum anneal at 300°C (30 min). (c) An additional vacuum anneal at 400°C (40 min).[122]

iting a compressive stress. At higher temperatures the compressed Si–H bonds would relax and thus the Si–H band frequency would decrease. Local vibrational modes of the Si–H bonds were also observed in amorphous Si:H[125,126] and reactive ion-etched[127] or hydrogen adsorbed[128] silicon surfaces using Raman techniques (the surface trapping modes are not within the scope of this review).

Local vibrational modes of Si–H and C–H bonds were also observed in proton- or deuteron-irradiated SiC. Figure 55 shows the Raman spectra of SiC after irradiation with 15 keV D^+ to a dose of 3×10^{18} cm^{-2} and H^+ to 1.5×10^{19} cm^{-2} (spectrum b and c, respectively).[73] The weak, broad band around 2100 cm^{-1} was attributed to the Si–H local vibrational mode and broad band appearing at 2925 cm^{-1} was analogously
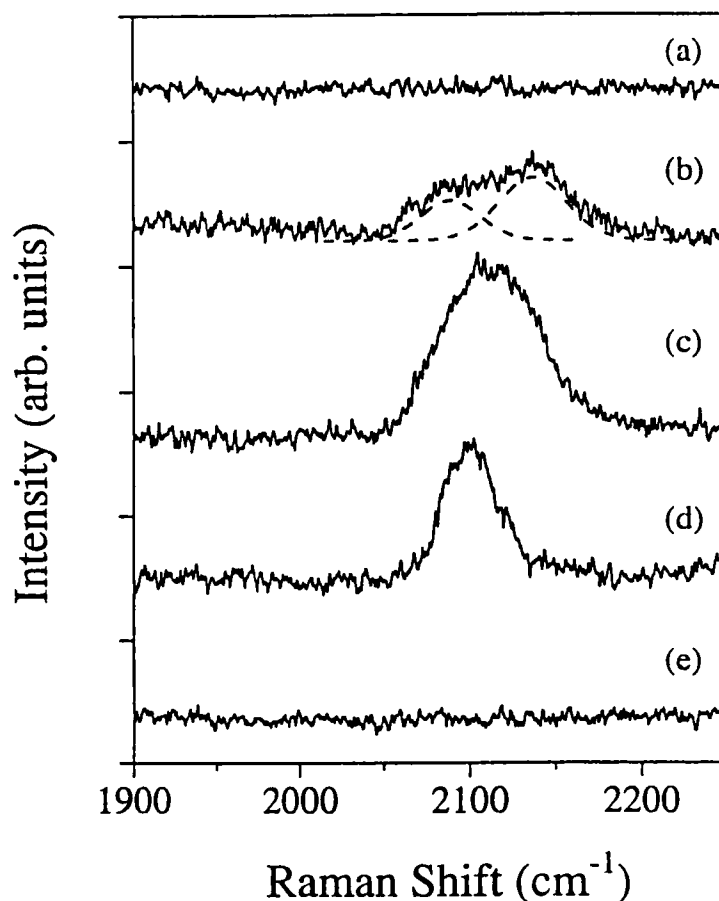
FIGURE 54. Raman spectra of Si–H stretching for crystalline (a) before hydrogenation and after treatment with atomic hydrogens at (b) 180°C, (c) 250°C, and (d) 400°C.[123]

attributed to local vibrational mode of C–H. In the deuteron-irradiated SiC a broad band around 2150 cm⁻¹ was expected to be C–D local mode. The C–D local band was also observed in graphite after exposure to a deuterium plasma at room temperature.[71]

B. Hydrogen Molecules in Crystals

1. Observation of Hydrogen Molecule by Raman Scattering

Molecules without a dipole moment cannot be detected by infrared absorption but they are Raman active (Section II). For example, vibrational modes of C–C pairs

were reported to be detected by Raman sacttering as an impurity-induced defect in GaAs.[134] A metastable configuration H_2^* was proposed as another type of hydrogen molecule in crystalline Si.[129] This was predicted to consist of a bond-center hydrogen and a hydrogen at a neighboring tetrahedral interstitial site and has an energy that is 0.01 eV higher than the most stable hydrogen molecule. Recently, this metastable hydrogen molecule was reported to be observed in H⁺ implanted silicon.[130] For amorphous Si:H, on the other hand, hydrogen molecules in voids have been directly detected by IR absorption.[131] The existence of deuterium molecules was also suggested by Raman measurement of amorphized
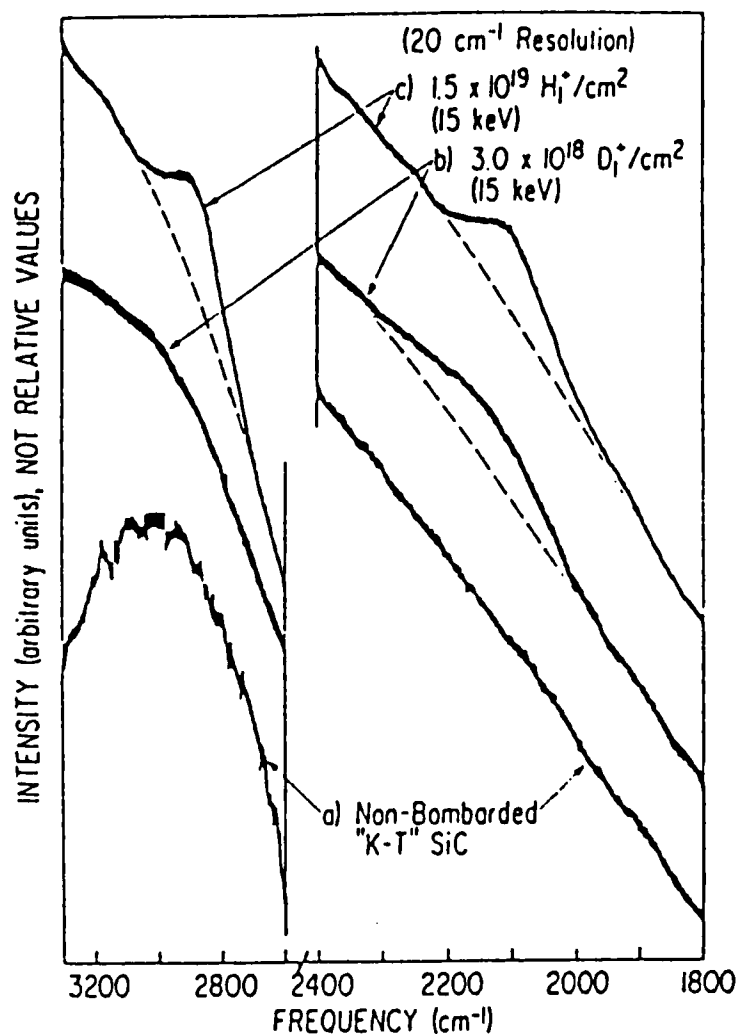
FIGURE 55. Raman spectra (1800 to 2400 cm^{-1} and 2600 to 3300 cm^{-1}; note frequency scale change) of SiC: (a) before bombardment, (b) bombarded with 15 keV D$^+$, to a dose of 3.0×10^{18} cm^{-2}, (c) bombarded with 15 keV H$^+$, to a dose of 1.5×10^{19} cm^{-2}.[73]

graphite surface layer exposed to a deuterium glow discharge.[71] In crystalline silicon, theoretical calculations predicted that the hydrogen molecule was stable at tetrahedral interstitial sites in silicon with its axis along a <100> (or <111>) direction[129,135] (Figure 56). However, direct observation of hydrogen molecules were lacking until the recent Raman studies on hydrogenated crystals were reported.[132]

Murakami et al.[132] observed for the first time hydrogen molecules in crystalline sili-

con by detecting their vibrational and rotational Raman lines after a remote hydrogen atom treatment at substrate temperatures of 60 to 600°C. Figure 57a shows a Raman spectrum of crystalline Si after treatment with atomic hydrogen at 400°C. In addition to the local vibrational modes of Si–H bonds around 2100 cm^{-1}, broad Raman lines were observed at around 590 cm^{-1} and 4158 ± 3 cm^{-1} and were assigned to the $S_0(1)$ rotational line and the Q_1 vibrational line of H_2, respectively. Both p-type Si and heavily
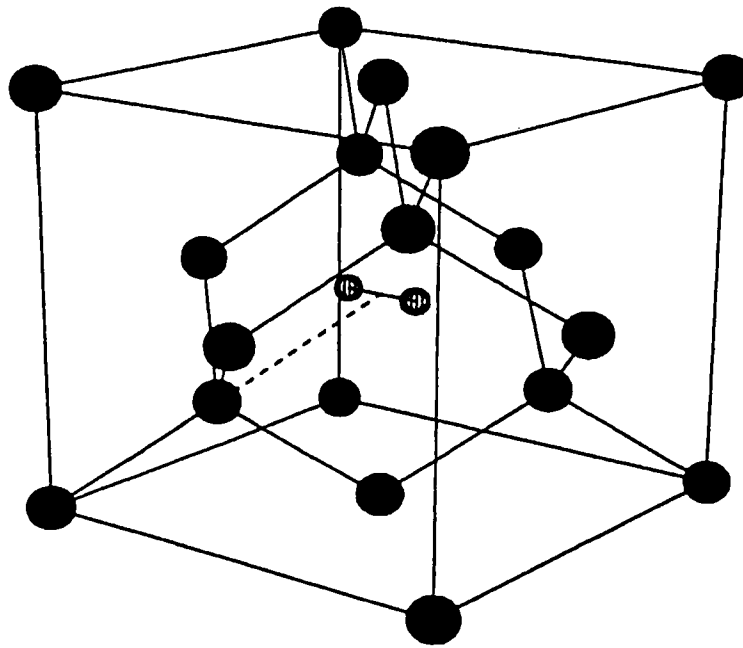
FIGURE 56.   Schematic illustration of the minimum energy position of a H_2 molecule in the Si crystal: located at the tetrahedral interstitial site and oriented along <100>.[141]
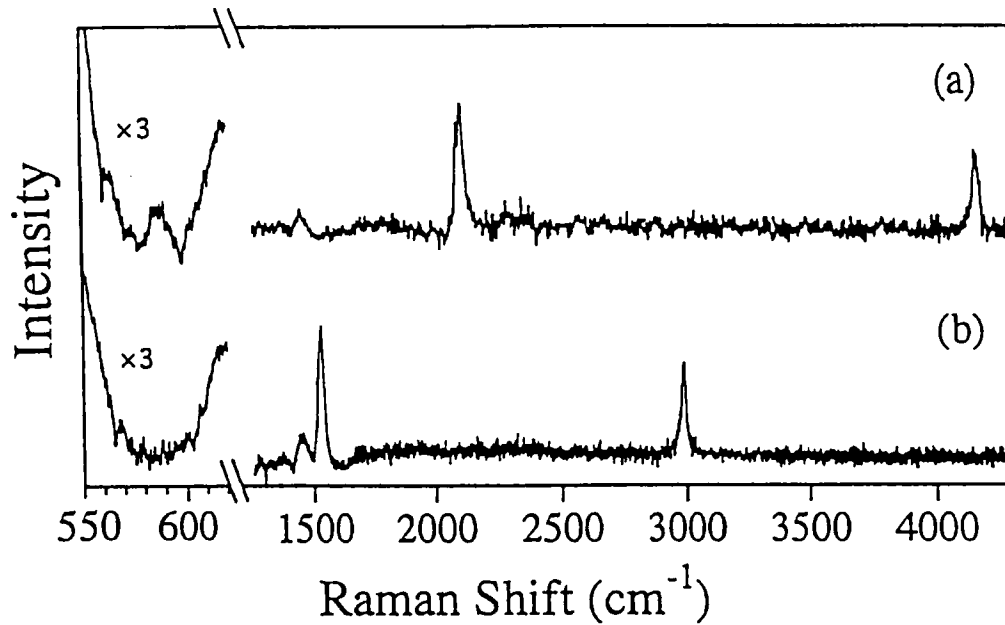
FIGURE 57.   Typical Raman spectra of crystalline Si (a) after treatment with H atoms at 400°C and (b) after treatment with D atoms at 400°C.[123]

doped n-type Si were examined, and no significant difference in the Raman spectrum due to the sample difference was observed.[136,137] In crystalline Si treated with deuterium atoms, the Q_1 vibrational line (D_2) and the Si–D stretching line occurred at 2990 cm^{-1} and at 1530 cm^{-1}, respectively (Figure 57b). The isotope shift confirmed the existence of hydrogen molecules in crystalline Si. The Raman spectra depth profiling of in Si obtained by a chemical etching of the surface layers showed that H_2 was present down to a depth of about 120 nm from the surface. To restate, H_2 exists not only near the surface but also in the bulk Si

crystal.[137] A plausible trapping site of H_2 is the tetrahedral interstitial (T_d) site in crystalline Si,[123,132] which was previously predicted by the theoretical calculations.

Fukata et al.[123] performed a systematic study on the hydrogenation temperature effect on the formation of hydrogen molecules. Figure 58 shows the vibrational lines of H_2 of Si crystal treated with atomic hydrogen at various temperatures. The intensities of the vibrational lines were largest at a hydrogenation temperature of 400°C, while that of the Si–H stretching line had a maximum at 250°C. as shown in Figure 59.[123,136] The vibrational line of H_2 was significantly
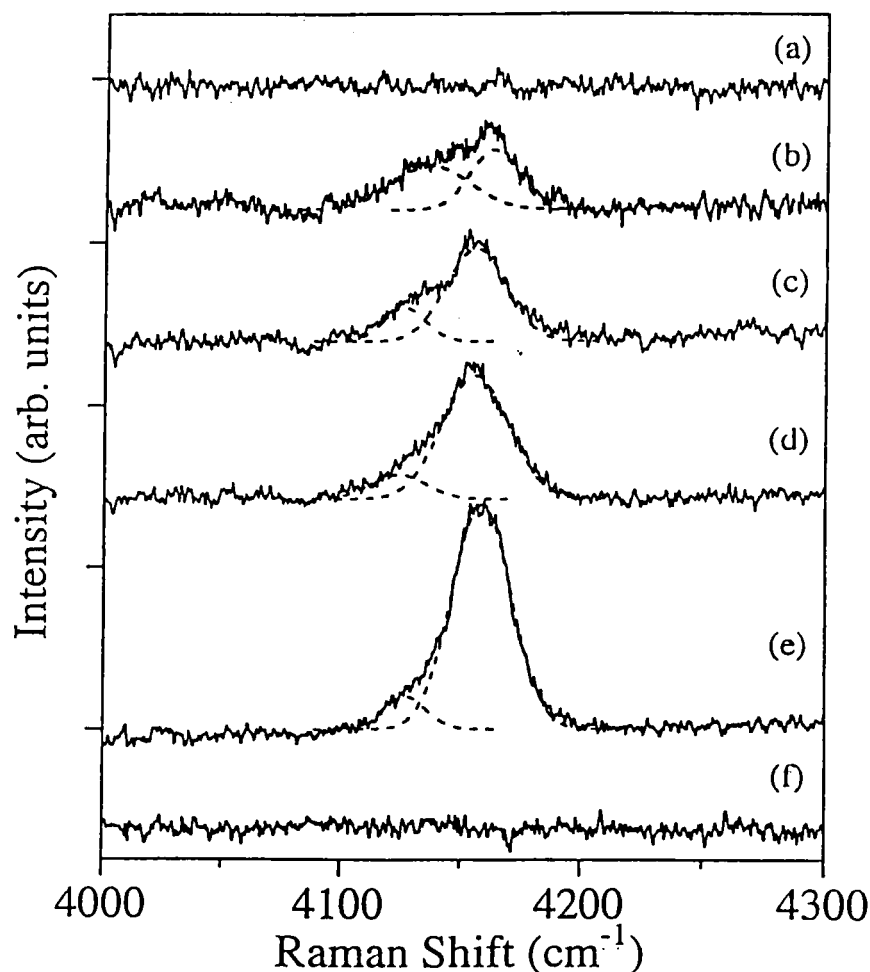
FIGURE 58. The vibrational Raman line of H_2 in crystalline Si (a) before hydrogenation, and after hydrogenation at (b) 180°C, (c) 250°C, (d) 300°C, (e) 400°C, and (f) 600°C.[123]
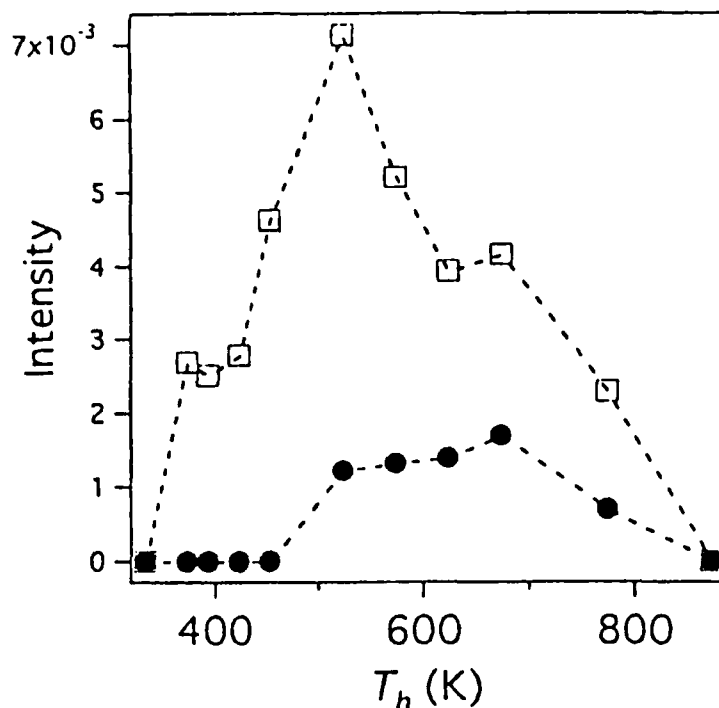
FIGURE 59. The intensities of the Q_1 line of H_2 (solid circle) and the Si–H stretching line (square) in heavily doped n-type silicon as a function of hydrogenation temperature (T_h) measured at 300 K. The intensities are normalized by that of the phonon peak of Si.[136]

asymmetric with a shoulder at around 4130 cm^{-1} for crystalline Si hydrogenated at 250°C, which corresponds to the maximum formation of Si–H. The main peak at 4160 cm^{-1} was attributed to H_2 trapped in the tetrahedral sites of the well-ordered silicon lattice, whereas the shoulder around 4130 cm^{-1} was inferred to arise from H_2 in the T_d sites of the distorted lattice: the distortion caused by the existence of Si–H bonds in the vicinity.[123,137]

It was noted that the widths of the vibrational lines were much larger than those of gaseous or solid hydrogen molecules, while the Raman shifts were comparable. Recently, Leitch et al. confirmed quite similar Raman spectra for crystalline Si treated with a hydrogen plasma.[138] The linewidth of the vibrational line gradually decreased with increasing hydrogenation temperature, from about 50 cm^{-1} for 180°C hydrogenation to

30 cm^{-1} for 500°C. The broadening of the Raman lines of H_2 is too large to be explained by high-pressure gaseous H_2. In fact, the vibrational Raman line of gaseous H_2 at a pressure of 200 MPa, the pressure of gaseous H_2 in voids in amorphous silicon,[131] has a width no more than 3 cm^{-1}.[139] On the other hand, for H_2 dissolved in vitreous silica the spectral linewidth was about 20 cm^{-1} at room temperature and exhibited significant narrowing with decreasing measurement temperature.[140] The temperature-dependent part of the width was explained in terms of collisional or motional broadening. To examine the origin of the large linewidth of H_2 in crystalline Si, Raman measurements were also performed at 90 K. No significant difference was observed after lowering the temperature to 90 K. More precise measurements were performed by Leitch et al.,[138] and no temperature dependence of the

linewidth was detected from 4 to 300 K. These results clearly indicate that the broadening is not attributed to collisional broadening in a high-pressure gas or other motional broadening, but predominantly to inhomogeneous broadening due to various configurations in Si crystal. Most of H_2 molecules were deduced to be trapped, isolated in crystalline Si;[123,137] to restate, H_2 molecules are not present as a high-pressurized gas in a free space like a void or platelet.

In order to investigate the thermal stability of H_2 in Si, crystalline Si was treated with hydrogen atoms at 250°C for 3 h and then thermal annealed at temperatures from 300 to 500°C.[142] It was evident that H_2 was stably trapped in the crystalline silicon up to ≈400°C because the intensity of the H_2 stretching mode and the line shape were almost constant up to 400°C with a similar lineshape. The Raman intensity of the Si–H bonds monotonically decreased as the annealing temperature increased. There was no strong correlation in the annealing behavior between the Si–H bonds and H_2.

The effect of crystal disorder on the formation of H_2 was examined. Raman measurements were performed on microcrystalline and amorphous Si treated with atomic hydrogen.[143] A vibrational line of H_2 was observed in microcrystalline Si after hydrogenation, and its intensity in microcrystalline was one fifth of that observed in the crystalline Si. No Raman signals due to hydrogen molecules were observed in amorphous Si. These results show that H_2 is trapped in non-damaged, well-ordered bulk crystal.

Molecular hydrogen was also observed in crystalline GaAs. Vetterhoeffer et al.[133] exposed crystalline GaAs to a hydrogen/deuterium plasma and measured the Raman spectra. Using a pure hydrogen plasma, a doublet was observed at 3934 cm⁻¹, as shown in Figure 60a, and the Raman intensity ratio (3:1) was consistent with the expected value
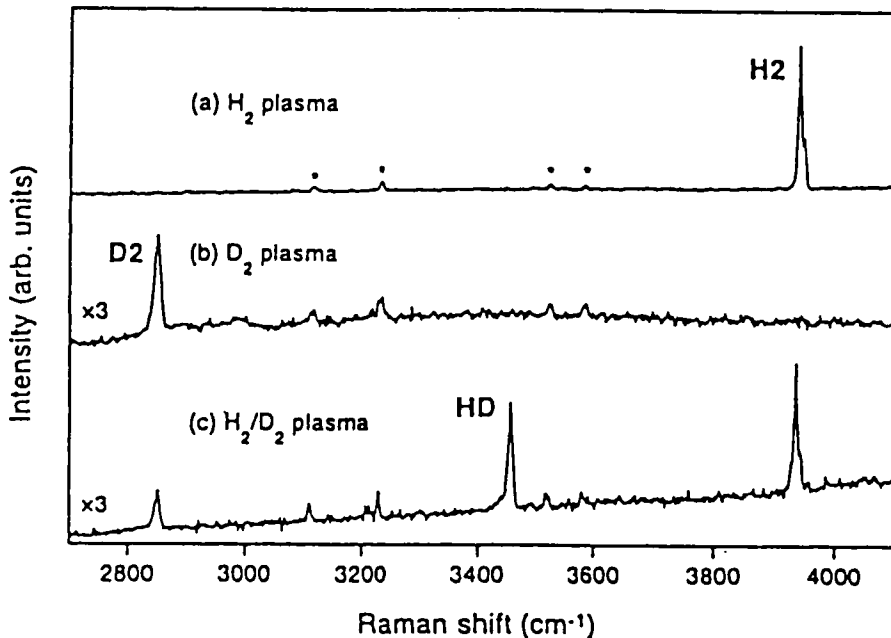
FIGURE 60. Low-temperature (T = 77 K) Raman spectra of three samples after different plasma treatments. (a) GaAs, 8 h H_2 plasma treatment at T = 254°C. (b) GaAs, 3-h D_2 plasma treatment at T = 200°C. (c) GaAs, 8 h 50% H_2/50% D_2 plasma treatment at T = 200°C.[133]

of the ortho/para ratio. Only a singlet line at 2843 cm^{-1} was observed when a pure deuterium plasma was used (Figure 60b). Finally, using a mixture of hydrogen and deuterium gas for the plasma, these lines plus an additional one at an intermediate frequency, 3447 cm^{-1}, appeared (Figure 60c). They assigned these lines as vibrational modes of isolated H_2, D_2, and HD in GaAs, respectively. The H_2 spectra are different in some aspects from those of Si. The Raman line of H_2 in GaAs was sharper (~3 cm^{-1}) and lower in frequency than that in Si. Compared with the Si case, however, we do not have enough information about hydrogen molecules in crystalline GaAs. Further investigation is needed to increase the understanding of the formation of hydrogen molecules in GaAs crystals; areas of interest are precise hydrogenation-temperature dependence, annealing effects, effects of defects in crystal, and effects of near-surface compositional change to be induced by interactions with the hydrogen plasma. The difference in the Raman spectra of hydrogen molecules in Si and GaAs suggests the importance of a systematic study on matrix effects such as ionicity, lattice constant, etc.

Following the Raman studies of hydrogen molecules in crystalline $Si^{132,137}$ and GaAs,[133] it was reported that three hydrogen-stretching modes at 3789, 3731, and 3618 cm^{-1} were observed for Si with oxygen ~10^{18} cm^{-3}.[144] The first two lines with higher frequencies were assigned to hydrogen molecules trapped close to interstitial oxygen atoms, and the line of the lowest frequency to hydrogen molecules trapped by an impurity/defect such as carbon or nitrogen. A reduction in electron density of the H–H bond was inferred to explain the reduced H_2 frequencies and induction of a dipole moment. In their hydrogenation the samples were heated in a 1-atm hydrogen gas at 1000 to 1300°C and cooled rapidly by dropping into a silicon oil rapidly to

room temperature, or were heated in a quartz tube that was withdrawn rapidly from the furnace and plunged into water. Thus, there should be some effects of lattice damage (or defects) on the H_2 formation. The samples should be examined with Raman spectroscopy as well to confirm the existence of hydrogen molecules having no dipole moment.

2. Theoretical Considerations

Finally, we discuss the theoretical calculations of hydrogen molecules in crystals, briefly. "Hydrogen molecule in crystal" is a new type of defect in crystals and thus is attracting much attention, particularly about in which sites H_2 are present in crystals. The frequencies of H_2 vibrational modes in crystalline semiconductors were theoretically calculated by several authors. Nakamura et al. calculated, for the first time, potentials of a hydrogen molecule in a silicon cluster ($Si_{10}H_{16}$) based on an *ab initio* molecular orbital (MO) theory.[145] H_2 exhibited a minimum energy at a T_d site of the cluster, with the molecular axis oriented almost along (100) direction, which corresponds to the result by the Van de Walle.[135] The calculated frequency of H_2 was 4393 cm^{-1}. This value is near to the experimental value, in particular if we consider an unharmonic term of vibration. The linewidth obtained experimentally, about 30 cm^{-1}, was also comparable to the distribution in the vibrational frequency of H_2 in different orientations at the T_d site in Si calculated by the *ab inito* MO theory. Recently, on the other hand, the frequencies of H_2 in the T_d site of crystalline semiconductors were also calculated based on the density functional theory (DFT). Nakamura et al.[146] performed the DFT calculations using small clusters. Van de Walle performed calculations on H_2 in 32-Si-atoms supercells based the local

density approximation (LDA) in the DFT and *ab initio* pseudopotentials for five different semiconductors.[147] Okamoto et al. performed similar calculations based the generalized gradient approximation (GGA) as well as LDA in the DFT.[148] The calculated frequencies by the DFT for Si and GaAs were always downshifted from that for a free H_2; there were differences in the frequency between the DFT calculations[146-148] and the calculated values ranged 3000 to 3700 cm^{-1} for Si and 3500 to 3800 cm^{-1} for GaAs. The observed downshift in frequency for GaAs appears to be explained with the DFT calculations, but for Si not. However, the DFT calculations did not reproduce the H–H distance in a free H_2: the H–H distance was always larger by about 0.03 nm than the experimental value (0.0742 nm).[146-148] Calculations based on the LDA seems to stress the interaction between H_2 and the surrounding lattice. It has not been understood well why there is such a difference in the frequency and the H–H distance between the MO and DFT methods. One should be careful about a choice of the electronic exchange correlation energy and the basis set.[146] At the moment I do not feel that the theories can judge where H_2 molecules locate in the crystals. Further theoretical calculations that would explain both properties of the isolated molecules and the band structure of solids at the same time is necessary for understanding the structure of H_2 in the crystals.

VII. CONCLUSIONS

The Raman line shapes and frequencies of the lattice vibrations would change owing to the relaxation of the wave-vector selection rule for the optical phonons when introducing disorders in crystals. The degree of disorder in crystal is quantitatively evaluated in terms of the phonon correlation length L: a measure of size of the phonon confinement by the defects in crystals. L can be obtained by applying the SC model to the analysis of the Raman phonon line shape. In the SC model, spectral feature could shift or broaden, if L is finite, phonon dispersion curves vary significantly in the region near q = 0. Actually, the asymmetric line shapes in microcrystalline Si and other crystals with defects were well reproduced by this model. For crystalline semiconductors such as Si and GaAs, the asymmetric line shapes caused by ion implantation were also well reproduced in terms of the SC model. It is surprising that the SC model was applied successfully to Raman scattering in the alloys ($Ga_{1-x}Al_xAs/GaAs$ and $Ga_{0.47}In_{0.53}As/InP$), showing a relaxation of the wave-vector selection rule due to the alloying induced-potential fluctuations.

Disordered graphite is known to exhibit a sensitive DIRS peak, and the in-plane phonon correlation length L_a can be obtained from the relative intensity ratio R of the D-peak (1360 cm^{-1}) with respective to the G-peak. As *La* decreased in the microcrystalline graphite, the D-peak became strong in the intensity and all the lines broadened. A detailed Raman study of the ion-implanted graphite showed a dramatic change in line shape at the dose of 5×10^{15} ions/cm², indicating an abrupt transformation to an amorphous layer at a critical dose. The ion mass and energy dependence on Raman spectra were explained in terms of the ion range, the ion straggling, and the optical penetration depth. The disordered structures for the ion-irradiated graphite was clearly mapped with linewidth and the *R*. and each domain in the map corresponded to a characterized TEM picture. It was proven from SERS that the outmost surface is highly damaged by ion irradiation. For other DIRS peaks in graphite six bands of DOS were observed in a lower frequency range after the annealing of amorphous carbon films, suggesting the formation of

nanocrystallites of $L_a \approx 1.3$ nm. DIRS peaks were observed in other disordered materials such as TiCx or ion-implanted GaAs.

Combined with the removal techniques of surface layers, it is important to take Raman scattering depth profiles to know the structural depth profiles. It was evident that the profile of LO frequency shift followed well the nuclear energy loss curve in the 1 MeV Si+ implanted GaAs. The resonant Raman scattering or the Raman scattering of coupled LO phonon-plasma modes was suggested to be a new sensitive probe of defects in ion-implanted semiconductors.

Kinetic studies of lattice disordering of crystals became possible, using the real-time Raman measurements during ion irradiation in a scale of seconds. With the real-time technique, the disordering rates were experimentally determined, and the phonon confinement due to the local defects was observed in the kinetic manner. The measurements were first applied to graphite. The experiments were focused on the very initial stage of the disordering, where the basal plane structure of graphite maintained with only local defects. The square root dependence of the irradiation time to the reciprocal of the in-phonon correlation length ($1/La$) was well reproduced by the IDD model assuming $\ell_d = La$ in the graphite plane: a phonon confinement in a small area surrounded with defects. For GaAs the cubic root dependence of the irradiation time to the reciprocal of the phonon correlation length ($1/L$) was observed. The agreement in ion-dose dependence of ℓ_d and L_a implied that the IDD model is applicable to the three-dimensional crystals as well as two dimensional. To restate, the LO phonon becomes localized in a small volume surrounded with defects as the ion dose increases.

The real-time Raman measurements led us to the direct observation of the thermal relaxation processes of the disordered structures. The relaxation rates were determined

for graphite irradiated with low-energy ions. To date, three distinct stages of thermal relaxation process with different rates have been observed in the ion-irradiated graphite. The thermal relaxation kinetic study has been performed only for graphite. This real-time study should be extended to other crystals.

The increase in optical absorption coefficient in the near-surface damage region resulted in the Raman intensity decrease in the crystals irradiated with low-energy ions. This could provide another way for the disordering kinetic study of crystals.

Localized vibration modes provide detailed and more intuitive information about the identity and the lattice location of both isolated and complexed impurity atoms in crystals. In many of studies on the localized vibration modes, the Raman spectroscopy was complementary with the IR absorption. In this paper the localized modes of the hydrogen-related defects were discussed in detail. In the hydrogenated crystalline Si, the local vibrational bands of the Si–H bonds observed were strongly temperature dependent, and the one that is unstable above 250°C was suggested to relate to the platelet.

Very recently, hydrogen molecules in the hydrogenated crystalline Si and GaAs were detected using Raman scattering. The observed vibrational band of H_2 in the Si had a similar frequency to that of H_2 in gas, liquid, and solid phases, and much higher linewidth. On the other hand, the H_2-line in the GaAs was sharp and downshifted in frequency. A systematic Raman experiment for the hydrogenated Si showed that the H_2 does not exist in free spaces like voids or platelets. However, it is still controversial both experimentally and theoretically in which sites H_2 molecules are present.

To understand more about defects in crystals, it is of importance to relate localized vibrational modes to the phonon correlation length that could be obtained from

the optical phonon modes. Such studies have not been well performed, including H_2 in crystals.

Local strains or stresses induced by defects can be also evaluated from Raman spectra. Some examples for this matter were explained.

For future directions, coherent optical phonon oscillations[151,152] and excited phonon-population decay[153] were observed directly by the pump/probe techniques using ultrashort pulse lasers in the picosecond and femtosecond time regime. It is of importance and of interest to apply the techniques to the vibrational spectroscopic studies on defects in crystals.

ACKNOWLEDGMENT

REFERENCES

1. Cardona, M., *Light Scattering in Solids*, Cardona, M., Ed., Springer-Verlag, Berlin, 1975.

2. Nakashima, S., Ohta, H., and Hangyo, M., *Phil. Mag. B*, **70**, 971, 1994.

3. On the other hand, using inelastic neutron scattering or high-resolution electron energy loss (HREELS) spectroscopy, we can explore the entire Brillouin zone in the phonon dispersion relation.

4. London, R., *Adv. Phys.*, **16**, 345, 1978.

5. Mooradian, A., *Laser Handbook*, Arecchi, F. T. and Schulzdu Bois, E. O. Eds., North-Holland Publishing, Amsterdam, 1972, 2.

6. Katoda, T., *Evaluation of Semiconductors by Laser Raman Spectroscopy*, University of Tokyo Press, Tokyo, 1988.

7. Pollak, F., Characterization of semiconductors by Raman spectroscopy, Chap. 6 *Analytical Raman Spectroscopy*, Grasselli, J. G. and Bulkin, B. J., Eds., 1991.

8. Anderson, A., *The Raman Effect*, Marcel Dekker, New York, 1973.

9. Turrel, G., *Infrared and Raman Spectra of Crystals*, Academic Press, London, 1972.

10. Long, D. A., *Raman Spectroscopy*, McGraw-Hill, New York, 1977.

11. Hamaguchi, H. and Hirakawa, A., *Raman Spectroscopy*, Measurement Method Series 17, Gakkai Shuppan Center, Tokyou, 1988.

12. Richter, H., Wang, Z. P., and Ley, L., *Solid State Commun.*, **39**, 625, 1981.

13. Campbell, I. H. and Fauchet, P. M., *Solid State Commun.*, **58**, 739, 1986.

14. Huang, X., Ninio, F., Brown, J., and Prawer, S., *J. Appl. Phys.*, **77**, 5910, 1995

15. Tiong, K. K., Amirtharaj, P. M., Pollak, F. H., and Aspnes, D. E., *Appl. Phys. Lett.*, **44**, 122, 1984.

16. Braunstein, G., Tuschel, D., Chen, S., and Lee, S.-Tong., *J. Appl. Phys.*, **66**, 3515, 1989.

17. Iqbal, Z., Webb, A. P., and Veprek, S., *Appl. Phys. Lett.*, **36**, 136, 1980.

18. Fauchet, P. M. and Campbell, I. H., *Crit. Rev. Sol. Stat. Mater. Sci.*, **14**, S79, 1988.

19. Lespade, P., Al-Jishi, P., and Dresselhaus, M. S., *Carbon*, **20**, 427, 1982.

20. Maeda, M., Kuramoto, Y., and Horie, C., *J. Phys. Soc. Japan.*, **47**, 337, 1979.

21. Leung, S. Y., Dresselhaus, G., and Dresselhaus, M. S., *Phys. Rev. B*, **24**, 6083, 1981.

22. Dresselhaus, M. S. and Dresselhaus, G., *Light Scattering in Solids*, 3, Cardona, M., Eds., Springer-Verlag, New York, 1982.

23. Tuinstra, F. and Koenig, J. L., *J. Chem. Phys.*, **53**, 1126, 1970.

24. Knight, D. S. and White, W. B., *J. Mater. Res.*, **4**, 385, 1989.

25. Nakamura, K., Fujitsuka, M., and Kitajima, M., *Phys. Rev. B*, **41**, 12 260, 1990.

26. Nakamizo, M. and Tamai, K., *Carbon*, 22, 197, 1984.

27. Li, F. and Lannin, J. S., *Appl. Phys. Lett.*, 61, 2116, 1992.

28. Nemanich, R. J., Solin, S. A., and Martin, R. M., *Phys. Rev. B*, 23, 6348, 1981.

29. Nakamura, K. G., unpublished work.

30. Asari, E., Kamioka, I., Nakamura, K. G., Kawabe, T., Lewis, W. A., and Kitajima, M., *Phys. Rev. B*, 49, 1011, 1994.

31. Nakashima, S. and Tahara, K., *Phys. Rev. B*, 40, 6339, 1989.

32. Sasaki, Y., Nishina, Y., Sata, M., and Okamura, K., *Phys. Rev. B*, 40, 1762, 1989.

33. Betsch, R. J., Park, H. L., and White, W. B., *Mat. Res. Bull.*, 26, 613, 1991.

34. Parayanthal, P. and Pollak, F. H., *Phys. Rev. Lett.*, 52, 1822, 1984.

35. Shuker, R. and Gammon, R. W., *Phys. Rev. Lett.*, 25, 222, 1970.

36. Fauchet, P. M., *Light Scattering in Semiconductor Structures and Superlattices*, Lockwood, D. J. and Young, J. F., Eds., Plenum Press, New York, 1990.

37. Fuchs, H. D., Stutzmann, M., Brandt, M. S., Rosenbauer, M., Weber, J., Breitschwerdt, A., Deak, P., and Cardona, M., *Phys. Rev. B*, 48, 8172, 1993.

38. Nemanich, R. J. and Solin, S. A., *Phys. Rev. B*, 20, 392, 1979.

39. Nemanich, R. J. and Solin, S. A., *Solid State Commun.*, 23, 417, 1977.

40. Wada, N., *Phys. Rev. B*, 24, 1065, 1981.

41. Ishida, H., Fukuda, H., Katagiri, G., and Ishitani, A., *Appl. Spec.*, 40, 322, 1986.

42. Nakamura, K. and Kitajima, M., *Solid State Commun.*, 82, 475, 1992.

43. Dillon, R. O., Woollam, J. A., and Katkanant, V., *Phys. Rev. B*, 29, 3482, 1984.

44. Bowden, M., Gardiner, D. J., and Southall, J. M., *J. Appl. Phys.*, 71, 521, 1992.

45. Klein, M. V., Holy, J. A., and Williams, W. S., *Phys. Rev. B*, 17, 1546, 1978.

46. Mammone, J. F., Sharama, S. K., and Shimomura, O., *Solid State Commun.*, 34, 799, 1980.

47. Hirata, T., Kitajima, M., Nakamura, K. G., and Asari, E., *J. Phys. Chem. Solid.*, 55, 349, 1994.

48. Hirata, T., Ishioka, K., Kitajima, M., and Doi, H., *Phys. Rev. B*, 53, 8442, 1996.

49. Weber, W., *Phys. Rev. B*, 15, 4789, 1977.

50. Nakamura, K., Fujitsuka, M., and Kitajima, M., *Chem. Phys. Lett.*, 172, 205, 1990.

51. Wagner, J. and Hoffman, Ch., *Appl. Phys. Lett.*, 50, 682, 1987.

52. Holtz, M., Zallen, R., and Brafman, O., *Phys. Rev. B*, 37, 4609, 1988.

53. Holtz, M., Zallen, R., and Brafman, O., *Phys. Rev. B*, 38, 6097, 1988.

54. Nakamura, T. and Katoda, T., *J. Appl. Phys.*, 53, 5870, 1982.

55. Motooka, T. and Holland, O. W., *Appl. Phys. Lett.*, 58, 2360, 1991.

56. Zhang, P. X., Michell, I. V., Tong, B. Y., and Schultz, P. J., *Phys. Rev. B*, 50, 17080, 1994.

57. Waugh, J. T. and Dolling, G., *Phys. Rev.*, 132, 2410, 1963.

58. Biersack, J. P. and Haggmark, L. G., *Nucl. Instrum. Methods*, 174, 257, 1980.

59. Ishioka, K., Nakamura, K. G., and Kitajima, M., *Phys. Rev. B*, 52, 2539, 1995.

60. Erman, M., Theeten, J. B., Chambon, P., Kelso, S. M., and Aspnes, D. E., *J. Appl. Phys.*, 56, 2664, 1984.

61. Aspnes, D. E. and Studna, A. A., *Phys. Rev. B*, 27, 985, 1983.

62. Aspnes, D. E., Kelso, S. M., Olson, C. G., and Lynch, D. W., *Phys. Rev. Lett.*, 48, 1863, 1982.

63. Feng, G. F. and Zallen, R., *Phys. Rev. B*, 40, 1064, 1989.

64. Feng, G. F. and Zallen, R., *Phys. Rev. B*, 43, 9678, 1991.

65. Lindhard, J., Scharff, M., and Schiott, H. E., Kgl. Danske Vid. Selsk. Matt-Fys. Medd., 33, 14, 1963.

66. Sauncy, T., Holtz, M., and Zallen, R., *Phys. Rev. B*, 50, 10 702, 1994.

67. Wang, P. D., Foad, M. A., Sotomayor-Torres, C. M., Thoms, S., Watt, M., Cheung, R., Wilkinson, C. D. W., and Beaumont, S. P., *J. Appl. Phys.*, 71, 3754, 1992.

68. Smith, J. E., Brodsky, M. H., Crowder, B. L., and Nathan, M. I., *J. Non-Cryst. Solids*, 8, 179, 1972.

69. Elman, B. S., Shayegen, M., Dresselhaus, M. S., Mazurek, H., and Dresselhaus, G., *Phys. Rev. B*, 25, 4142, 1982.

70. Elman, B. S., Dresselhaus, M. S., Dresselhaus, G., Maby, E. W., and Mazurek, H., *Phys. Rev. B*, 24, 1027, 1981.

71. Kitajima, M., Aoki, K., and Okada, M., *J. Nucl. Mater.*, 149, 269, 1987.

72. Tanabe, T., Muto, S., Gotoh, Y., and Niwase, K., *J. Nucl. Mater.*, 175, 258, 1990.

73. Wright, R. B., Varma, R., and Gruen, D. M., *J. Nucl. Mater.*, 63, 415, 1976.

74. Niwase, K. and Tanabe, T., *Materials transactions, JIM.*, 34, 1111, 1993.

75. Niwase, K., *Phys. Rev. B*, 52, 15 785, 1995.

76. Maeta, H. and Sato, Y., *Solid State Commun.*, 23, 23, 1977.

77. Kitajima, M., Fujitsuka, M., Shinno, H., and Okamoto, S., *J. Mater. Sci. Lett.*, 9, 19, 1990.

78. Kitajima, M., Nakamura, K., Fujitsuka, M., Shinno, H., and Tanabe, T., *J. Nucl. Mater.*, 179, 180, 1991.

79. Nakamura, K. and Kitajima, M., *Appl. Phys. Lett.*, 59, 1550, 1991.

80. Kitajima, M. and Nakamura, K., *J. Nucl. Mater.*, 191, 356, 1992.

81. Nakamura, K. and Kitajima, M., *Phys. Rev. B*, 45, 78, 1992.

82. Kitajima, M., Asari, E., and Nakamura, K. G., *Tanso.*, 166, 47, 1995.

83. Nakamura, K. and Kitajima, M., *Phys. Rev. B*, 45, 5672, 1992.

84. Nakamura, K. G. and Kitajima, M., *Surface Science*, 283, 255, 1993.

85. Sigmund, P., *Sputtering by Particle Bombardment I*, Behrisch, R., Ed., Springer-Verlag, Berlin, 1981, 9.

86. Kinchin, G. H. and Pease, R. S., *Rep. Prog. Phys.*, 18, 1, 1955.

87. Nakamura, K. G., Asari, E., and Kitajima, M., *J. Nucl. Mater.*, 187, 294, 1992.

88. Asari, E., Kamioka, I., Lewis, W. A., Kawabe, T., Nakamura, K. G., and Kitajima, M., *NIM. B*, 91, 545, 1994.

89. Ishioka, K., Nakamura, K. G., and Kitajima, M., *Sur. Sci.*, 357, 495, 1996.

90. Kitajima, M., *Proc. Material Chemistry 96*, Kitajima, M., Haneda, H., Ishioka, K., and Hirata, T., Eds., 1996, 87.

91. Ishioka, K., Nakamura, K. G., and Kitajima, M., *J. Mater. Sci. Lett.*, 16, 281, 1997.

92. Aspnes. D. E., Studna, A. A., and Kinsbron, E., *Phys. Rev. B*, 29, 768, 1984.

93. Ishioka, K., Nakamura, K. G., and Kitajima, M., *Solid State Commun.*, 96, 387, 1995.

94. Niwase, K., Tanabe, T., and Tanaka, I., *J. Nucl. Mater.*, 191, 335, 1992.

95. Nakamura, K., G., Asari, E., and Kitajima, M., *Solid State Commun.*, 82, 569, 1992.

96. Asari, E., Kitajima, M., Kawabe, T., and Nakamura, K. G., *Phys. Rev. B*, 47, 11 143, 1993.

97. Kitajima, M., Asari, E., and Nakamura, K. G., *J. Nucl. Mater.*, 212, 139, 1994.

98. Asari, E., Kitajima, M., Nakamura, K. G., and Kawabe, T., *J. Sur. Sci. Jpn.*, 14, 301, 1993.

99. Asari, E., Kitajima, M., Nakamura, K., G., and Kawabe, T., *J. Sur. Sci. Jpn.*, 15, 31, 1994.

100. Asari, E., Kitajima, M., Nakamura, K. G., and Kawabe, T., *J. Nucl. Mater.*, 244, 173, 1997.

101. Asari, E., Thesis, March 1996, The University of Tsukuba.

102. Söder, B., Roth, J., and Möller, W., *Phys. Rev. B*, **37**, 815, 1988.

103. Thrower, P. A. and Mayer, R. M., *Phys. Status Solidi* (a), **47**, 11, 1978.

104. Iwata, T. and Nihira, T., *Jpn. J. Appl. Phys.*, **15**, 575, 1976.

105. Suezawa, M. and Katayama-Yoshida, H., *Materials Science Forum Vols. 196–201*, Trans Tech Publications, Switzerland, 1995.

106. Davies, G. and Nazare, M. H., *Program and Abstracts Book of Proc. 19th International Conference of Defects in Semiconductors*, Universidade de Aveiro, 1997.

107. Pankove, J. I. and Johnson, N. M., *Hydrogen in Semiconductors*, Academic Press, New York, 1991.

108. Pearton, S. J., Corbett, J. W., and Stavola, M., *Hydrogen in Crystalline Semiconductors*, Springer-Verlag, Berlin, 1991.

109. Stavola, M. and Pearton, S. J., *Hydrogen in Semiconductors.*, Pankove, J. I. and Johnson, N. M., Eds., Academic Press, New York, 1991, Chap. 8.

110. Stavola, M., Zheng, J.-F., Cheng, Y. M., Abernathy, C. R., and Pearton, S. J., *Mater. Sci. Forum.*, **196**, 809, 1995.

111. Markevich, V. P., Suezawa, M., and Sumino, K., *Mater. Sci. Forum.*, **196**, 915, 1995.

112. Hatakeyama, H., Suezawa, M., Markevich, V. P., and Sumino, K., *Mater. Sci. Forum.*, **196**, 939, 1995.

113. Pajot, B., Newman, R. C., Murray, R., Jalil, A., Chevallier, J., and Azoulay, R., *Phys. Rev. B*, **37**, 4188, 1988.

114. Pajot, B., *Shallow Impurities in Semiconductors 1988*, Monemar, B., Ed., IOP. Bristol, 1989, 473.

115. Clerjaud, B., Gendron, F., and Krause, M., *Phys. Rev. Lett.*, **65**, 1800, 1990.

116. Kozuch, D. M., Stavola, M., Pearton, S. J., Abernathy, C. R., and Lopata, J., *Appl. Phys. Lett.*, **57**, 2561, 1990.

117. Stutzmann, M., Beyer, W., Tapfer, L., and Herrero, C. P., *Physica B*, **170**, 240, 1991.

118. Stutzmann, M. and Herrero, C. P., *Appl. Phys. Lett.*, **51**, 1413, 1987.

119. Gruen, D. M., Varma, R., and Wright, R. B., *J. Chem. Phys.*, **64**, 5000, 1976.

120. Johnson, N. M., Ponce, F. A., Street, R. A., and Nemanich, R. J., *Phys. Rev. B*, **35**, 4166, 1987.

121. Johnson, N. M., *Hydrogen in Semiconductors*, Pankove, J. I., Ed., Academic Press, New York, 1991, Chap. 7.

122. Heyman, J. N., Ager, III, J. W., Haller, E. E., Johnson, N. M., Walker, J., and Doland, C. M., *Phys. Rev. B*, **45**, 13363, 1992.

123. Fukata, N., Sasaki, S., Murakami, K., Ishioka, K., Nakamura, K., G., Kitajima, M., Fujimura, S., Kikuchi, J., and Haneda, H., *Phys. Rev. B*, **56**, 1, 1997.

124. Deak, P., Ortiz, C. R., Snyder, L. C., and Corbett, J. W., *Physica. B*, **170**, 233, 1991.

125. Knights, J. C., Lucovsky, G., and Nemanich, R. J., *Philosophical Magazine B*, **37**, 467, 1978.

126. Nevin, W. A., Yamagishi, H., Asonka, K., Nishio, H., and Tawada, Y., *Appl. Phys. Lett.*, **59**, 3294, 1991.

127. Tsang, J. C., Oehrlein, G. S., Haller, I., and Custer, J. S., *Appl. Phys. Lett.*, **46**, 589, 1985.

128. Hines, M. A., Chabal, Y. J., Harris, T. D., and Harris, A. L., *J. Chem. Phys.*, **101**, 8055, 1994.

129. Chang, K., J. and Chadi, D. J., *Phys. Rev. Lett.*, **62**, 937, 1989; Chadi, D. J. and Park, C. H., *Phys. Rev. B*, **52**, 8877, 1995; Chang, K. J. and Chadi, D. J., *Phys. Rev. B*, **40**, 11644, 1989.

130. Holbech, J. D., Nielsen, B. B., Jones, R., Sitch, P., and Öberg, S., *Phys. Rev. Lett.*, **71**, 875, 1993.

131. Chabal, Y. J. and Patel, C. K. N., *Phys. Rev. Lett.*, **53**, 210, 1984.

132. Murakami, K., Fukata, N., Sasaki, S., Ishioka, K., Kitajima, M., Fujimura, S., Kikuchi, J., and Haneda, H., *Phys. Rev. Lett.*, **77**, 3161, 1996; Fukata, N., Sasaki, S., Murakami, K., Ishioka, K., Kitajima, M., Fujimura, S., and

Kikuchi, J., *Jpn. J. Appl. Phys.*, **35**, 1069, 1996.

133. Vetterhöffer, J., Wagner, J., and Weber, J., *Phys. Rev. Lett.*, **77**, 5409, 1996.

134. Newman, R. C., Grosche, E. G., Ashwin, M. J., Davidson, B. R., Robbie, D. A., Leigh, R. S., and Sangster, M. J. L., *Proc. Int. Conf. Defects. in Semiconductors 19*, Davis, G. and Nazare, M. H., Eds., Aveiro, 1997, in press.

135. Van de Walle, C. G., *Phys. Rev. B*, **49**, 4579, 1994.

136. Murakami, K., Fukata, N., Sasaki, S., Ishioka, K., Kitajima, M., Fujimura, S., Kikuchi, J., and Haneda, H., *Proc. Material Res. Soc.*, **442**, 269, 1997; Ishioka, K., Nakamura, K. G., Kitajima, M., Fukata, N., Sasaki, S., Murakami, K., Fujimura, S., Kikuchi, J., and Haneda, H., *Appl. Surface Sci.*, **117**, 37, 1997.

137. Kitajima, M., Ishioka, K., Nakamura, K. G., Fukata, N., Murakami, K., Kikuchi, J., and Fujimura, S., *Proc. Int. Conf. Defects. in Semiconductors 19*, Davis, G. and Nazare, M. H., Eds., Aveiro, 1997, in press.

138. Leitch, A. W. R., Alex, V., and Weber, J., *Proc. Int. Conf. Defects in Semiconductors 19*, Davies, G. and Nazare, M. H., Eds., Aveiro, 1997, in press.

139. May, A. D., Degen, V., Stryland, J. C., and Welsh, H. L., *Can. J. Phys.*, **39**, 1769, 1961.

140. Hartwig, C. M. and Vitko, J., *Phys. Rev. B*, **18**, 3006, 1978.

141. Van de Walle, C. G., Denteneer, P. J. H., Bar-Yam, Y., and Pantelides, S. T., *Phys. Rev. B*, **39**, 10791, 1989.

142. Fukata, N., Murakami, K., Ishioka, K., Nakamura, K. G., Kitajima, M., Fujimura, S., Kikuchi, J., and Haneda, H., *Proc. Int. Conf. Defects. in Semiconductors 19*, Davies, G. and Nazare, M. H., Eds., Aveiro, 1997, in press.

143. Ishioka, K., Nakamura, K. G., Kitajima, M., Fukata, N., Murakami, K., Fujimura, S.,

144. Pritchard, R. E., Ashwin, M. J., Newman, R. C., Tucker, J. H., Lightowlers, E. C., Binns, M. J., Falster, R., and McQuaid, S. A., *Proc. Int. Conf. Defects. in Semiconductors, 19*, Davies, G. and Nazare, M. H., Eds., Aveiro, 1997, in press; Pritchard, R. E., Ashwin, M. J., Newman, R. C., Tucker, J. H., Lightowlers, E. C., Binns, M. J., Falster, R., and McQuaid, S. A., *Phys. Rev. B*, in press.

145. Nakamura, K. G., Ishioka, K., Kitajima, M., and K., Murakami, *Solid State Commun.*, **101**, 735, 1997; Nakamura, and Kitajima, M., *Jpn. J. Appl. Phys.*, **36**, 2004, 1997.

146. Nakamura, K. G., Ishioka, K., Kitajima, M., Endou, A., Miyamoto, A., *J. Chem. Phys.*, in press.

147. Van de Walle, submitted to *Phys. Rev. Lett.*

148. Okamoto, Y., Saito, M., and Oshiyama, A., *Phys. Rev. B*, B56, 10016, 1997.

149. Shen, H. and Pollak, F. H., *Appl. Phys. Lett.*, **45**, 692, 1984.

150. Kitajima, M. and Nakamura, K. G., *J. Nucl. Mater.*, **175**, 251, 1990.

151. Cho, G. C., Kuett, W., and Kurz, H., *Phys. Rev. Lett.*, **65**, 764, 1990; Dekorsky, T., Auer, H., Waschke, C., Bakker, H. J., Roskos, H. G., and Kurz, H., *Phys. Rev. Lett.*, **74**, 738, 1995.

152. Hase, M., Mizoguchi, K., Harima, H., Nakashima, S., Tani, M., Sakai, K., and Hangyo, M., *Appl. Phys. Lett.*, **69**, 2474, 1996.

153. Fuchs, H. D., Grein, C. H., Devlin, R. I., Kuhl, J., and Cardona, M., *Phys. Rev. B*, **44**, 8633, 1991.

154. Ogura, A., Honea, E. C., Murray, C. A., Raghavachari, K., Sprenger, W. O., Jarrold, M. F., and Brown, W. L., *Mater. Res. Soc. Symp. Proc.*, Vol. 332, Material Research Society, 1994, p. 333.